

Experimental investigation of the velocity and temperature fields near the walls in turbulent Rayleigh-Bénard convection

DISSERTATION

zur Erlangung des akademischen Grades

DOKTORINGENIEUR

(Dr.-Ing.)

vorgelegt der

Fakultät für Maschinenbau der

Technischen Universität Ilmenau

von Frau

Master Ling Li

geboren am 05.11.1983

in Shenyang, China

Acknowledgments

This work has been carried out at the Institute of Thermodynamics and Fluid Mechanics, in the Department of Mechanical Engineering, Ilmenau University of Technology under the supervision of Dr. Ronald du Puits, the group leader of the Barrel of Ilmenau.

First of all, I would like to thank my family and all my friends. Without their support and encouragement, this work would not have been successful.

I would like to give special thanks to Dr. Ronald du Puits for his generous support and guidance.

For working closely together, for the nice numerical simulation results I thank Nan Shi.

For many fruitful discussions with Prof. André Thess, Prof. Jörg Schumacher and Dr. Christian Resagk, I also extend my deep gratitude.

For their technical assistance, my thanks go to Vigimantas Mitschunas, Klaus-Dieter Henschel and Helmut Hoppe.

I would also like to offer my gratitude to Robert Kaiser, Max Körner, Dr. Elka Lobutova, Hauke Hirsch, Yogesch Kumar Agrawal and the other members of our institute, with whom I have enjoyed a friendly and efficient working atmosphere.

Finally, I wish to acknowledge the financial support for this PhD work from the China Scholarship Council (Grant No. 2009608062) as well as the Deutsche Forschungsgemeinschaft within the Research Unit FOR 1182 and the Thüringer Ministerium für Bildung, Wissenschaft und Kultur.

Kurzfassung

Experimentelle Untersuchung von wandnahen Geschwindigkeits- und Temperaturfeldern in turbulenter Rayleigh-Bénard-Konvektion

Für den Wärmetransport in turbulenter Rayleigh-Bénard-Konvektion sind die beiden Grenzschichten an Heiz- und Kühlplatte von besonderer Bedeutung. In der vorliegenden Arbeit wird über die Messung von dreidimensionalen Geschwindigkeits- und Temperaturfeldern in turbulenter Rayleigh-Bénard-Konvektion mittels Laser-Doppler-Anemometrie und Mikro-Thermistor berichtet. Es wurden hochaufgelöste Geschwindigkeits- und Temperaturmessungen innerhalb und außerhalb der Grenzschichten bei verschiedenen Rayleigh-Zahlen, Aspektverhältnissen und Messpositionen durchgeführt. Ein Teil der Daten wurde mit äquivalenten Ergebnissen aus direkten numerischen Simulationen (DNS) verglichen. Für die physikalische Beschreibung der Grenzschicht und für die Überprüfung von verschiedenen Grenzschichtmodellen, wie zum Beispiel die Prandtl-Blasius-Lösung, werden zeitgemittelte Geschwindigkeits- und Temperaturprofile, die Profile von deren Fluktuationen, die Skalierungsgrößen der Grenzschicht, die Scher-Reynolds-Zahl und die Invarianten des Reynoldsschen Spannungstensors bei Rayleigh-Zahlen im Bereich zwischen $Ra = 3,44 \times 10^9$ und $Ra = 9,78 \times 10^{11}$ und für Aspektverhältnisse im Bereich zwischen $\Gamma = 1,0$ und $\Gamma = 3,0$ analysiert. Die dreidimensionalen Geschwindigkeitsmessungen haben gezeigt, dass in der Nähe der Kühlplatte bei $Ra = 3,44 \times 10^9$ und $Ra = 2,88 \times 10^{10}$ keine wand-normale Geschwindigkeitskomponente existiert. Sowohl die viskose als auch die thermische Grenzschichtdicke skalieren mit der Rayleigh-Zahl wie $\delta_v \sim Ra^{-0,24}$ und $\delta_\theta \sim Ra^{-0,24}$. Der Vergleich der experimentell gewonnenen Daten mit denen aus der DNS basiert auf Ergebnissen bei Rayleigh-Zahlen $Ra = 3 \times 10^9$ und $Ra = 3 \times 10^{10}$, sowie einem festen Aspektverhältnis von $\Gamma = 1$. Es zeigte sich, dass die gemessenen Geschwindigkeitsdaten sehr gut mit den DNS-Daten übereinstimmen [1], die Temperaturdaten jedoch leicht differieren. Speziell die gemessenen Temperaturprofile zeigen nicht den linearen Verlauf der DNS-Daten und die gemessenen Temperaturgradienten an der Wand sind signifikant größer als die DNS-Werte. Weiterhin wird in der Arbeit über simultane Geschwindigkeits- und Temperaturmessungen in der großen Konvektionszelle bei $Ra = 8,96 \times 10^{11}$, $\Gamma = 1,13$ an drei verschiedenen Messpositionen berichtet. Es wurden die Profile der wand-normalen Geschwindigkeit und der Temperatur untersucht sowie diffusiver und konvektiver Wärmetransport aus den gemessenen Geschwindigkeits- und Temperaturfluktuationen berechnet. Dabei zeigte es sich, dass bei der Wärmeübertragung innerhalb der Grenzschicht der diffusive und außerhalb der Grenzschicht der konvektive Transport dominiert.

Abstract

Experimental investigation of the velocity and temperature fields near the walls in turbulent Rayleigh-Bénard convection

The boundary layers at the heating and the cooling plates are of particular importance for the heat transport in turbulent Rayleigh-Bénard convection. This work reports measurements of the three-dimensional velocity and temperature fields in turbulent Rayleigh-Bénard convection in air using laser Doppler anemometry and micro thermistor. Highly resolved velocity and temperature measurements inside and outside the boundary layers at different Rayleigh numbers, aspect ratios and locations were carried out. Parts of the data have been directly compared with equivalent data obtained in Direct Numerical Simulations (DNS). In order to describe the boundary layer or to verify various predictions of boundary layer solution, such as the Prandtl-Blasius solution, we have analyzed the mean velocity and temperature profiles and their fluctuations, the boundary layer scalings, the shear Reynolds numbers, the invariants of the Reynolds stress tensor at Rayleigh numbers in the range between $Ra = 3.44 \times 10^9$ and $Ra = 9.78 \times 10^{11}$ and aspect ratios in the range between $\Gamma = 1.0$ and $\Gamma = 3.0$. From the 3D velocity measurements at $Ra = 3.44 \times 10^9$ and $Ra = 2.88 \times 10^{10}$, we found that there is no mean wall-normal velocity. Both viscous and thermal boundary layer thickness scale with respect to the Rayleigh number as $\delta_v \sim Ra^{-0.24}$ and $\delta_\theta \sim Ra^{-0.24}$, respectively. The comparison between the experimental data and that data obtained from DNS is based on a set of two Rayleigh numbers at $Ra = 3 \times 10^9$ and $Ra = 3 \times 10^{10}$ and a fixed aspect ratio of $\Gamma = 1$. We found that the measured velocity data is in good agreement with the DNS results [1] while the temperature data slightly differs. In particular, the measured mean temperature profile does not show the linear trend as seen in the DNS data and the measured gradients at the wall are significantly higher than those obtained from the DNS. Additionally, we report simultaneous velocity and temperature measurement results obtained in the large convection cell at $Ra = 8.96 \times 10^{11}$, $\Gamma = 1.13$ at three different locations. The mean wall-normal velocity and temperature profiles, diffusive and convective heat fluxes calculated from the directly measured velocity and temperature fluctuations are studied in this work. We found that the heat transport inside the boundary layer is dominated by diffusion while outside the boundary layer it is dominated by convection.

| | | |
|----------|---|-----------|
| 1 | Introduction | 1 |
| 1.1 | Motivation of the thesis | 1 |
| 1.2 | Overview of experimental facilities | 3 |
| 1.3 | Overview of theoretical and experimental boundary layer analysis | 4 |
| 1.4 | Outline of the thesis | 9 |
| 2 | Basics of the Rayleigh-Bénard Convection | 11 |
| 2.1 | Basic equations and parameters | 11 |
| 2.2 | Large-scale circulation (LSC) and formation of boundary layers | 13 |
| 2.3 | Blasius and Pohlhausen solutions of the boundary layer equations | 14 |
| 3 | Experimental apparatus | 17 |
| 3.1 | RB convection facility “Barrel of Ilmenau” (BOI) | 17 |
| 3.2 | Small convection cell for 3D velocity and temperature measurements built in the large convection cell | 21 |
| 4 | Measurement technique and calibration | 23 |
| 4.1 | Velocity field measurements using laser Doppler anemometry (LDA) | 23 |
| 4.1.1 | LDA introduction and measurement principles | 23 |
| 4.1.2 | LDA seeding particles | 26 |
| 4.2 | Velocity measurement set-up in the BOI | 28 |
| 4.2.1 | 3D set-up with two LDA probes | 28 |
| 4.2.2 | Alignment and size of measurement volume | 31 |
| 4.3 | Temperature measurement | 32 |

| | | |
|----------|--|------------|
| 4.3.1 | Set-up and calibration of the micro-thermistor | 33 |
| 4.4 | Simultaneous velocity and temperature measurement set-up | 34 |
| 4.5 | Data post-processing | 38 |
| 5 | Results: velocity and temperature profiles from the small convection cell | 43 |
| 5.1 | Velocity and temperature profiles at aspect ratio $\Gamma = 1$ | 43 |
| 5.1.1 | Velocity profiles at the center line | 43 |
| 5.1.2 | Temperature profiles at the center line | 47 |
| 5.1.3 | Boundary layer scaling | 49 |
| 5.1.4 | Velocity profiles out of the center line | 55 |
| 5.1.5 | Turbulent stress invariant analysis | 57 |
| 5.2 | Velocity and temperature profiles at aspect ratio $\Gamma = 2.76$ | 58 |
| 5.2.1 | Velocity and temperature profiles at the center line | 59 |
| 5.2.2 | Velocity and temperature profiles out of the center line | 61 |
| 6 | Results: simultaneous velocity and temperature profiles from the large convection cell | 65 |
| 6.1 | Simultaneous velocity and temperature profiles and their fluctuations at the center line | 65 |
| 6.2 | Simultaneous velocity and temperature profiles and their fluctuations out of the center line | 73 |
| 7 | Discussion of measurement errors | 81 |
| 7.1 | Uncertainty analysis for the velocity data | 81 |
| 7.2 | Accuracy of the temperature data | 84 |
| 8 | Conclusion | 85 |
| 8.1 | Conclusion | 85 |
| 8.2 | Outlook | 87 |
| | Bibliography | 89 |
| | List of figures | 97 |
| | List of tables | 105 |

List of symbols

| Symbol | Unit | Explanation |
|----------------------|-----------------|--|
| Latin letters | | |
| a_{ij} | - | Reynolds stress anisotropy tensor. i, j are tensor indices |
| c_p | $kJ/kg \cdot K$ | heat capacity |
| D | m | diameter of heating or cooling plate |
| D_L | μm | beam waist at $1/e^2$ intensity drop |
| d_f | nm | fringe separation |
| d_{mv_x} | μm | height of the measurement volume |
| d_{mv_y} | μm | width of the measurement volume |
| E | - | beam expander ratio |
| f | mm | focal length of the front lens |
| g | m/s^2 | gravity acceleration |
| H | m | distance between the heating and cooling plate |
| I | A | electric current |
| l_{mv_z} | μm | length of the measurement volume |
| N_f | - | number of fringes |
| P | Pa | pressure |
| \dot{q} | W/m^2 | total heat flux |
| \dot{q}_d | W/m^2 | diffusive heat flux |
| \dot{q}_c | W/m^2 | convective heat flux |
| Ra | - | Rayleigh number |
| Re_s | - | shear Reynolds number |
| R_{th} | K/W | heat resistance |
| Pr | - | Prandtl number |
| Nu | - | Nusselt number |
| St | - | Stokes number |
| T | $^{\circ}C$ | temperature |
| T' | $^{\circ}C$ | temperature fluctuation |
| \bar{T} | $^{\circ}C$ | mean temperature |
| ΔT | $^{\circ}C$ | temperature difference between heating and cooling plate |
| t_r | s | particle relaxation time |

| Symbol | Unit | Explanation |
|--------------------------------------|------------------|---|
| t_c | s | characteristic time scale of flow |
| U | m/s | magnitude of the horizontal velocities |
| u_1, u_2 and u_3 | m/s | LDA measured three random velocity components |
| u, v and w | m/s | desired velocity components in Cartesian coordination system |
| \bar{v} | m/s | mean velocity |
| w' | m/s | wall-normal velocity fluctuation |
| Greek letters | | |
| α | $^{\circ}C^{-1}$ | thermal expansion coefficient |
| β, γ, ϵ and η | - | boundary layer scaling law exponents |
| δ | mm | boundary layer thickness |
| δ_v | mm | viscous boundary layer thickness |
| δ_{θ} | mm | thermal boundary layer thickness |
| ε_D | mW/K | thermal dissipation rate of the thermistor in air |
| η_{PB} | - | Prandtl-Blasius solution self-similar variable |
| θ | $deg (^{\circ})$ | beam intersection angle |
| ϑ_b | $^{\circ}C$ | mean bulk temperature |
| ϑ_{cp} | $^{\circ}C$ | mean surface temperature of the cooling plate |
| κ | m^2/s | thermal diffusivity |
| λ | nm | laser wavelength |
| λ_{th} | $W/m \cdot K$ | thermal conductivity |
| μ | $Pa \cdot s$ | dynamic viscosity |
| ν | m^2/s | kinematic viscosity |
| ρ | kg/m^3 | fluid density |
| σ | m/s | standard deviation |
| τ | - | delay time of the simultaneous velocity and temperature measurement |
| ϕ | $deg (^{\circ})$ | angle of the wind orientation |
| $\varphi_{1D,2D}$ | $deg (^{\circ})$ | alignment angle of the 1D and 2D LDA probes |
| Γ | - | aspect ratio D/H |

1.1 Motivation of the thesis

Thermal convection, without overstatement, is one of the most widespread kinds of flow phenomena in nature and technology. It is responsible for both the movement of air in the atmosphere and for the oceanic currents and also plays an important role in various technological applications. In the Earth's core the flow of molten iron ensures the formation and maintenance of the geomagnetic field. Furthermore, thermal convection plays a central role in many industrial processes such as in the generation of electricity, the air conditioning of buildings or the cooling of electronical equipment. The flows mentioned above have in common a high spatial and temporal complexity. It is rather difficult or even impossible to make exact mathematical descriptions for the fluid dynamic problems or to quantify them in many cases. Even now, with the use of massively parallel computers, it remains imperative to have an experimental facility, such as our large-scale convection facility, "Barrel of Ilmenau" (BOI), in order to study the turbulent temperature and velocity fields in large-scale convection in detail. Experimental data obtained from BOI can be with much higher spatial and temporal resolution and it is usually affected by less statistical uncertainty due to longer measurement times. So far, these sets of data are well-suited to prove earlier predicted theoretical models and state-of-the-art numerical simulations.

As elaborated, a great variety of natural and technical turbulent flows are driven by temperature differences. Rayleigh-Bénard (RB) convection is one of the paradigmatic models used to study the details of this kind of turbulence. In its simplest setting an infinitely extended horizontal fluid layer is enclosed by two isothermal plates, with a hot plate at the bottom and a cold plate at the top. In experiments, the finite flow volume is established by additional thermally-insulated side walls which can form a closed cylin-

1 Introduction

drical or rectangular cell. The focus of most experimental and numerical studies in this configuration is for a better understanding of the mechanisms of turbulent heat transport [2, 3], which is quantified by the dimensionless Nusselt number (Nu) as function of the input parameters, the Rayleigh number (Ra), the Prandtl number (Pr) and the aspect ratio Γ (defined in chapter 2). Since non-permeable walls enclose the moving fluid, boundary layers (BL) form at the horizontal as well as at the vertical walls. Although these BL become ever thinner when the velocity of the turbulent convective flow is increased, they cannot be neglected. The reason being that all the upward directed heat flux which is provided from the isothermally-heated bottom plate has to pass through these tiny layers at the bottom and top. Furthermore, it is well known that a large-scale circulation (LSC) builds up in closed cells which also interacts with the BLs. Moreover, except for these widely recognized thermal and viscous BLs near the horizontal upper and lower surfaces of the cell, there are further BLs created by this LSC close to the side-walls. Inside the horizontal BLs, related large temperature gradients exist, which are absent at the side-walls; therefore the horizontal BLs are with heat transport and the side-wall BLs are without heat transport. A better understanding of the mechanisms of global heat transport at large Rayleigh numbers remains thus intimately connected with a better understanding of the physics inside the BLs.

The point just mentioned above is exactly the main motivation for the present work – a detailed experimental analysis and comparison of the velocity and temperature fields inside the BL with phenomenological theories and direct numerical simulations (DNS). In this work, we take a first step in this direction and compare the statistics of time series from the turbulent flow field and temperature field data taken at points inside and outside the BLs allowing us to compose wall-normal profiles of the three velocity components and temperature at a few different locations close to the cooling plate of the cell. Experimentally, it requires a convection cell which is several meters high in order to take mean profiles in a less-than-a-centimeter thick BL, such as in BOI [4].

The two main objectives of the thesis constitute a characterization of the statistical properties of the velocity and temperature field in the close proximity of the horizontal plates. They contain:

1. Collection of highly-resolved velocity and temperature field data and comparison with direct numerical simulation results.
2. Analysis of the local heat transport through the BL by simultaneous measurement of wall-normal component velocity and temperature fluctuations at single points.

1.2 Overview of experimental facilities

In this chapter, we introduce several RB convection facilities. In order to quantitatively study the fundamental aspects of the complex RB convection flow, the experimentalists have to take several steps to make the study feasible, while not losing any of the main physical aspects. For modeling the natural convection at high Rayleigh numbers, there are two ways: first, using low viscosity fluids; second, working with large-scale experiments. In the recent years, the Hong Kong groups, Xia and Tong, conducted experiments in cells filled with water, $Pr = 5.4$. One of their present experimental set-ups is a vertical cylindrical cell with diameter, $D = 19.0$ cm and height, $H = 19.3$ cm. The side-wall is made of Plexiglass with a thickness of 5 mm. The corresponding aspect ratio is equal to $\Gamma = 0.98$. The upper stainless cooling plate is driven by a water circulation system. The temperature stability of the refrigerated circulator is 0.01°C . Two silicon rubber film heaters connected in a series are sandwiched to the back of the bottom plate to provide constant and uniform heating [5]. This is one of the typical RB experiments in water, which contributed some important results such as structures of vicious and thermal BLs, velocity and temperature profiles and their fluctuations [6, 7, 8, 9], however the limitation of water experiments is the relatively thin BL thickness (maximum up to ≈ 1 mm) and low Rayleigh numbers (up to $Ra = 10^{10}$).

In order to achieve even higher Rayleigh numbers, the former choice using fluid Helium at about 5 K near its critical point, was pursued by Castaing and co-workers in Chicago, USA [10], followed by Chavanne *et al.* in Grenoble, France [11]. They reached Rayleigh numbers up to $Ra \approx 10^{15}$. Another group, Niemela *et al.* in Oregon, USA [12], went further by also using low-temperature Helium in a larger cell, covering more than eleven orders of magnitude of Ra up to $Ra \approx 10^{17}$. They constructed a larger apparatus with $D \approx 0.5$ m and $L \approx 1$ m with at fixed $\Gamma = 0.5$. More recently, Ahlers, Funfschilling and Bodenschatz used a very large pressure vessel for RB experiments in Göttingen, Germany. This is a cylinder with a diameter of 2.5 m and length of 5.5 m in horizontal position, and with a turret above it that extends the height to 4 m over a diameter of 1.5 m. Because of its shape, this vessel has become known as the “U-Boot of Göttingen”. It can be filled with various gases at pressures up to 19 bars. A Rayleigh-Bénard sample cell with $L = 2.24$ m and $D = 1.12$ m (the “High Pressure Convection Facility” or HPCF) was placed in the section containing the turret, yielding $\Gamma = 0.5$ and $\Gamma = 1$. Using Sulfur Hexafluoride at 19 bars, they reached a Ra of $Ra \approx 2 \times 10^{15}$ [13]. The Helium or the high pressure experiments gave us the possibility to study global quantities, like heat transport, the large-scale circulation or the typical mean velocity (wind), but it is almost impossible to conduct

1 Introduction

detailed measurements in the BLs with high temporal and spatial resolution, because the BLs are of the order of less than 0.1 mm.

With the currently largest RB convection cell, Barrel of Ilmenau (BOI), 6.30 m in height, 7.15 m in diameter, it is possible to make much higher spatially and temporally resolved measurements than ever at Ra up to $Ra = 10^{12}$. The barrel is a closed cylindrical cell filled with air ($Pr = 0.7$), in which the BL thickness is of the order of 10 mm, ten times larger than in any other experiments with the same Ra . The variable plate distance allows us to investigate how the aspect ratio Γ effects the heat transport [14]. It also allows the study of different LSC structures (single roll, two co-existing rolls or more complicated three-dimensional structures) at various ratios reaching from 1 (using small inserted cells) to 143. At aspect ratio $\Gamma = 1$, we observed a single LSC roll, the so called “wind” and studied its oscillation of rotation axis and wind velocity and furthermore cessation [15]. The visualization results give us a clear up-welling and down-welling circulation by the “plumes” detaching from the heating and cooling plate [16]. The flow visualization was conducted in the BL of the heating plate along the path of the convective circulation in the BOI using laser light sheet and high-definition video camera (1920×1080 pixels, 30 frames per second). Overall, the BOI has the advantages of being fully accessible for all measurement techniques to study the highly complex, three-dimensional and extremely unstable flow conditions in detail [17, 18, 19, 20].

To summarize, experiments in water give us some information about the local flow field close to the horizontal plates, but the resolution is poor at $Ra > 10^{10}$. On one hand, BOI is the only facility in which the velocity and the temperature fields in the proximity of the plates can be studied in detail at $Pr = 0.7$. On the other hand, the low viscosity gas experiments provided good information of global quantities. One can also state that the knowledge of the local field variables, in particular within the BLs is still very poor. The local velocity and temperature measurements in highly turbulent RB convection would definitely help to improve our knowledge on the BL dynamics.

1.3 Overview of theoretical and experimental boundary layer analysis

Scaling theories of thermal convection aim at predicting transport laws for heat and momentum. Nu , the representing dimensionless parameter of heat transfer, is the ratio of convective to conductive heat transfer across the convection cell, in particular across the thermal BL. In thermal convection, the Nu is a function of Ra and Pr : $Nu(Ra, Pr)$. Furthermore, the Reynolds number Re , the representing dimen-

sionless parameter of momentum transfer, can be described by Ra and Pr: $Re(Ra, Pr)$. Both relations require a physical model for the BLs as an input. Though many efforts have been made by the pioneers on experimental and numerical studies of this relationship, the limited research conditions caused the limited statistic range of Ra, Pr and Γ .

There were people working on concepts of heat transfer as early as in 1922 [21], such as Davis. The first combined experimental and theoretical attempt is Malkus' marginal-stability theory in 1954 [22]. He used a water mixed with acetone, a water and an air filled cell with a maximum plate distance of 20 cm to measure the heat transport and the mean velocity, up to $Ra = 10^{10}$. The heat transport as power law had been calculated by the apparent linear part of the temperature curves, scaling in $Nu \sim Ra^{1/3}$. His theory was later experimentally studied by Deardorff and Willis (1967) [23], Krishnamurti (1970) [24] and Brown (1973) [25] and in 1967 it was theoretically confirmed by the work of Busse [26]. 20 years after Malkus' first power law valuation, the experiments by Fitzjarrald (1976) [27] applied a movable hot-wire anemometer in a $3.5 \text{ m} \times 3.5 \text{ m} \times 1.8 \text{ m}$ variable-height, closed convection box, using air as the working fluid. He measured the heat flux at Rayleigh numbers up to $Ra = 7 \times 10^9$ and velocities and temperatures up to $Ra = 1.7 \times 10^7$. Unlike Malkus, he found a universal scaling relation $Nu = 0.13 Ra^{0.30}$. However, the accuracy of the measurements was effected by strong temperature fluctuations and Ra was limited to $Ra = 10^9$. Since there is a necessity to investigate these relationships for higher Rayleigh numbers, experimentalists started using new working fluids, such as gaseous Helium or compressed Sulfur Hexafluoride SF_6 instead of the traditional working fluids, water and air. With these alternative fluids current Rayleigh numbers up to $Ra = 10^{17}$ are possible, since by small pressure and temperature changes, the kinematic viscosity and the thermal diffusivity of the fluids can be varied considerably. Furthermore, a wide range of variation of the experimental parameters, Ra and Pr, can be attained. The pioneering experiment was done with frozen Helium by Castaing *et al.* in 1989 [10]. This study of RB convection at roughly 5 K is performed in a cell with an aspect ratio of one. The Rayleigh numbers were in a range of $4 \times 10^7 < Ra < 6 \times 10^{12}$, in which the Pr remains between 0.65 and 1.5. The main observation of his work is the scaling behavior $Nu \sim Ra^{2/7}$. Further low-temperature Helium gas experimental studies on the Ra- and Pr-dependence of Nu and Re as well as their discrete transitions were made by M. Sano *et al.* (1989) [28], X. Chavanne *et al.* (1997) [11], J.J. Niemela *et al.* (2000) [12], X. Chavanne *et al.* (2001) [29], J.J. Niemela *et al.* (2003) [30]. The coupling of side-wall effects are actually in every laboratory inevitable, thus Sun *et al.* in 2005 included Γ in their study. These experiments were performed in a water-filled 1 m diameter cylindrical cell of aspect ratio $\Gamma = 0.67, 1, 2, 5, 10$ and 20. The measurements were conducted at the Prandtl number $Pr \approx 4$ with Ra

1 Introduction

varying from 1×10^7 to 5×10^{12} . He found that the Nu can be described by a combination of power laws of $\text{Nu} = C_1(\Gamma) \times \text{Ra}^{0.211} + C_2(\Gamma) \times \text{Ra}^{0.332}$, however, he also found that the Γ dependency on $\text{Nu}(\text{Ra}, \text{Pr})$ is very weak.

For a considerable number of experimental results, Grossmann and Lohse (GL) in 2000 [31] for the first time summarized a scaling theory over a wide range of parameters. The essential contribution of the GL theory is to separate the flow into a turbulent mixing zone and the BLs. In other words, it is supposed to separate the volume averages of both the kinetic and the thermal dissipation rate into respective bulk and BL contributions. The theory with regard to the dependence of the material properties Pr and the geometry Γ was presented in their papers of 2002 [32] and 2003 [33]. In this theory, another particularly interesting topic of turbulent RB convection, the transition to the “ultimate” regime, was discussed. In 1962, Kraichnan first raised the “ultimate” Ra regime theory [34], in which the flow inside the BL and the heat transfer are independent on the material properties of the fluid. Kraichnan estimated the Ra of the transition to the ultimate regime as high as $\text{Ra} = 10^{18}$. The estimation of GL theory leads to $\text{Ra} = 10^{14}$ and another representative experimental study showed a transition in Helium to be at $\text{Ra} = 10^{11}$ [11, 35].

A closer look at the heat transfer studies suggest that BLs play a crucial role in all convection flows. As the heat transport is dominated by viscous and thermal BLs, the direct characterization of the BL properties is essential for unravelling discrepancies between existing theoretical models and their verification and will also provide an insight into the physical nature of turbulent heat transfer in the RB system. After all of the above, the first basic study on velocity and temperature fields in an enclosed volume of air, which is heated from below and cooled from above was made by Deardorff and Willis in 1967 [23]. He measured horizontal and vertical velocities, temperature fluctuations and total heat flux, but given the small size of the experimental system, the Rayleigh numbers were limited at $\text{Ra} = 6.3 \times 10^5$, 2.5×10^6 and 1.0×10^7 . To achieve higher Ra, an experiment by Garon and Goldstein in 1973 [36] was performed in a cylindrically-shaped tube filled with water, 45 cm in diameter and $\Gamma = 0.5$. In their experiment, they applied laser Doppler anemometry (LDA) techniques to determine the rms velocity profiles for Rayleigh numbers up to $\text{Ra} = 2.5 \times 10^9$. However the small mean velocity required long-time velocity measurements in order to obtain sufficient data statistics. Tanaka and Miyata (1980) [37] used a photographic technique to measure the velocity fluctuations in water at varying Rayleigh numbers up to $\text{Ra} = 10^9$. However the accuracy of this velocity measurement was affected by taking the bubbles’ own buoyancy into account and there was no long-time average performed in the measurements. Velocity and

temperature measurements in turbulent RB convection at higher Rayleigh numbers were later carried out by Tilgner, Belmonte and Libchaber in 1993 [38] and 1994 [39]. The mean horizontal velocity, the mean temperature and their fluctuations were measured in a cubic cell ($\Gamma = 1$) filled with either water ($\text{Pr} = 6.6$) or with compressed SF_6 ($\text{Pr} = 0.7$), leading to Rayleigh numbers up to $\text{Ra} = 1.1 \times 10^9$. Due to the fact that the BL thickness was decreasing with increasing Ra , with the relatively large size of the thermistor ($500 \mu\text{m}$), it was difficult to generate high spatial resolution data. Thus their measurements led to an inaccurate assumption of the linear temperature profile. In 1993 Chillá *et al.* [40] designed a cell filled with water, with a horizontal size of $40 \times 10 \text{ cm}^2$, two possible aspect ratios $\Gamma = 1$ and 4, in order to measure both temporal fluctuations and spatial temperature profiles of turbulent thermal convection. Due to the small size of the cell, the measurement was limited at $\text{Ra} = 4 \times 10^8$. For a better understanding of BLs, Xia and Tong [7, 8, 41] used LDA to measure the mean horizontal velocity and their fluctuations inside the BL of the hot plate and the side-wall. The measurement was performed in a transparent cylindrical RB cell filled with water at a range of Rayleigh numbers of $\text{Ra} \leq 1.1 \times 10^{11}$. One of the conclusions was that with respect to the distance z from the lower surface of a convection cell, the mean velocity profile has an invariant shape while varying Ra . Furthermore, the BL thicknesses were scaled as $\delta_{v1} \sim \text{Ra}^{-0.16}$ and $\delta_{v2} \sim \text{Ra}^{-0.25}$. The viscous BL thicknesses were defined by two methods, respectively by the intersection value of the maximum mean velocity with the linear velocity gradient at the wall (δ_{v1}) and the maximum mean standard deviation with the linear standard deviation gradient (δ_{v2}). Further velocity and temperature profile measurements in water using LDA were reported by X. L. Qiu and P. Tong (2001) [42], who studied the large-scale velocity structures at $\text{Ra} = 10^9$ and found the flow could be divided into three regions in the rotation plane: thin viscous BL, fully mixed central core and intermediate plume-dominated buffer layer. Sun *et al.* (2008) [43] studied the BL profiles using particle image velocimetry (PIV) measurement and have found that the model of a laminar BL predicted by Prandtl and Blasius is a good approximation for the velocity BL in turbulent RB convection at varying Ra from $\text{Ra} = 10^9$ to $\text{Ra} = 10^{10}$ and at a fixed $\Gamma = 4.3$. However, one has to keep in mind that because of the large Pr of water, the thermal BL is much thinner than the viscous one. Therefore it was difficult to get a high spatial and temporal resolution of the data.

Summarizing all the discussed results in the field, an investigation, which fulfills all the measuring conditions, at high Ra , obeying high spatial and temporal resolution and providing three-dimensional velocity data is still missing. In the BLs, acquisition of all velocity components is equally important, since all theoretical near-wall models are two-dimensional and fail in the presence of strong cross-stream flows. Furthermore, the intermittent emissions of thermal plumes from the BLs require long

1 Introduction

enough measurement time periods. The LDA is an ideal tool to measure the local multi-component velocity accurately and non-intrusively. This method could help answer the question of whether the BL can be described with a turbulent or a laminar model. While the theory by Shraiman and Siggia [44, 45] builds on existing turbulent BLs close to the isothermal plates, Grossmann and Lohse [31, 46] assumed a Prandtl-Blasius-type BL [47]. In this thesis, 3D LDA velocity measurements with high spatial and temporal resolution and temperature measurements using micro thermistor are applied in highly turbulent RB convection. These experiments as well as joint DNS high-resolution BL analysis will allow us to compare our findings with the assumptions and provide a further motivation to the present work.

Numerous investigations have been done to refine the existing BL and LSC models for RB convection. Appropriate velocity and temperature profile measurements in water using LDA were reported in Qiu and Tong [42], who studied the LSC of the flow at $Ra = 10^9$. Later Sun, Cheung and Xia [43] and Zhou and Xia [48] studied the BL profiles by PIV for thermal convection in water at $Pr = 4.3$. They found that the Prandtl-Blasius solution is a good approximation for the velocity BL for Rayleigh numbers between 10^9 and 10^{10} . Their rectangular convection cell was, however, very narrow in the third direction, such that the LSC is confined to a quasi-two-dimensional flow. BL measurements for convection in air up to a $Ra = 10^{11}$ have been conducted with a two-component LDA measurement [17, 18]. In these experiments deviations from the Prandtl-Blasius case were detected. Three aspects improve the agreement with the classical Prandtl-Blasius theory: the switch to a quasi-two-dimensional experiment or two-dimensional DNS that constrains the LSC, an increase in the Prandtl number and a rescaling by an instantaneously defined BL thickness. All these directions in various combinations have been discussed in [48, 49].

In recent years, a number of DNS were conducted to study the BL. Recent 3D DNS for Rayleigh numbers up to 2×10^{12} found however that the differences compared with the Prandtl-Blasius solution grow for the BL profiles of the temperature field [50]. The 3D numerical studies of the BL structure by Shi *et al.* [1] found that even with a dynamical rescaling of both the velocity and temperature data by an instantaneously defined BL thickness, the deviations from the Prandtl-Blasius-Pohlhausen theory still exist. However at the same $Pr = 0.7$ and $\Gamma = 1$, the numerical study of Scheel *et al.* found that the viscous boundary profiles up to $Ra = 1 \times 10^9$, scaled with the similarity variable BL thickness, do agree with the Prandtl-Blasius profile [51]. In contrast, the thermal BL profiles disagree with the prediction by more than 10%.

The experimental studies of the velocity and temperature profiles as discussed above were done separately, but in RB convection the velocity and the temperature field are generally coupled in the BL, so it is very important to measure them simultaneously. The first recent simultaneous measurements were conducted in a cylindrical convection cell filled with water by Xia and Tong in 2003, 2004 [52, 53]. The velocity and temperature measurements were carried out with LDA and thermistor probe, at $\Gamma = 1$, $9.8 \times 10^8 < Ra < 7.6 \times 10^9$ as well as at $\Gamma = 0.5$, $Ra \leq 5.9 \times 10^{10}$. They found that the local convective heat flux is mainly orientated in the vertical direction. The flux is primarily determined by the thermal plumes in the system. The heat transport analysis inside the BL was still missing. In this thesis, the size of the thermistor probe is much smaller with a diameter $125 \mu\text{m}$ current instead of $200 \mu\text{m}$ earlier. We have optimized the spatial separation between LDA measurement volume and thermistor tip to 0.3 mm (earlier measurement was with $0.7 \pm 0.2 \text{ mm}$) to have stronger cross-correlation between velocity and temperature data. The thicker BL of our convection cell (BOI at $Ra = 10^{10}$ with $\delta = 10 \text{ mm}$) allow us simultaneous velocity and temperature measurements both inside and outside the BL with much better spatial resolution.

1.4 Outline of the thesis

The outline of this thesis is as follows. In chapter 2, the basics of RB convection are introduced. In chapter 3, we introduce the Barrel of Ilmenau, the world's largest Rayleigh-Bénard convection facility. In chapter 4, laser Doppler anemometry with 3D measurement technique and the micro thermistor temperature probe are described. In chapter 5, the results of the mean velocity and temperature profiles and their fluctuations in the small convection cell (inset of the BOI) are introduced. We compare experimental data at $Ra = 3.44 \times 10^9$, $\Delta T = 2.4 \text{ K}$, with DNS data at $Ra = 3 \times 10^9$. Furthermore, experimental data at $Ra = 2.88 \times 10^{10}$, $\Delta T = 20 \text{ K}$, are compared with DNS data at $Ra = 3 \times 10^{10}$. This chapter also includes BL analysis from other experimental data records in order to discuss trends for the scaling of the BL thickness and shear Reynolds number in a range of Rayleigh numbers varying from $Ra = 3.44 \times 10^9$ to $Ra = 9.97 \times 10^{11}$. These studies are followed by investigations of the large-scale circulations, the mean angle of its rotation. In chapter 5, additionally the velocity and temperature profiles at aspect ratio $\Gamma = 2.76$ are presented. In chapter 6, we present the local heat flux calculated by the simultaneously-measured velocity and temperature fluctuations at $Ra = 8.96 \times 10^{11}$, $\Delta T = 50 \text{ K}$, $\Gamma = 1.13$. In chapter 7, the measuring uncertainty is investigated and discussed. In the conclusion, a summarization of the work and its possible extensions are given.

2.1 Basic equations and parameters

In this chapter, the classic statement of the RB problem will be described. We start from the relevant parameters, then we trace back these parameters from the Boussinesq equations. The dimensionless Rayleigh number (Ra), is the most important parameter and characterizes the relation between buoyancy and friction force. With this parameter we can calculate the onset of thermal convection and it is defined as:

$$\text{Ra} = \frac{\alpha g \Delta T H^3}{\nu \kappa}, \quad (2.1)$$

where α is the thermal expansion coefficient, g is the acceleration due to gravity, ν is the kinematic viscosity, κ the thermal diffusivity, H is the distance between the heating and cooling plates and ΔT is the temperature difference between the heating and cooling plates. The Prandtl number (Pr) describes the molecular transport in the working medium and is purely a material property. It is a ratio of momentum diffusivity (kinematic viscosity) to thermal diffusivity. Thus the Prandtl number is defined as:

$$\text{Pr} = \frac{\nu}{\kappa}. \quad (2.2)$$

To describe the geometry of the convection cell, another dimensionless number is introduced, the aspect ratio Γ . In a cell, it corresponds to the ratio between the diameter D and the distance H between the heating and cooling plate:

$$\Gamma = \frac{D}{H}. \quad (2.3)$$

2 Basics of the Rayleigh-Bénard Convection

In response to the sustained temperature difference a turbulent flow with a Reynolds number (Re) is established:

$$\text{Re} = \bar{v}H/\nu. \quad (2.4)$$

This flow enhances the transport of heat far beyond the level that is possible by thermal diffusion. The Nusselt number quantifies exactly this ratio and is defined as:

$$\text{Nu} = (4H\dot{q}_c)/(\lambda_{th}\pi D^2\Delta T). \quad (2.5)$$

In these definitions variables stand for the following physical quantities: \bar{v} for mean velocity, \dot{q}_c for convective heat flux and λ_{th} for the thermal conductivity.

Generally the RB convection can be described by the Oberbeck-Boussinesq equations consist of the Navier-Stokes equation, the heat equation and the mass conservation. The original meaning of the Boussinesq effect is as follows: The fluid density ρ is considered to be independent on pressure (i.e. incompressibility is assumed) and to depend linearly on the temperature T:

$$\rho - \rho_0 = -\rho_0\alpha(T - T_0) \quad (2.6)$$

Additionally, it is assumed that the material properties of the fluid such as thermal expansion coefficient α , the viscosity ν and the thermal diffusivity κ are independent on the temperature and constant. By the temperature difference $\Delta T = T_h - T_c$ generated density difference causes a buoyancy force and sets the fluid in motion. Warm fluid rises, while cold fluid sinks to the bottom and thus creates complex structures in the coupled velocity temperature system.

By the Boussinesq approximation, the momentum balance (2.6) can be simplified as follows:

$$\frac{\partial \vec{v}}{\partial t} + (\vec{v} \cdot \nabla) \vec{v} = -\frac{\nabla p}{\rho_0} + \nu \nabla^2 \vec{v} - g[1 - \alpha(T - T_0)] \quad (2.7)$$

where \vec{v} is the velocity, g is the gravitational acceleration, and p is the pressure. With the assumption that the air in the RB-cell is incompressible, the mass balance can be written as:

$$\nabla \cdot \vec{v} = 0 \quad (2.8)$$

Finally, we are still using the energy equation, which describes the temperature field, the equation of energy conservation:

$$\frac{\partial T}{\partial t} + (\vec{v} \cdot \nabla) T = \kappa \nabla^2 T. \quad (2.9)$$

There are several ways for the nondimensionalization, we introduce one of them as an example. We proceed as:

$$t' = \frac{t}{\tau_v}, \tau_v = \frac{H^2}{\kappa} \quad (2.10)$$

$$\vec{v}' = \vec{v} \left(\frac{H}{\kappa} \right) \quad (2.11)$$

$$T' = \frac{T}{\Delta T} \quad (2.12)$$

$$\frac{p'}{\rho_0'} = \frac{p}{\rho_0} \left(\frac{H^3}{\kappa^2} \right) \quad (2.13)$$

Hence, (2.7) - (2.9) become:

$$\frac{\partial \vec{v}'}{\partial t'} + (\vec{v}' \cdot \nabla) \vec{v}' = -\frac{\nabla p'}{\rho_0'} + \frac{\nu}{\kappa} \nabla^2 \vec{v}' - \frac{g\alpha \Delta T H^3}{\kappa^2} (T' - T_0') \quad (2.14)$$

$$\frac{\partial T'}{\partial t'} + (\vec{v}' \cdot \nabla) T' = \nabla^2 T' \quad (2.15)$$

$$\nabla \cdot \vec{v}' = 0 \quad (2.16)$$

and drop all the primes then we obtain following form:

$$\frac{\partial \vec{v}}{\partial t} + (\vec{v} \cdot \nabla) \vec{v} = -\frac{\nabla p}{\rho_0} + \frac{\nu}{\kappa} \nabla^2 \vec{v} + \frac{\nu g \alpha \Delta T H^3}{\nu \kappa^2} (T - T_0) \quad (2.17)$$

If we substitute Ra (2.1), Pr (2.2) and the pressure $P = p/\rho_0$, another form of the equation is written down:

$$\frac{\partial \vec{v}}{\partial t} + (\vec{v} \cdot \nabla) \vec{v} = -\nabla P + Pr \nabla^2 \vec{v} + Pr Ra (T - T_0) \quad (2.18)$$

$$\frac{\partial T}{\partial t} + (\vec{v} \cdot \nabla) T = \nabla^2 T \quad (2.19)$$

$$\nabla \cdot \vec{v} = 0 \quad (2.20)$$

2.2 Large-scale circulation (LSC) and formation of boundary layers

The basic RB system in the nature is of infinite extent. In the model experiment, the side-walls are unavoidable, therefore the large-scale circulation is developed. The LSC is an important mechanism of heat transfer and was the objective of many experiments in the past [2, 5, 10, 24, 54, 55]. The structure and dynamics of the LSC in the large cylindrical facility depends on the aspect ratio. In this chapter, we focus on the cell with $\Gamma = 1$, because for this condition the flow geometry is a fully dynamically developed single roll. It has near-elliptical stream lines and maintains itself on a slightly tilted circulation plane with up-welling warm plumes and down-welling cool plumes detaching from the

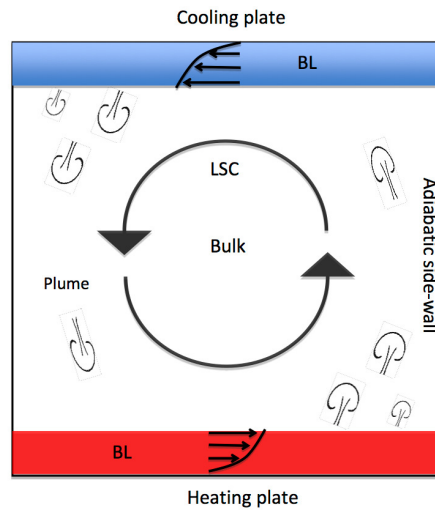


Figure 2.1: The large-scale circulation with a typical mean flow, which is maintained by the up- and down-welling plumes detaching permanently from the BLs.

BLs, as shown in the mean velocity profiles measured at various locations [20]. The plumes initiate the mean wind and are as well maintained by it in a self-organizing process [56, 57]. The motivation of LSC theory is that the whole thermal convection system is split into three regions: BLs, LSC, also called wind and a bulk region, see sketch 2.1. The spatial and temporal dynamics at large scales is complicated. For a long time, they have been considered as a locally fixed flow structure. Nowadays, the LSC is found to have periodic oscillations [15]; the LSC direction near the plates is found to horizontally oscillate with a typical time scale very similar to the large eddy turnover time. It is also known to have sudden and periodic reversals, rotations and cessations [58, 59, 60]. Due to these complex behaviors, the LSC has a direct effect on the BL structure. Our work is aiming to characterize the flow field in the near-wall fluid layer and also to study the influence of the dynamics of the LSC on the BL structure.

2.3 Blasius and Pohlhausen solutions of the boundary layer equations

Since the global heat transfer is intimately related to the physics of the BLs, almost all scaling theories are based on assumptions for the BLs, in order to derive relations for Nu as a function of Ra (and Pr). Therefore it is very important to verify whether the BL theoretical predictions do or do not fit the experimental findings. We might expect a solution of RB convection BL, indeed the velocity or temperature profile maintains a constant shape. But in the thermal convection, the BL behaves far beyond that which we can make an exact solution. It is usually recommended that the Prandtl-Blasius solution [61], which describes the steady two-dimensional BL that forms on a semi-infinite plate which is held parallel to a

constant unidirectional flow, be compared with RB velocity profile in the BL.

In figure 2.2, the longitudinal velocity of the flow grows along the length of the plate from $u = 0$ to $u = u_\infty$. After some length, the orderly flow (shear flow) separates from the layer with small transversal velocity components into a less-ordered turbulent-flow with random velocity fluctuations, with a thicker boundary layer and a much thinner laminar sub-layer close to the wall. We may arbitrarily set the thickness of the boundary layer δ , as that where $u = 0.99u_\infty$ and we want to know its growth rate, $\delta(x)$. The equations governing the laminar and steady flow over a flat plate, with constant density and without gravity effects are as follow:

$$\frac{\partial u}{\partial x} + \frac{\partial v}{\partial y} = 0 \longrightarrow \frac{u_\infty}{L} \approx \frac{v}{\delta} \quad (2.21)$$

$$u \frac{\partial u}{\partial x} + v \frac{\partial u}{\partial y} = \nu \left(\frac{\partial^2 u}{\partial x^2} + \frac{\partial^2 u}{\partial y^2} \right) \longrightarrow \frac{u_\infty^2}{L} \approx \nu \frac{u_\infty}{\delta^2} \quad (2.22)$$

$$u \frac{\partial v}{\partial x} + v \frac{\partial v}{\partial y} = -\frac{1}{\rho} \frac{\partial p}{\partial y} + \nu \left(\frac{\partial^2 v}{\partial x^2} + \frac{\partial^2 v}{\partial y^2} \right) \longrightarrow \frac{\delta}{L} \frac{u_\infty^2}{L} \approx \frac{\partial p}{\partial y} \quad (2.23)$$

where the order-of-magnitude analysis has also been performed. The continuity equation shows that transversal velocities are much smaller than longitudinal velocities. The longitudinal momentum balance shows that the thickness ratio, δ/L , is of order $(u_\infty L/\nu)^{-1/2}$, *i.e.* $\delta/L \approx \text{Re}^{-1/2}$. Blasius found in 1908 the exact solution by introducing a self-similar variable, $\eta_{PB} \equiv y(u_\infty/(vx))^{1/2}$, that transforms the partial differential equation (PDE) function into an ordinary differential equation in the auxiliary function, $\psi(\eta_{PB}) = (u_\infty vx)^{1/2} f(\eta_{PB})$ with $f(\eta_{PB}) \equiv \int (u/u_\infty) d\eta_{PB}$, the equations being:

$$2 \frac{d^3 f}{d\eta_{PB}^3} + f \frac{d^2 f}{d\eta_{PB}^2} = 0 \quad (2.24)$$

$$f|_{\eta_{PB}=0} = 0 \quad (2.25)$$

$$\left. \frac{df}{d\eta_{PB}} \right|_{\eta_{PB}=0} = 0 \quad (2.26)$$

$$\left. \frac{df}{d\eta_{PB}} \right|_{\eta_{PB}=\infty} = 1 \quad (2.27)$$

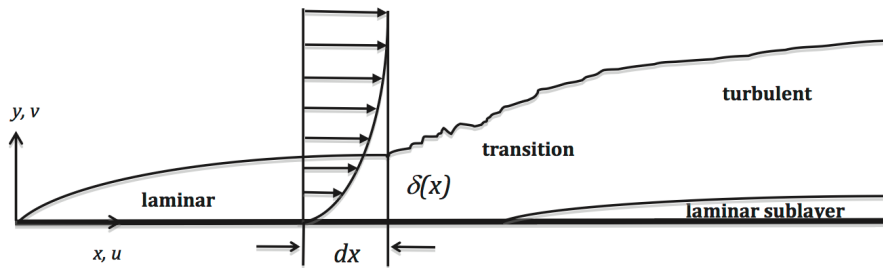


Figure 2.2: Structure of the boundary layer flow over a flat plate.

2 Basics of the Rayleigh-Bénard Convection

which, although not analytically integrable, has a universal solution easily computed numerically. The longitudinal speed fraction $u/u_\infty = \partial f / \partial \eta_{PB}$ asymptotically grows from 0 to 1 at infinity, attaining a precise value of 0.99 for $\eta_{PB} = 4.92$. Thus, the height at which $u = 0.99u_\infty$, BL thickness grows parabolically as $\delta = 4.92(vx/u_\infty)^{-1/2}$. The BL thickness δ also can be defined by 95% of the free stream velocity as well as displacement thickness, then BL thickness can be defined as $\delta = 3.92(vx/u_\infty)^{-1/2}$ and $\delta = 1.72(vx/u_\infty)^{-1/2}$ respectively.

The Pohlhausen solution builds on the Prandtl-Blasius solution for the laminar BL and assumes that the temperature is passively advected in the flow. For the use of Pohlhausen's solution, all fluid properties, such as kinematic viscosity, thermal conductivity and Pr are again assumed to be constant. It is a Pr dependent governing equation of the temperature distribution of the flat plate flow and is usually recommended to be compared with RB convection temperature profile in the BL. In this dissertation, we compare the mean velocity and temperature profiles with these two solutions at different Rayleigh numbers and aspect ratios at various locations.

3.1 RB convection facility “Barrel of Ilmenau” (BOI)

All velocity and temperature measurements were conducted in the BOI - a large-scale RB experiment (see Fig. 3.1). We used air as the working fluid and performed our experiments in a closed cylindri-

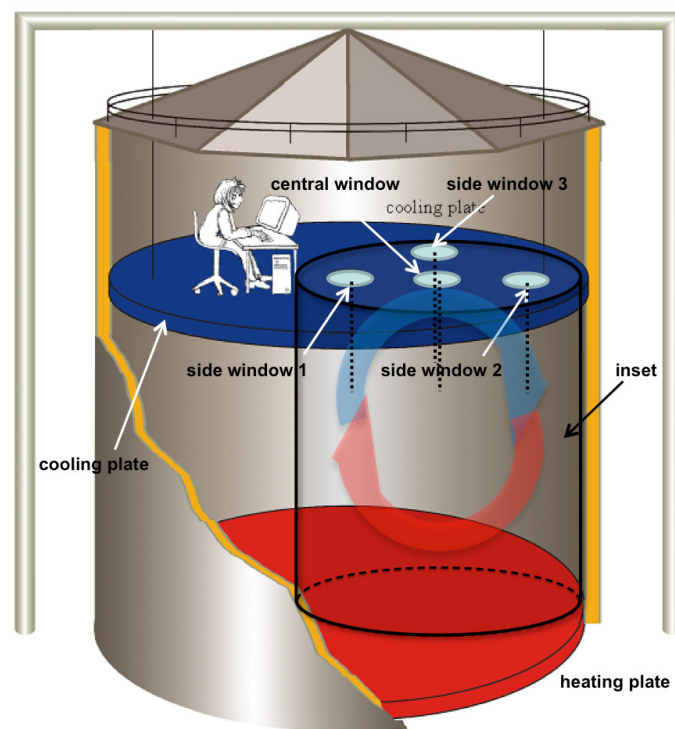


Figure 3.1: Sketch of “Barrel of Ilmenau” with the inset cell of 2.5 m height and 2.5 m diameter. In this work we will take measurements at the central window (the center line) and the side windows 1, 2 and 3.

3 Experimental apparatus

cal box with an inner diameter $D = 7.15$ m, a heating plate at the bottom and a free-hanging cooling plate above. The distance between the heating and cooling plates is continuously adjustable between $H = 0.063$ m and $H = 6.30$ m. The plates are aligned perpendicularly to the vector of the gravitational acceleration, with a deviation smaller than 0.1° . In order to force the convective flow into a certain direction the cooling plate can be inclined to an angle of up to approximately 5° , but we did not make use of this possibility in the experiments. The side-wall is covered with an active compensation heating system, which is necessary to suppress lateral heat losses to the environment. The box is filled with ambient air (about 250 m^3 for $\Gamma = 1.13$). Two side windows, each with a diameter of 1.00 m and shielded with a separate compensation heating segment can be used for global observation and access for maintenance.

Because our interest was focused on the investigation of the temperature and the velocity field in the vicinity of the cooling plate, we had to guarantee very precise boundary conditions there, the homogeneity of temperature. A relatively low weight and a good homogeneity of the temperature distribution of the cooling plate can be obtained by a water-cooled aluminum plate, made of 16 separate segments, each covering a sector of angle 22.5° . All segments consist of a lower blank smooth aluminum plate with a thickness of 6 mm, followed by a cooling-coil system with 25 mm tubes and a second aluminum plate on top. The segments are mounted on a steel rack with total weight of approximately 5 tons, which hangs at three hoists in a steel construction. Each segment of the cooling plate is supplied with cooled water by a central cooling system with a maximum power 13 kW, see figure 3.2 [62]. A proportional-integral-derivative controller (PID controller) in combination with a 1 m^3 buffer tank in the cooling circuit guarantees a very stable temperature. The temperature can be adjusted between 15°C and 25°C . The accuracy is better than $\pm 0.1^\circ\text{C}$. In order to achieve intense lateral heat transport and a homogeneous temperature distribution at the plate surface, the highest possible flow rate of approximately $10 \text{ m}^3/\text{h}$ was chosen and each segment was supplied separately. The surface temperature of the cooling plate is continuously measured and stored by 19 high-accuracy PT-100 temperature sensors, mounted in holes drilled from the upper site of the plate to about 0.5 mm from its lower surface. Nine sensors are arranged at the ninth segment opposite to the lower maintenance window in a line from the centre of the plate to its outer edge. They give information about the radial distribution of temperature. The other sensors are distributed regularly over the remaining segments. The mean temperature of the cooling plate, \bar{T}_{CP} , which we use for the determination of Ra and for the presentation of non-dimensional temperature profiles is obtained as an average over every second segment.

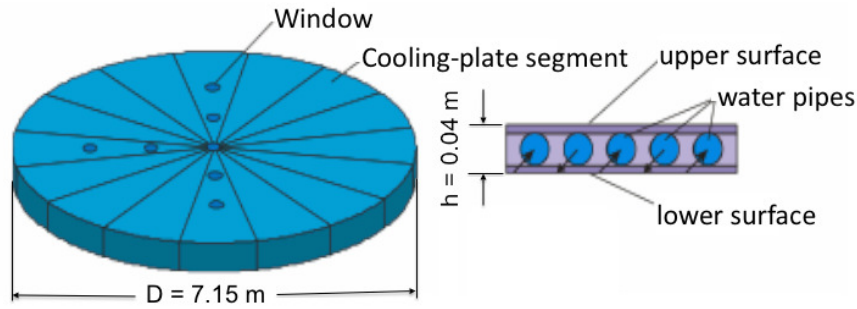


Figure 3.2: Construction of cooling plate of the BOI, with 16 separate segments (on the left) and the cross section of an individual segment (on the right) [62].

The bottom heating plate consists of two layers. On the ground is the earlier built electrical underfloor heating system embedded in a 5 cm concrete layer and isolated to the ground with 30 cm polyurethane plates. Electrical heating wires are mounted in a spiral form at a metal gauze and fixed at the surface of the insulation layer. On top of this electrical heating floor, an aluminum plate with water circulation system, which is very similar to the cooling plate, is set up. The water circulation inside the aluminum heating plate and its smooth surface sustain the homogeneity of the temperature distribution and balance differences of the convective heat flux at the plate-air interface. Both layers are thermally coupled by a 2 mm silicon pad. Temperature sensors in an arrangement, which is shown in figure 3.3 [14], are embedded in the cooling plate. They are mounted in holes drilled from the lower site of the plate to about 0.5 mm from its upper surface. The electrical heating system is divided into three concentric sectors with equal areas. The surface temperature of every sector is separately controlled by a PID controller. A mean surface temperature \bar{T}_{HP} between 80°C and 20°C with an accuracy better than $\pm 0.02\text{ K}$ can be adjusted. In figure 3.3, an example from a recent paper [14] of our group, the temperature at the heating plate has been adjusted in a range between $T = 31.2^{\circ}\text{C}$ and $T = 58.2^{\circ}\text{C}$. The different levels of temperature homogeneity of the heating and cooling plate are illustrated in this figure. The deviation of any local temperature at the surface from the global mean temperature was typically less than $\pm 1\%$ of the total temperature drop between the plates ($\pm 1.5\%$ at the cooling plate).

In case of a perfectly adiabatic side-wall the heat flux through it has to be zero. The side-wall of the BOI is shielded by an active compensation heating system to prevent a heat exchange with the surroundings. Electrical heating elements are arranged between an inner and outer isolation. The temperature of these elements is controlled to be equal to the temperature at the inner surface of the side-wall [14].

The side-wall of the experimental facility consists of an inner insulation layer 16 cm thick followed by

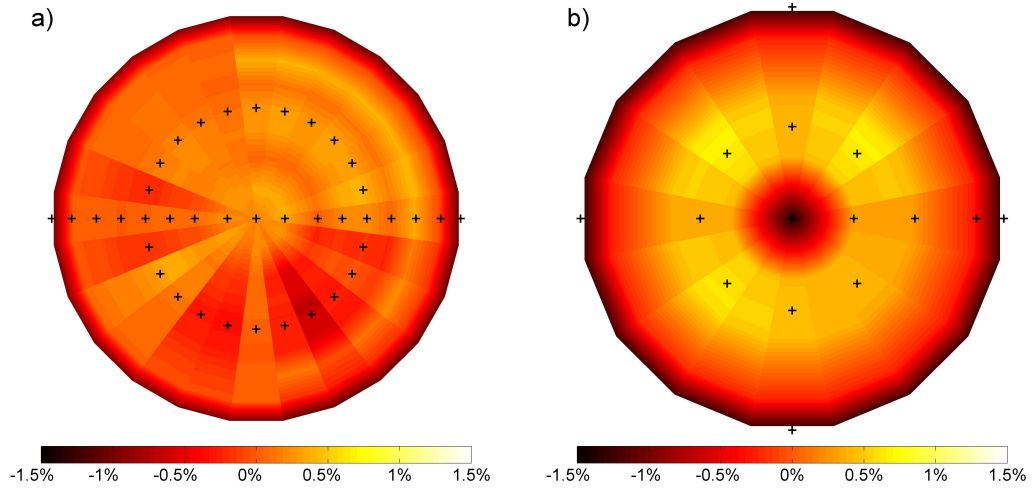


Figure 3.3: Temperature distribution at the surface of the heating plate (a) and the cooling plate (b) at $T_h - T_c = 35.2$ K, $\Gamma = 2.75$ and $Ra = 5.2 \times 10^{10}$. The plots show the relative deviation $\Delta T_h = 100 [T_h(x, y) - T_h]/[T_h - T_c]$ and $\Delta T_c = 100 [T_c - T_c(x, y)]/[T_h - T_c]$ in percent of the total temperature drop between the plates. The crosses indicate the position of internal temperature sensors. The radial temperature distribution at each segment is a projection of the measured distribution along the horizontal line whereas the angular distributed temperature sensors are used as basic values. Figure taken from [14].

compensating heating elements and an outer insulation layer with thickness 12 cm. The inner insulating wall is made of five rings of height 1.60 m, each mounted on three 120° sections. They consist of an inner and an outer layer of a very stable fiber-reinforced plastic (of thickness 1 cm) as well as an intermediate insulation layer of polyurethane. The heat resistance R_{th} of this simple wall is of the order of 0.04 K/W and leads to a maximum heat loss $\dot{q}_w = 1.5$ kW through the side-wall. The compensation heating system at the outer surface, covered with additional thermal insulation and finished with an outer weather-resistant plastic board, reduces this heat loss by a factor of about 20. In relation to the convective heat flux at the maximum Ra ($Ra = 10^{12}$) the lateral heat loss amounts to less than 1%. To avoid computation of a Ra based on the non-uniform bottom temperature, we define our experimental Ra as

$$Ra = \frac{2\alpha g(T_B - T_{CP})H^3}{\nu\kappa}. \quad (3.1)$$

where T_B is the measured bulk temperature averaged over the time of the profile measurement. All fluid properties are evaluated for this temperature. More details on the facility can be found in Refs. [4, 17, 18, 62].

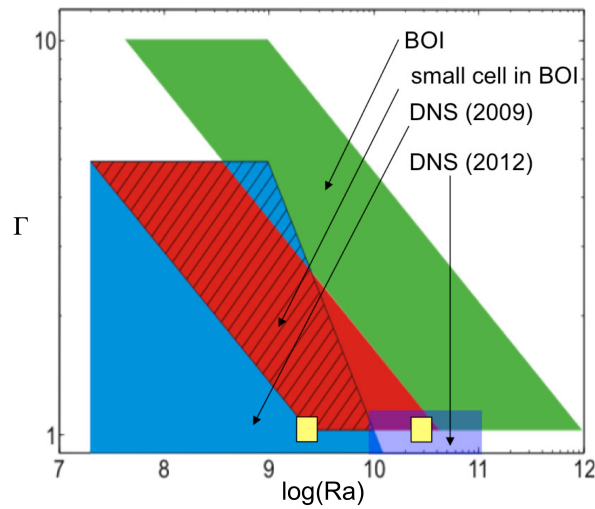


Figure 3.4: Accessible parameter range in Ra versus Γ for the Barrel of Ilmenau (green), and the inset cell (red). The accessible range of the direct numerical simulation (DNS) is given in blue. The yellow dots mark the parameter sets (Ra, Γ) at which the measurements were compared directly with the results from the DNS [1].

3.2 Small convection cell for 3D velocity and temperature measurements built in the large convection cell

The lowest accessible Ra in the big barrel at aspect ratio one is $Ra_{min} = 5 \times 10^{10}$, which is still larger than the maximum Ra in the numerical simulations, $Ra_{sim} = 3 \times 10^{10}$. The common parameter range of both experiment and DNS is shown in figure 3.4. In order to match the experimental parameters to those from the DNS for the case of $\Gamma = 1$, a cylindrical inset with a diameter of 2.5 m and a height of 2.5 m has been installed between the heating and the cooling plates. The surrounding environment of the smaller cell has the same temperature difference as the inside volume of the BOI. Thus no thermal exchange across the side-walls is present and the adiabatic side-wall boundary condition is very well established. The first separately measured velocity and temperature using LDA and micro thermistor were conducted in this small convection cell. Finally a 1:1 numerical model was made for the comparison between measurements and DNS at various locations [1]. Four measuring windows are located at different positions of the cooling plate (see Fig. 3.1) permitting access for the optical device and the temperature sensor. In order to lock the orientation of the “wind”, the inset cell was stretched slightly along the line connecting the three windows, window 1, central window and window 2. The results will be systematically discussed in the chapter 5.

4.1 Velocity field measurements using laser Doppler anemometry (LDA)

4.1.1 LDA introduction and measurement principles

There are mainly three popular techniques which have been applied for flow measurements, hot wire anemometry, particle image velocimetry (PIV) and laser Doppler anemometry (LDA). The hot wire anemometry needs a constant ambient temperature and is not suitable working in high temperature field gradient. PIV is predestined for instantaneous flow field investigations but not for single-point measurements. LDA features many apparent advantages such as non-intrusive, directional sensitivity, high spatial and temporal resolution due to small measurement volume. Because of its high accuracy, LDA became a frequently used measurement technique in fluid mechanics. Especially for the BL investigation, the small size of the measurement volume of LDA is the best tool to fit our purpose.

The first LDA, known as the reference-beam mode, was introduced by Yeh and Cummins in 1964 [63]. The modern dual-beam mode LDA, which we are using in our research, was presented by Lehmann in 1968 [64] and von Stein and Pfeifer in 1969 [65]. The principle of LDA, shown in figure 4.1, is based on the interaction of two laser beams. They are generated from one source by a beam splitter. One beam passes through a Bragg cell which modulates the wave fronts with 40 MHz, resulting in a constant movement of the interference fringe pattern described below, such that the direction of the velocity can be distinguished. These two beams are focused by a front lens and form a measurement volume wherein an interference fringe pattern is generated. A particle in the flow, for example a dust particle traveling through the measurement volume causes the scattering of laser light, which is detected by a

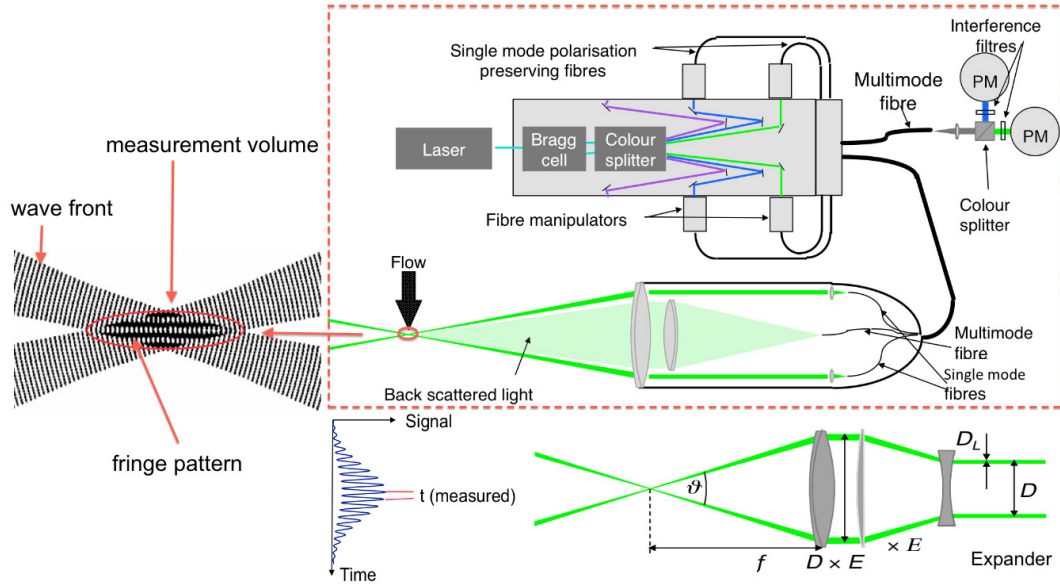


Figure 4.1: LDA principle and configuration of transmitter and receiver [66].

photomultiplier and transformed into an electric signal. The light scattering signal at the receiver is called a LDA burst. The time interval between the peaks within a burst contains the desired information about the speed of the particle. The velocity is measured perpendicular to the direction of the interference stripes. In the present case, the receiver unit is combined with the transmitting unit. This is known as the backscattering configuration, because the scattered light is measured opposite to the irradiation direction. On our LDA probe, a beam expander is used to make the beam diameter large in order to decrease the measurement volume as well as to increase the scattered light intensity. The LDA system we are using is a commercial system, from Dantec Dynamics company.

A critical parameter of the LDA system is the size of the measurement volume, since this quantity defines the spatial resolution of the velocity measurement. The crossing laser beams generate the measurement volume, which has a Gaussian intensity distribution in all three dimensions. The measurement volume is an ellipsoid, see figure 4.2. Its height d_{mv_x} , width d_{mv_y} and length l_{mv_z} are given by the $1/e^2$ laser light intensity level. They can be calculated, if the beam angle θ and beam diameter D_L are known.

$$\text{Height : } d_{mv_x} = \frac{4f\lambda}{\pi E D_L \cos(\theta/2)} \quad (4.1)$$

$$\text{Width : } d_{mv_y} = \frac{4f\lambda}{\pi E D_L} \quad (4.2)$$

$$\text{Length : } l_{mv_z} = \frac{4f\lambda}{\pi E D_L \sin(\theta/2)} \quad (4.3)$$

Within the measurement volume, the numbers of fringes and the fringe spacing can be calculated as

4.1 Velocity field measurements using laser Doppler anemometry (LDA)

| | green-2D | blue-2D | dark green-1D |
|-------------------------------------|----------|---------|---------------|
| | 514.5 nm | 488 nm | 532 nm |
| Height d_{mv_x} (μm) | 72.3 | 75.2 | 81.4 |
| Width d_{mv_y} (μm) | 72.1 | 75.0 | 80.82 |
| Length l_{mv_z} (μm) | 967 | 1016.2 | 1059.12 |

Table 4.1: Dimensions of measurement volume with $f = 500$ mm front lens. Two probes combined a 3D LDA set-up, includes a pair of green beam (2D probe), a pair of blue beam (2D probe) and a pair of dark green beam (1D probe)

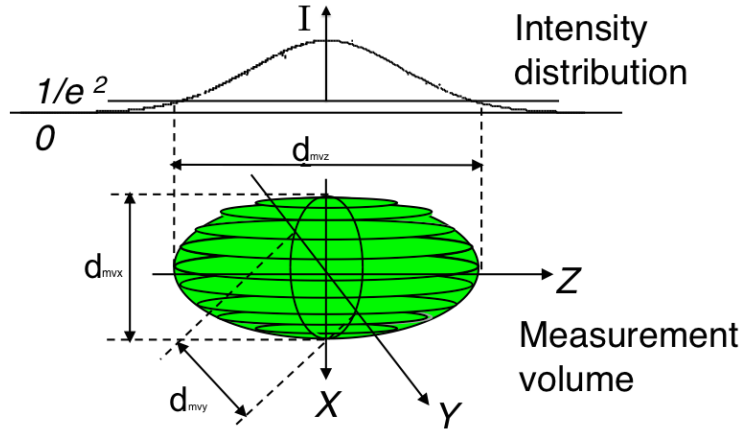


Figure 4.2: Three-dimensional LDA measurement volume in the intersection point of two laser beams.

follow:

$$\text{Fringe separation} : d_f = \frac{\lambda}{2 \sin(\theta/2)} \quad (4.4)$$

$$\text{Number of fringes} : N_f = \frac{8f \tan(\theta/2)}{\pi E D_L} \quad (4.5)$$

The quantities are: f - is the focal length of the front lens. λ - is the laser wavelength. θ - is the beam intersection angle. E - is the expander ratio. D_L - is the beam waist at $1/e^2$ intensity drop.

We have checked the size of the measurement volume by using a laser beam diagnostic method based on the rotating wire principle, shown in figure 4.7. If we take the e^{-2} intensity level of the Gaussian distribution of the laser beam intensity, the size of the measurement volume is shown in table 4.1 for a front lens with focal length $f = 500$ mm.

4.1.2 LDA seeding particles

The LDA measurement relies on the light scattering properties of particles. They should not only follow the flow faithfully, but also exist in a sufficient density in order to provide reliable velocity data. In the air flow, the cold-atomized droplets of Di-Ethyl-Hexyl-Sebacat (DEHS) have been injected through an opening in the convection cell. They serve as tracers for the LDA measurement and are basically free of inertia. The number distribution of DEHS droplets generated by a Palas aerosol generator AGF 2.0 at three different volume flows is shown in figure 4.3. Most of the particles exist for a radius of $0.25 \mu\text{m}$. In our work, the aerosol generator AGF 10.0 was used with an air pressure between 0.5 and 1.0 bar. According to the information from the Palas manual [67], the AGF system consists of an adjustable binary nozzle for the adjustment of the desired mass flow as well as of a cyclone for the filtration of particles, *e.g.* the diameter larger than $2 \mu\text{m}$ for the AGF 2.0 or larger than $10 \mu\text{m}$ for the AGF 10.0 will be

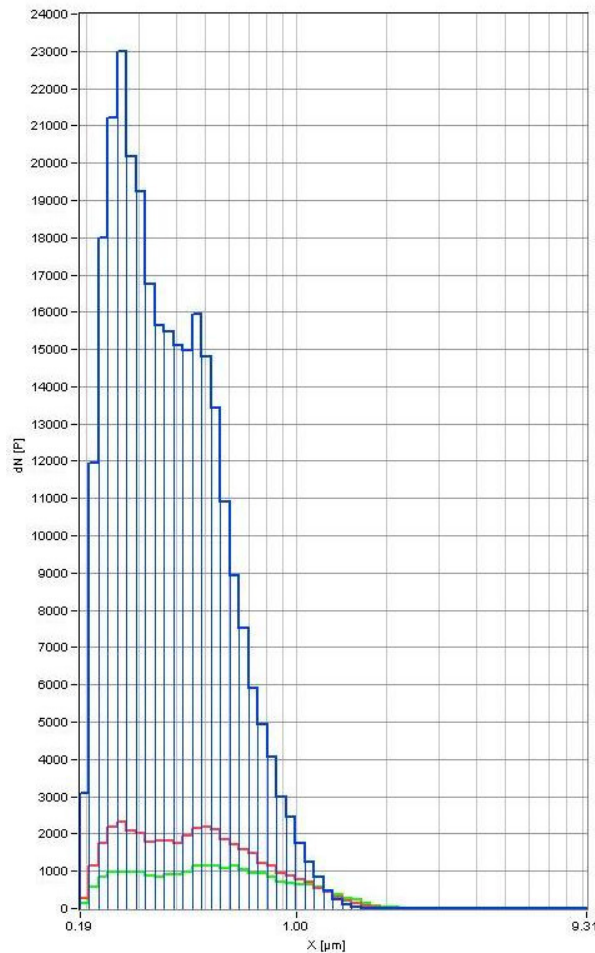


Figure 4.3: Number distribution of DEHS droplets generated by AGF 2.0 at three different volume flows. [67]

4.1 Velocity field measurements using laser Doppler anemometry (LDA)

removed. In the case of AGF 10.0, the number distribution curve, figure 4.3 is shifted to larger particle diameters. In the table of figure 4.4, the average diameter of the DEHS particles generated by the AGF 10.0 is given with $0.5 \mu\text{m}$ (For the focal length $f = 500 \text{ mm}$, the measurement volume contains ≈ 37 fringes with a spacing of $\approx 3.60 \mu\text{m}$).

How well the particles are following the flow can be determined by the Stokes number St . DEHS particles are perfect Lagrangian tracers when $St \ll 1$. St is defined as follows:

$$St = \frac{t_r}{t_c} \quad (4.6)$$

$$t_r = \frac{\rho_p d_p^2}{18\mu} \quad (4.7)$$

$$t_c = \frac{l_c}{v_c} \quad (4.8)$$

In the equations, t_r is the particle response time in the turbulent flow, t_c is a characteristic time scale of the flow, ρ_p is the density of DEHS (800 kg/m^3), d_p is the diameter of the particle ($1 \mu\text{m}$), μ is the dynamic viscosity of air ($1.7 \times 10^{-5} \text{ Pa} \cdot \text{s}$ at room temperature), l_c is the characteristic length scale of the flow (1 mm, the Kolmogorov length scale is taken) and v_c is the characteristic mean velocity of the flow (0.5 m/s). When all the values are inserted in equations (4.6) - (4.8), it follows that St is equal to 10^{-3} , which is much smaller than 1. It means that the DEHS particles follow the turbulent flow sufficiently well and can be considered as passive tracers.

Due to the fact that the particle seeding rate is determined by the requirements of the data processing, such as data interpolation, we try to sustain a sufficient concentration for a 100 Hz burst frequency on average. Keep in mind that the concentration also depends on the distance to the wall. In order to obtain

| | Dimensions WxHxD mm | Weight kg | \dot{V} l/min | \dot{m}_{max} g/h | $d_{p,\text{mean}}$ μm *** | d_{max} μm | 115/230V 50/60 Hz | Pressure- tight up to 10 bar | Compressed air supply |
|-------------|------------------------|--------------|--------------------|-------------------------------|--|-----------------------------------|----------------------|------------------------------------|--------------------------|
| AGF 2.0 | 300x330x240 | ca. 9 | 6-17 | 4 | 0,25 | 2 | | | x |
| AGF 2.0 iP | 300x330x240 | ca. 15 | 16-18 | 2 | 0,25 | 2 | x | | |
| AGF 10.0 | \emptyset 240x385 | ca. 4 | 12-45 | 20 | 0,5 | 10 | | | x |
| AGF 2.0 D | \emptyset 200x260 | ca. 8 | 12-45 | 4 | 0,25 | 2 | | x | x |
| AGF 10.0 D | \emptyset 200x300 | ca. 8 | 12-45 | 20 | 0,5 | 10 | | x | x |
| AGF 2.0 B** | \emptyset 210x300 | ca. 4 | 6-25 | 4 | 0,25 | 2 | | | x |
| UGF 2000 | 270x200x175 | ca. 4 | ca. 1-13 | 1,5 | 0,2 | 1,5 | | | x |

Figure 4.4: Overview of the AGF systems. * applied for DEHS; ** test rig version; *** average number diameter [67]

reliable data free of statistical errors, it is required to have a relatively high burst signal rate of each channel even at positions very close to the wall, where the velocity is almost zero. The actual LDA burst signal rate varies between 1 Hz and 200 Hz. The particles have been added at least one minute before we start a new measurement to give the flow sufficient time to mix them. The location of particle release is at least 1.1 m away from the measuring position. To guarantee a sufficiently high number of statistically independent measurements, namely with a 95% confidence level, the interval of the data is sufficiently small. Under this circumstance, the experiment time for each position was set to one hour.

4.2 Velocity measurement set-up in the BOI

4.2.1 3D set-up with two LDA probes

The investigation of the flow field at a single point inside the BL requires a simultaneous measurement of all three velocity components. The three-dimensional (3D) velocity field was measured by combining a one-dimensional (1D) LDA probe and a two-dimensional (2D) LDA probe from Dantec Dynamics. The 1D probe is working with a Nd-YAG laser ($\lambda = 532$ nm) and the 2D probe is using an Argon-ion laser ($\lambda = 514.5$ nm, $\lambda = 488$ nm).

The 2D LDA probe was aligned vertically, in order to measure the two horizontal velocity components in x and y direction, see figure 4.5 (a). To apply this probe, one of the windows on the cooling plate

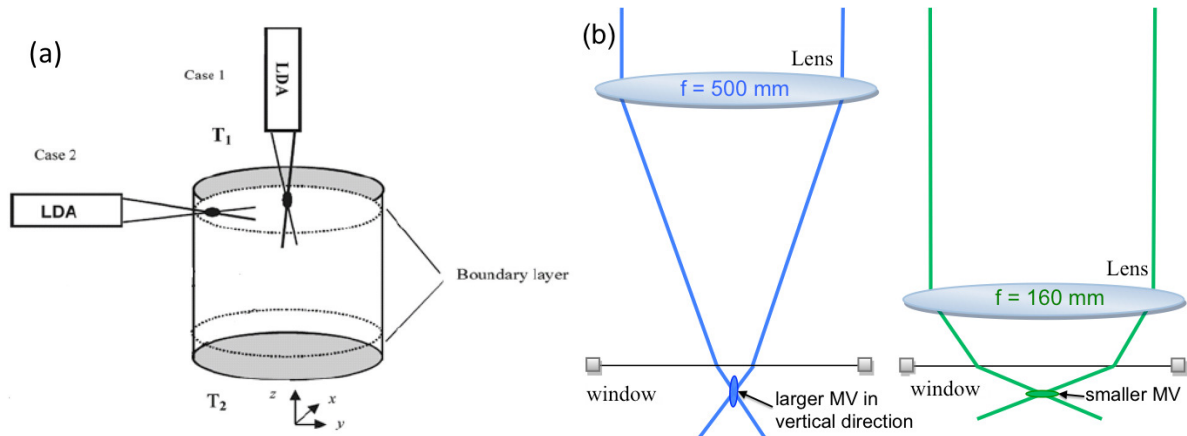


Figure 4.5: Figure (a) shows the theoretical possibilities how one can align the measurement volume. At the BOI, there is no access for guiding the laser through the side-wall. Figure (b) shows the vertical alignment for the BOI with two different front lenses. The optimized measurement volume is guided through the window at the cooling plate with very short focal length of 160 mm.

is used. To measure the wall-normal velocity component usually the 1D probe has to be aligned in the horizontal direction. Because there is in practice no optical access for this alignment, this probe was also placed close to the 2D probe above the window. To resolve the wall-normal velocity, the 1D probe has to be tilted with a certain angle. Finally, both probes were aligned symmetrically with the same angle between the optical axes $\varphi_{1D} = \varphi_{2D}$, see figure 4.6. The size of these angles depend on the focus length of the LDA probes in relation to the diameter of the window. The wall-normal velocity component w is calculated from this angle φ and the weighted difference of the other two components u_2 and u_3 by a transformation matrix (see data post-processing section 4.5). In order to position the measurement volume as close as possible to the cooling plate and to minimize the size of the measurement volume, two different focal length lenses, $f = 160$ mm and $f = 500$ mm, are applied into two depth ranges, sketched in figure 4.5 (b). First, the measurement of the velocity profiles was performed with a focal length of the probes of 160 mm. In this configuration the size of the measurement volume, amounts to $l_{mv_z} = 75$ μm , $d_{mv(x,y)} = 200$ μm . This is 50 times smaller than the typical thickness of the viscous BL in our experiment. The angle between the optical axes of the two LDA probes in this

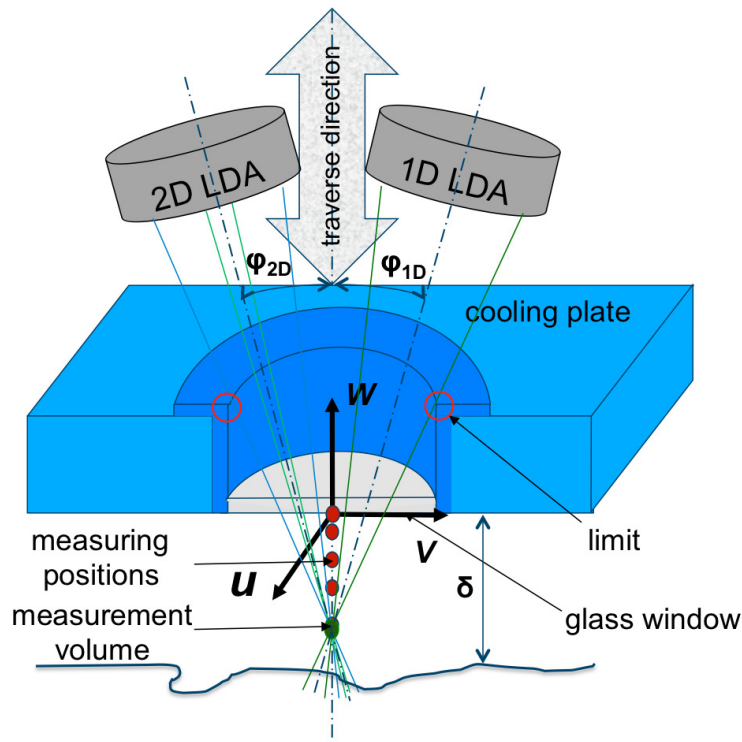


Figure 4.6: Set-up of the 3D laser Doppler anemometry measurement using two probes, which are mounted on the traverse system above the cooling plate. u , v and w are the desired velocity components in the Cartesian coordinate system, δ illustrates the thickness of the BL inside the convection cell.

4 Measurement technique and calibration

configuration was $\varphi_{1D} = \varphi_{2D} = 24.5^\circ$ limited by the window in diameter of 9.5 cm. The measuring depth of the profile (0 mm to 15 mm) is also confined by the diameter of the observation window which is embedded in the cooling plate, shown in figure 4.6. As a consequence, an additional measurement with a longer focal length of 500 mm is necessary to measure the whole profile up to a distance of 180 mm. The angle in this configuration was $\varphi_{1D} = \varphi_{2D} = 6.5^\circ$.

We have also tested the stability of the 3D LDA set-up, shown in figure 4.6. The reason is that the weight of the LDA probes (5 kg each one) and tiny size of the measurement volume can be easily dis-aligned during the automatic traverse matrix motion in the measurement. When the adjustment

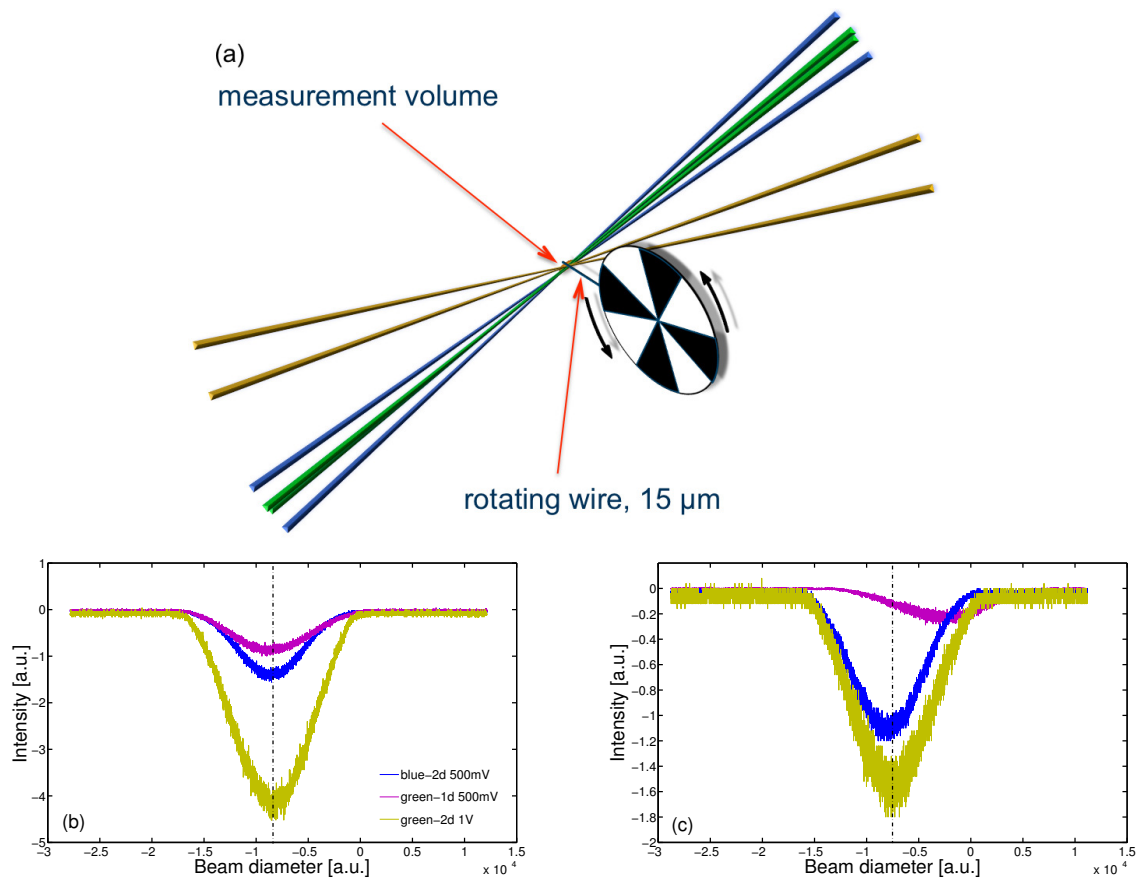


Figure 4.7: Stability test results by the “rotating wire” laser beam diagnostic method. The three colored curves are the three pairs of beams. The peak of the curves denote the maximum intensity of the Gaussian beam intensity distribution. (a) Principle: rotating wire with given frequency is cutting the LDA measurement volume and scanning the intensity distribution of each beam pair. (b) Well aligned measurement volume with all the maximum intensity in one vertical line. (c) De-adjusted measurement volume shows different peak positions after one hour traversing.

of the laser beams is ready, all the three pairs of beams are intersected at one focal point with the maximum intensity of the Gaussian distribution, like the result from the laser beam diagnostic method in Fig. 4.7 (b). In this method, a rotating wire with a given frequency is cutting the laser beam and scanning the intensity distribution, then recorded by a photo-detector. In our case, the detector of the LDA probe was used. As a result, the intensity distribution along the beam diameter can be observed with an oscilloscope. After one hour of traversing, the relative position of the two probes are shifted with respect to each other, which can be seen from the alignment of the measurement volume, shown in Fig. 4.7 (c). The beams are no longer exactly intersected at the focal point. The result indicates that the mounting and positioning devices are not stable enough for a very long time series measurement. For this reason, we changed the devices to a complex of linear stages ($10\ \mu\text{m}$ per scale) and goniometer ($0.1\ \text{deg}$ per scale), which are specialized for mounting and traversing the probes perpendicularly.

4.2.2 Alignment and size of measurement volume

For a precise alignment of all six laser beams in one focal point and for the final measurement of beam waists for the calibration of the size of the LDA measurement volume, a commercial laser beam diagnostic system was performed. The principle of this diagnostic device is based on the recording of the spatial intensity distribution by a CCD camera. Optical filters are used to attenuate the laser beam power. With a BeamView software (Coherent) the parameters (*e.g.* waist diameter) of the laser beam in the focal point can be measured.

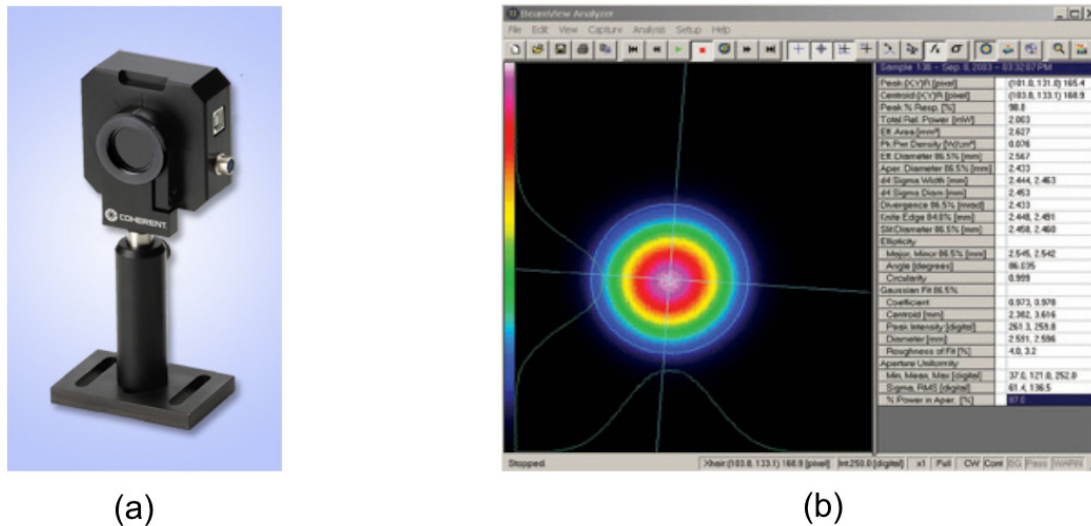


Figure 4.8: (a) Photograph of the laser beam diagnostic system Coherent LaserCam-HR. (b) Example of the intensity distribution of the LDA laser beam in the center of the measurement volume (focal point), screen shot of the BeamView USB Analyzer Software.

In the following section the adjustment procedure of a 3D measurement set-up is described. There are two probes combined in this 3D measurement system, but the adjustment procedures for each of them are the same. The procedure is introduced as follow:

1. Switch on the laser for about 10 minutes until the power of the laser beams becomes stable.
2. Guide the pilot laser beam from the 1D and 2D probe to the beam diagnostic system detector (Coherent LaserCam-HR), see figure 4.8, while traversing the laser probe along its central axis up and down until you find the maximum intensity which is displayed at the screen. The color gradient from red to blue indicates the intensity distribution from high to low. Mark this position by the cursor or read it out from the software of LaserCam-HR.
3. Guide the beams of each single probe intersected at the focal point of the pilot light according to the maximum intensity detected by the LaserCam-HR. This can be achieved by adjusting the prisms embedded in the probe expander.
4. Due to the limited access and space, in the measurements make the crossing angle between the two optical axes as large as possible (the reason has been explained in the 3D set-up section). Finally, guide all the six beams to cross at one point and align the two probes symmetrically. The LaserCam-HR can detect the height difference between the two probes with a resolution of 0.1 mm.
5. Measure the beam waist by the LaserCam-HR. It gives the diameter (d_{mv_x} , d_{mv_y}) of the LDA measurement volume.

4.3 Temperature measurement

For temperature measurements in air, three different sensor types can be applied: thermocouples, resistive temperature devices (RTD) and thermistors. Before starting the comparison, please note that the accuracy and the sensitivity with respect to strong temperature fluctuation are our selection criterion. Each of these sensor technologies caters to specific temperature ranges and environmental conditions. A thermocouple generates a thermoelectric voltage with respect to the temperature difference between the measurement position and a cold junction. With small sensor wires, they would be fast enough for the application in turbulent thermal convection but the output signal of the order of $10 \mu V/K$ is too low to measure the relatively small temperature variations. Accuracy and good linearity are hard to

achieve in precision measurements. Compared with a thermocouple, the RTD probe is much more sensitive. It is working with a Platinum wire, and changing the resistance with respect to the temperature. Compared to thermocouples and thermistors, the RTD sensor has the best precision and stability, but because of its large size, it is only suitable in calibration and process control. In this work, we used it for the calibration of the thermistor probe. Thermistors are temperature dependent semiconductor resistors operating over a range of -100°C to 450°C with a continuous change of resistance over temperature [68]. This resistance change is larger than the RTD. But much more important is the fact that it has a sphere-shaped tip, as small as $125\ \mu\text{m}$ in diameter. A small sensor with low heat capacity allows fast temperature measurements. With a cut-off frequency in the order of 100 Hz, this kind of sensor is predestined for application and turbulent thermal convection. In this work, we choose a NTC (negative temperature coefficient) thermistor, for temperature measurement.

A thermistor is a kind of resistor whose resistance varies significantly with temperature changing. Due to the variation of the current caused by the temperature-dependent resistance, a very low current of $I_{Th} = 5\ \mu\text{A}$ is used in our experiments. The low measurement current is taken in order to prevent measurement errors from the self-heating of the thermistor. The current is supplied by a resistance bridge with an internal DC voltage source. The bridge transforms the resistance change of the thermistor into a voltage and amplifies it by a factor of 100. The output voltage of the bridge is in the range between $-10\ \text{V}$ and $+10\ \text{V}$ and is measured using the computer controlled data acquisition board NI-PCI 6284 from National Instrument (18 bit analog input, correlated (32 clocked lines) DIO 10 MHz, 48 digital I/O lines). The NI-PCI 6284 device and National Instruments LabVIEW interactive software together deliver the measurement data to the computer. It permits a maximum sampling rate of $333\ \text{s}^{-1}$ with a resolution of 6 digits. The thermistor probe is mounted on a traverse system and controlled by a PC with a LabVIEW program. This arrangement permits temperature measurements in air with negligible heating of the sensor, high accuracy and noise immunity as well as with an excellent long-term stability [4]. The thermal dissipation rate of the thermistor is specified with $\varepsilon_D = 0.045\ \text{mW/K}$ in still air.

4.3.1 Set-up and calibration of the micro-thermistor

For all temperature measurements in the convection cell, a glass-encapsulated micro-thermistor with a diameter of approximately $125\ \mu\text{m}$ and $18\ \mu\text{m}$ thick connecting wires was used. It is supported between two pins of a small transistor case and mounted at the end of a brass tube with a diameter of 5 mm, as shown in Figure 4.9. Mounted on a 1D traverse system, it can be moved in steps of $10\ \mu\text{m}$ along the z-axis. The smallest distance to the cooling plate is defined by $z_{min} = 70\ \mu\text{m}$, referring to one half of the

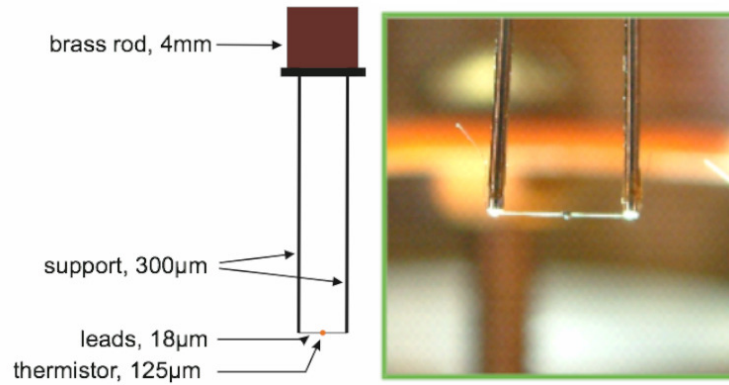


Figure 4.9: Temperature measurement set-up: Schematic of the thermistor probe performed through the central window (Figure 3.1) and a photograph of the sensor tip with connecting wires.

sensor diameter. Due to the strong temperature gradients close to the wall [18], the temperature sensor was aligned with its connecting wires exactly parallel to the cooling plate and along the iso-surface of constant mean temperature in the flow [69]. The temperature sensor has been calibrated in a calibration chamber using a RTD of PT 100 type certified by the Deutsche Kalibrierdienst as reference. The measurement uncertainty of this sensor is specified with ± 0.02 K in the range between 0°C and 100°C .

It should be noted that the typical thickness of the boundary layers is of the order of 10 mm at the Rayleigh numbers covered in this work. The size of the sensor ($125 \mu\text{m}$) is thus 100 times smaller compared with the typical BL thickness and allows a high spatial resolution. All measurements were performed at the corresponding locations where the velocity measurements have been done. The temperature set-up introduction in this chapter is only for the individual velocity and temperature measurements. The simultaneous velocity and temperature experimental set-up is different and will be introduced separately in the next section. Each single measurement covers the distance between $z = 70 \mu\text{m}$ and $z = 150 \text{ mm}$. Each position was measured over a time span of one hour and with a sampling rate of 200 s^{-1} . In order to avoid the systematic errors created, for example, by environmental influences, we automatically ran the measuring position matrix randomly. Before a measurement with new parameters (Ra and ΔT) was started, at least 48 hours relaxation time was necessary to achieve a steady state of the temperature field in the RB cell.

4.4 Simultaneous velocity and temperature measurement set-up

The heat transport in turbulent convection is determined primarily by thermal plumes. The direct measurements of the local convective heat flux in an experiment are essential for a better understanding of

the heat transport mechanism in turbulent convection. The local heat flux is determined by the joint and local velocity and temperature fluctuations. Local velocity measurements are conducted using a 1D Nd-YAG- LDA probe ($\lambda = 532 \text{ nm}$). The heat flux is determined by the wall-normal velocity, therefore, the measurement volume of the LDA probe was aligned horizontally to measure this component directly. Together with the LDA probe a thermistor is mounted on the traverse system, which has been introduced already in the section of temperature measurement, see figure 4.10. In this set-up, the fringe pattern of the LDA measurement volume was parallel to the wall using a small dielectric mirror, which deflects the vertical optical axis of the LDA beams into a horizontal one. Comparing with the 3D LDA measurements, this alignment allows us to measure the wall-normal velocity component directly without error from weighting factors of the velocity transformation matrix, see equation 4.11. Each point of the profile is measured for one hour. In order to keep a constant and high velocity data rate, DEHS

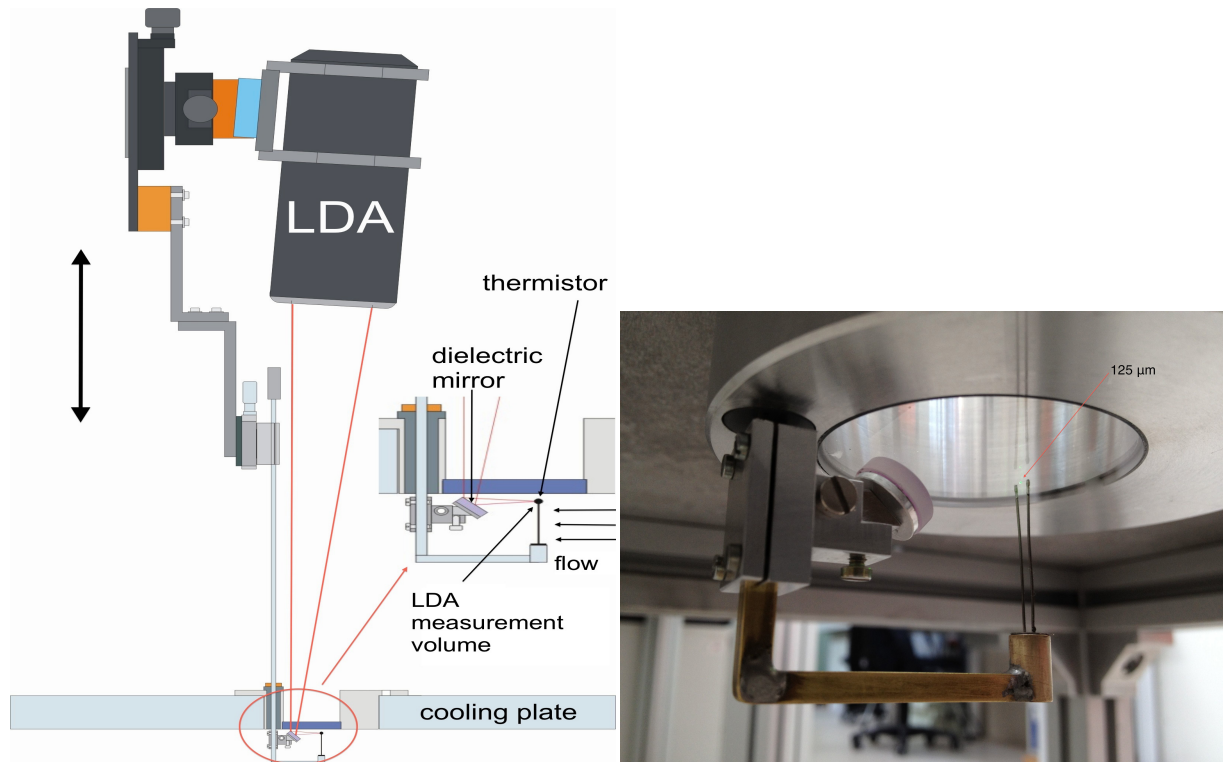


Figure 4.10: Simultaneous velocity and temperature measurement set-up: The sketch on the left shows the set-up of the joint measurement of wall-normal velocity and temperature through one access, a small window embedded in the cooling plate. The alignment of the thermistor and LDA measurement volume was fixed in the direction of the wind. The LDA probe and thermistor support are mounted together on a traverse system, which can be moved up and down precisely in 0.01 mm per step. The figure on the right shows a photograph of the dielectric mirror and the thermistor probe.

seeding particles were injected in regular periods, 5 min per half an hour.

As the name “simultaneous measurement” suggests, the LDA measurement volume and the thermistor should record data at the same time and the same location. This is impossible, since the temperature sensor could be heated up or just burnt by the LDA laser light. Then, theoretically, the thermistor can be placed over, below, in front of, behind or besides the LDA measurement volume as close as possible to each other, but without any interference. For the purpose of a precise LDA measurement volume positioning, the LDA probe is mounted on a goniometer (with 0.1° resolution) together with two linear stages ($10\ \mu\text{m}$ per scale). All these are mounted on the traverse system, so that adjustments are made three-dimensionally. First, we fix the alignment of the laser axis, after reflected by the mirror, being parallel to the cooling plate, which is necessary to ensure measuring the pure wall-normal velocity. In the meanwhile, we set the standard position, where the LDA measurement volume must overlap with the temperature sensor, which can be detected by the voltage changing of the sensor. If they are completely overlapped, then it shows the minimum voltage. Second, the measurement volume can be moved in a vertical direction, over and below the temperature sensor. According to the sketch of the stream lines, in figure 4.11, it can be seen that if one puts them closely together an artificial wall-normal velocity is created due to the deflection at the sensor. To avoid this artificial velocity,

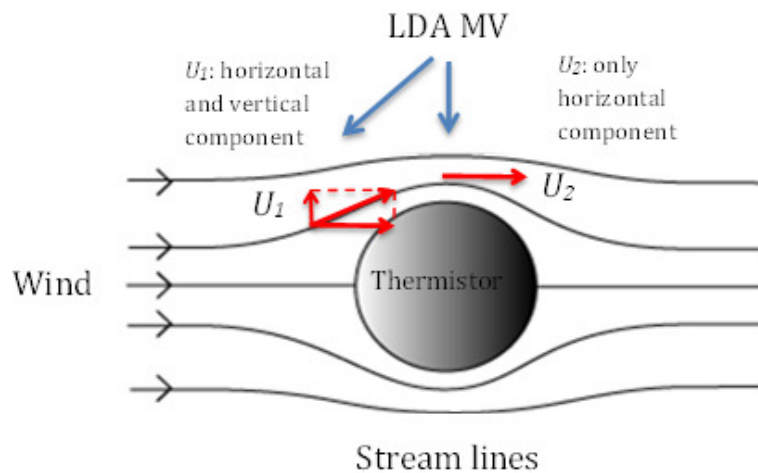


Figure 4.11: Illustration of the flow disturbance from the thermistor

as well as to prevent the heating of the thermistor by the laser light, the LDA measurement volume was placed $55\ \mu\text{m}$ away from the thermistor in a vertical direction and additionally $300\ \mu\text{m}$ away in horizontal direction, see figure 4.12. The optimized spatial separation is much smaller than earlier simultaneous measurements ($700\ \mu\text{m} \pm 200\ \mu\text{m}$)[52, 53], which leads to a stronger cross-correlation

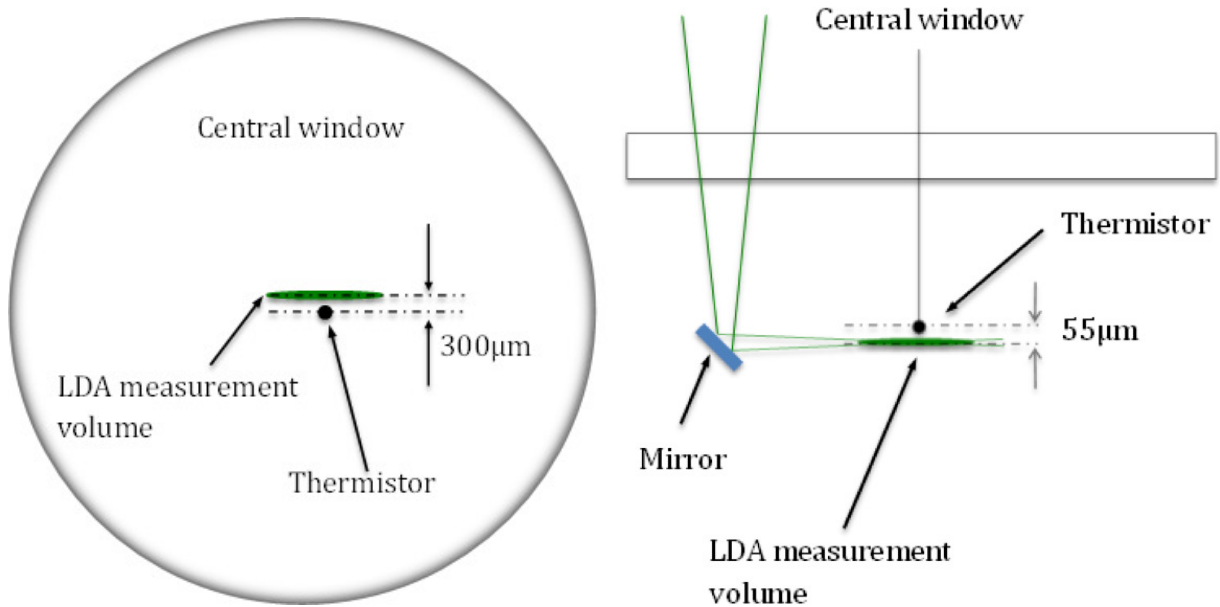


Figure 4.12: On the left side, the top-view of the set-up shows the horizontal displacement of $300 \mu\text{m}$ between the thermistor probe and the LDA measurement volume, which is necessary to minimize the heating of the thermistor by the LDA laser light. On the right side, the front-view shows the additional vertical displacement in order to prevent the measurement of wall-normal velocity from the influence of the flow around the thermistor and the connecting wires.

between velocity and temperature data. The separation of $300 \mu\text{m}$ is in the order of the smallest length scale of the turbulent flow field (Kolmogorov length scale $\approx 1 \text{ mm}$) and will not miss any small structure of the flow. The measurement results show that we have a strong cross-correlation between velocity and temperature time series data at all the positions measured until 160 mm distance from the cooling plate, shown in figure 6.4. The first point of the whole measurement is $z = 2.4 \text{ mm}$, which is limited by the laser alignment and experimental set-up arrangement.

The simultaneous velocity and temperature measurement was performed on two separate computers limited by compatibility problems of the data acquisition software. The consequent problem is the non-synchronized system clock of the two computers. Overall, there are three effects on the time-shift between the velocity and temperature data:

- 1. Computer system clock time difference.
- 2. Measurement starting time difference.
- 3. Distance between LDA measurement volume and temperature sensor.

The first two effects can be solved by calculating the time delay from the velocity and temperature cross-correlation. The data were re-sampled with 1000 Hz, so that the time-shift can be accurate to 10 ms. The third effect, the 300 μm spatial separation between the thermistor and the LDA measurement volume will generate a time-shift of 0.75 ms at a velocity of 0.4 m/s and can be omitted.

4.5 Data post-processing

In figure 4.13, the block diagram shows the procedure of the LDA measurement data acquisition and post-processing. In this chapter, the velocity data post-processing with Matlab program will be introduced. In the first step, the obvious outliers were detected and eliminated. One of the reasons for the outliers is the scattering of the laser light at the glass window. This happens mostly when measurements are conducted in the vicinity of the cooling plate. As the distance to the plate increases the number of outliers decreases significantly. The outliers have to be removed since they may cause statistical errors. A moving average parameter G_i has been calculated for a window of 20 measured values:

$$G_i = \frac{1}{20} \sum_{j=i-10}^{i+9} \bar{x}_j \quad \text{for } i > 10. \quad (4.9)$$

The bounds have been set according to three times the standard deviation of this interval:

$$\sigma_i = \sqrt{\frac{1}{20} \sum_{j=i-10}^{i+9} (x_j - G_i)^2} \quad \text{for } i > 10. \quad (4.10)$$

All samples outside this band have been removed from the time series. It should be noted here that the number of outliers turns out to be only a very small fraction (0.003% on average) of the total number of samples within every time series. Thus, the elimination of these values is justified.

In order to obtain reliable data free of statistical errors it is required to have a relatively high burst signal rate of each channel even at the position where the velocity is almost zero. There are two operating

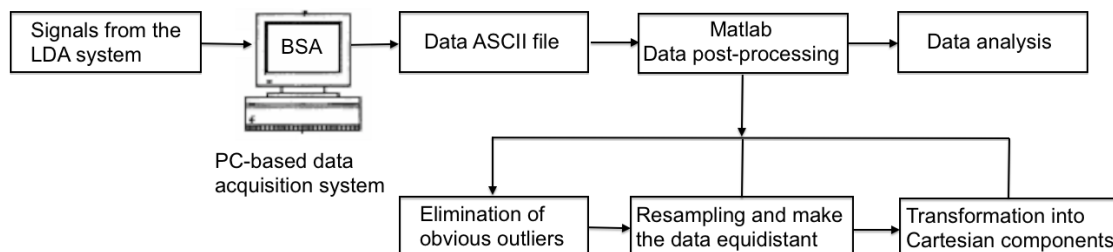


Figure 4.13: LDA block diagram of data acquisition and post-processing procedure.

modes to measure 3D velocity data: the “coincidence” and the “non-coincidence” mode. In the first one, a burst signal rate is only counted if all three LDA channels recognize one sample simultaneously. However, in our set-up, this mode provides very small data rate of the order of 1 s^{-1} . In the second mode, each of the LDA channel operates separately. In this mode the data rate is much higher (up to 200 s^{-1}), but the data are not sampled simultaneously. We have chosen the non-coincidence mode, because of the higher burst signal rate. In order to transfer the randomly measured velocity components u_1 , u_2 and u_3 to the desired velocity components u , v and w in the Cartesian system, we need to make the velocity data equi-distant by interpolation and re-sampling in the second step. We have tested three different sampling rates $f_s = 25, 50$ and 75 Hz and we found that at $f_s = 50 \text{ Hz}$ the Fourier spectrum shows a sufficiently small but well-pronounced plateau. Therefore 50 Hz is the right re-sampling rate for all three velocity components u_1 , u_2 and u_3 . Four different interpolation methods have been investigated: interpolation of the nearest neighbors, linear interpolation, cubic Hermite interpolation and cubic spline interpolation. The first interpolation method was not used further since this method is very crude and the trend between the measured values is ignored. The linear and cubic Hermite interpolation resulted in smoother and closer interpolated curves than the cubic spline interpolation when compared with the original sample. Due to the reasonable computational complexity, the Hermite interpolation was taken, for more details see [70].

In the third step the velocity components u , v and w are calculated according to the following transformation matrix:

$$\begin{pmatrix} u \\ v \\ w \end{pmatrix} = \begin{pmatrix} 1 & 0 & 0 \\ 0 & -\frac{\sin \varphi_2}{\sin(\varphi_1 - \varphi_2)} & \frac{\sin \varphi_1}{\sin(\varphi_1 - \varphi_2)} \\ 0 & \frac{\cos \varphi_2}{\cos(\varphi_1 - \varphi_2)} & -\frac{\cos \varphi_1}{\cos(\varphi_1 - \varphi_2)} \end{pmatrix} \begin{pmatrix} u_1 \\ u_2 \\ u_3 \end{pmatrix} \quad (4.11)$$

This angular transformation matrix is used in correspondence with the software user guide manual of the LDA equipment [71]. In the measurement, the three random components “ u_1 , u_2 and u_3 ” were measured, then the desired components “ u , v and w ” in the Cartesian system were corrected by this matrix. In Fig. 4.6, the measurement set-up and the coordinate system are shown. With this set-up, one of the horizontal velocity components, u_1 is measured directly.

Due to the arbitrary and fluctuating orientation of the LSC in the cylindrical RB cell (see e.g. Resagk et al. [15]), we studied the magnitude of the horizontal velocity:

$$U = \sqrt{u^2 + v^2}, \quad (4.12)$$

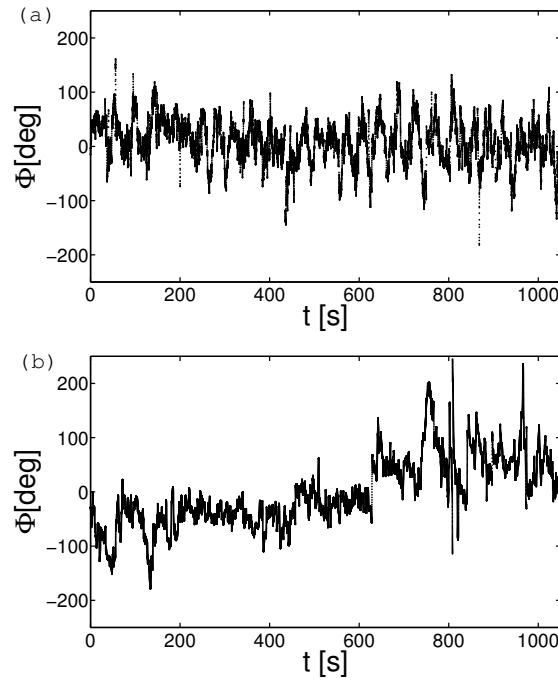


Figure 4.14: Orientation of the horizontal velocity vector. (a) Instantaneous angle of the vector from experiment and (b) DNS data [1], taken at the center line. The time axis from the DNS has been recalculated to the experimental ones. Figure is taken from Ref. [20].

instead of one of the single velocity components, u or v . In Fig. 4.14 the time series of the instantaneous angle of the horizontal velocity vector at the center line are plotted. While the orientation of the velocity vector (and thus that of the LSC) seems to be locked in the experiment due to small imperfections of the RB cell (see Fig. 4.14a), the oscillation of the angle drifts slowly in the DNS (see Fig. 4.14b).

The simultaneous measurements were conducted on two individual computers and the time-shift existed between the velocity and temperature time series data, introduced in the last section. We introduce the data post-processing of the simultaneous measurements in the following steps:

1. Filter the velocity data using the same method as handling the 3D velocity data.
2. In order to calculate the time-shift between the velocity and temperature measurement computers, the cross-correlation function must be calculated, therefore the velocity and temperature data have to be re-sampled by the linear function. The sampling frequency is 1000 Hz., thus we can have a time-shift as precise as about $10 \mu\text{s}$, calculated by the cross-correlation function. Please note that the second step for re-sampling the data is only for calculating the cross-correlation function. The re-sampled data will not be brought into the next step, only the filtered data will.

3. The filtered velocity time series data have been shifted by the time-shift calculated from the cross-correlation.
4. In order to calculate the term $\langle w' \cdot T' \rangle_t$ of the convective heat flux, the temperature time series data are re-sampled according to the velocity time series data. In this way, we can keep the resolution (on average 50 Hz) of the velocity data, but interpolate the temperature data which has a much higher data resolution (200 Hz).

CHAPTER 5

RESULTS: VELOCITY AND TEMPERATURE PROFILES FROM THE SMALL CONVECTION CELL

5.1 Velocity and temperature profiles at aspect ratio $\Gamma = 1$

The knowledge of the local velocity and temperature field variables, in particular within the BLs is still very poor. However, a better understanding of the mechanisms of global turbulent heat transport at large Rayleigh numbers remains thus intimately connected with a better understanding of the physics inside the BLs. However, such an endeavor is only possible to a limited extent due to the need for a theoretical interpretation of experimental results and the quantitative prediction of this type of flow. The local velocity and temperature measurements in highly turbulent RB convection would definitely help us to alleviate some of this knowledge deficit. To that end, we present a joint experimental and numerical analysis. In particular, we make a direct comparison of the structure of BL of the velocity and temperature fields in a cylindrical RB cell filled with air at two Rayleigh numbers $Ra > 10^9$ and at aspect ratio $\Gamma = 1$ at various positions.

5.1.1 Velocity profiles at the center line

We present first the mean velocity profiles at $Ra = 3 \times 10^9$ and $Ra = 3 \times 10^{10}$ and start with the comparison of the mean horizontal velocity profiles at the center line, $\langle U(z) \rangle$, as shown in Fig. 5.1. The symbol $\langle \cdot \rangle$ stands for an average over the time series taken in the studies and horizontal velocity U is defined by equation (4.12). The experimental mean velocity profiles at $Ra = 3 \times 10^9$ and $Ra = 3 \times 10^{10}$ are plotted as closed circles, the corresponding DNS results [1] as open circles. They are normalized by the maximum mean velocity. Additionally, the Prandtl-Blasius prediction of the two-dimensional BL equations [47] is plotted. The data show that the measured and numerical mean velocity profiles agree

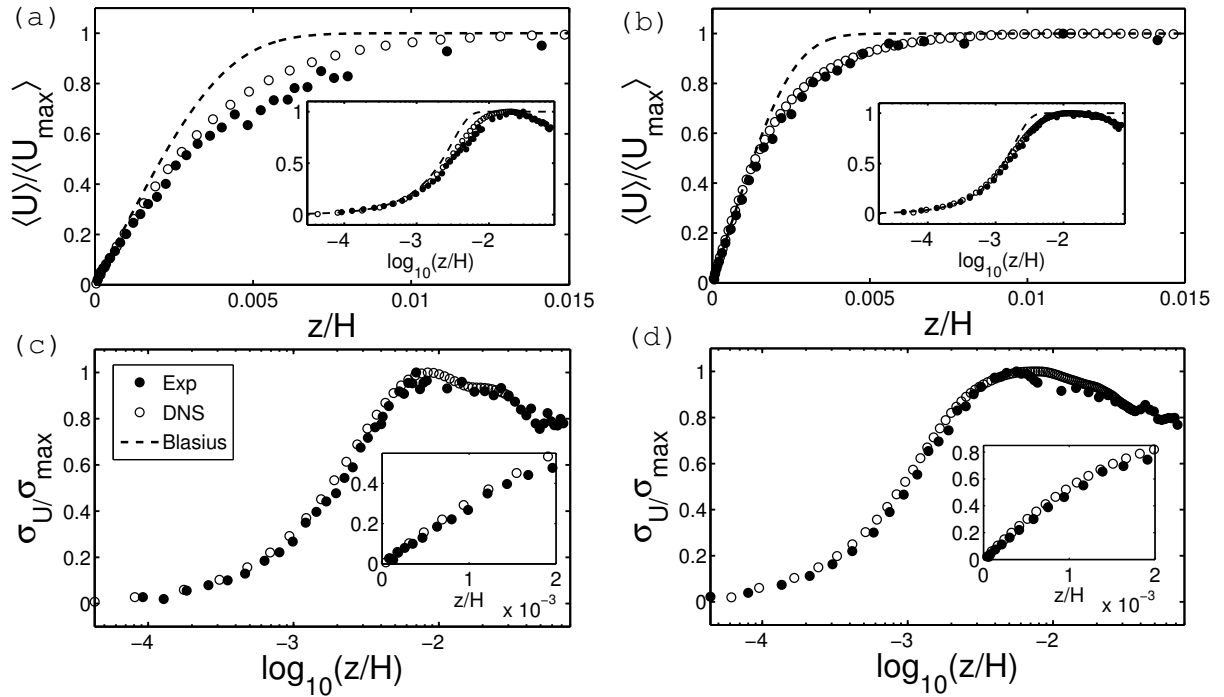


Figure 5.1: Profiles of the mean horizontal velocity (a,b) and the standard deviation (c,d) measured in the experiment (closed circles) and obtained from the DNS (open circles) [1] at $Ra = 3 \times 10^9$ (a,c) and $Ra = 3 \times 10^{10}$ (b,d). The dashed lines in (a) and (b) represent the velocity field of a laminar flat plate BL according to Blasius [47]. The insets of (a) and (b) show the entire mean velocity profile in logarithmic scale and the inset of (c) and (d) show the near-wall region of the BL fluctuations.

well for both Rayleigh numbers. In case of $Ra = 3 \times 10^9$, both mean velocity profiles show a linearly increasing fraction of the profile. The maximum difference of both curves amount to 9 % at a height that corresponds with the BL thickness.

Additionally, we can address the question whether the profiles of the mean velocity of turbulent RB convection match with the laminar Blasius prediction [47]. The detailed Blasius solution has been introduced in chapter 2. The 99% level of the free stream velocity is defined as BL. Then the self-similar variable is equal to $\eta_{PB} = 4.92$ and the BL thickness is given as $\delta = 4.92 \sqrt{(vx / \langle U_{max} \rangle)}$. The values of the Blasius function and its first two derivatives can be found in the ready solved table [72]. The Blasius prediction describes a steady two-dimensional BL that forms on a semi-infinite plate. It is held parallel to a constant unidirectional flow and is usually recommended to be compared to RB velocity profile in the BL. Some theories for the prediction of turbulent heat transport in the RB convection are based on the Blasius solution, for example the GL theory [31, 32, 46]. Therefore, it is very important

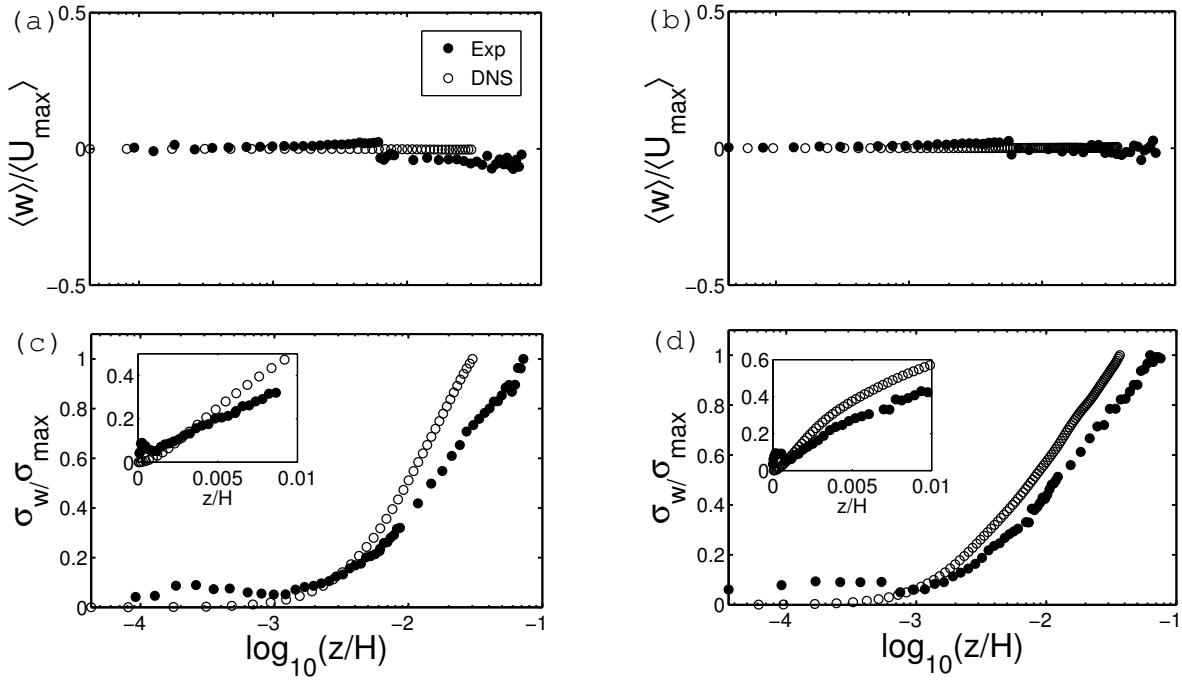


Figure 5.2: Profiles of the mean wall-normal velocity (a,b) and the standard deviation (c,d) measured in the experiment (closed circles) and obtained from the DNS (open circles) [1] at $Ra = 3 \times 10^9$ (a,c) and $Ra = 3 \times 10^{10}$ (b,d). The insets show the near-wall region of the BL.

to verify if the prediction is feasible or not. It has been already found in a previous study by du Puits et al. [19] that the Blasius profile does not provide a good approximation to the measured profiles of the mean horizontal velocity in turbulent RB convection. These measurements covered a range of Rayleigh numbers of one order of magnitude between $Ra = 10^{11}$ and $Ra = 10^{12}$. In the present work we extend this range and show results at lower Rayleigh numbers of $Ra = 3 \times 10^9$ and $Ra = 3 \times 10^{10}$. In both cases, the near-wall part of the profiles grows almost linearly and coincides with the Blasius solution as visible in the inset of Fig. 5.1 (a), (b). Following their shape towards larger distances, the profiles noticeably start to deviate from the theoretical prediction of the laminar shear layer, especially for the velocity at the lower Ra . We can thus conclude that the Blasius profile cannot perfectly describe the profiles of the mean velocity in turbulent RB convection for the range of Rayleigh numbers which are accessible to the measurements and simulations. The velocity and temperature field coupled BL in RB convection is not a purely laminar BL and is different from the BL in forced convection.

For a further analysis of the existing difference between the measured mean velocity profile and Blasius solution, a dynamic rescaling method has been suggested in [48] and has been discussed in [1] for the DNS. The method of dynamic rescaling of the data is used to normalize the mean velocity or

temperature profile by an instantaneous BL thickness, which tends to bring the mean profiles closer to the Blasius prediction in the water experiment by Zhou and Xia [48]. It cannot be performed in the current measurements since the time series of the profiles are taken point by point. In summary, all the horizontal velocity profiles are systematically smaller than Blasius prediction, within the investigated Rayleigh numbers between $Ra = 10^9$ and $Ra = 10^{12}$. A reason might be the extraction of kinetic energy from the horizontal motion in order to supply the wall-normal disturbances.

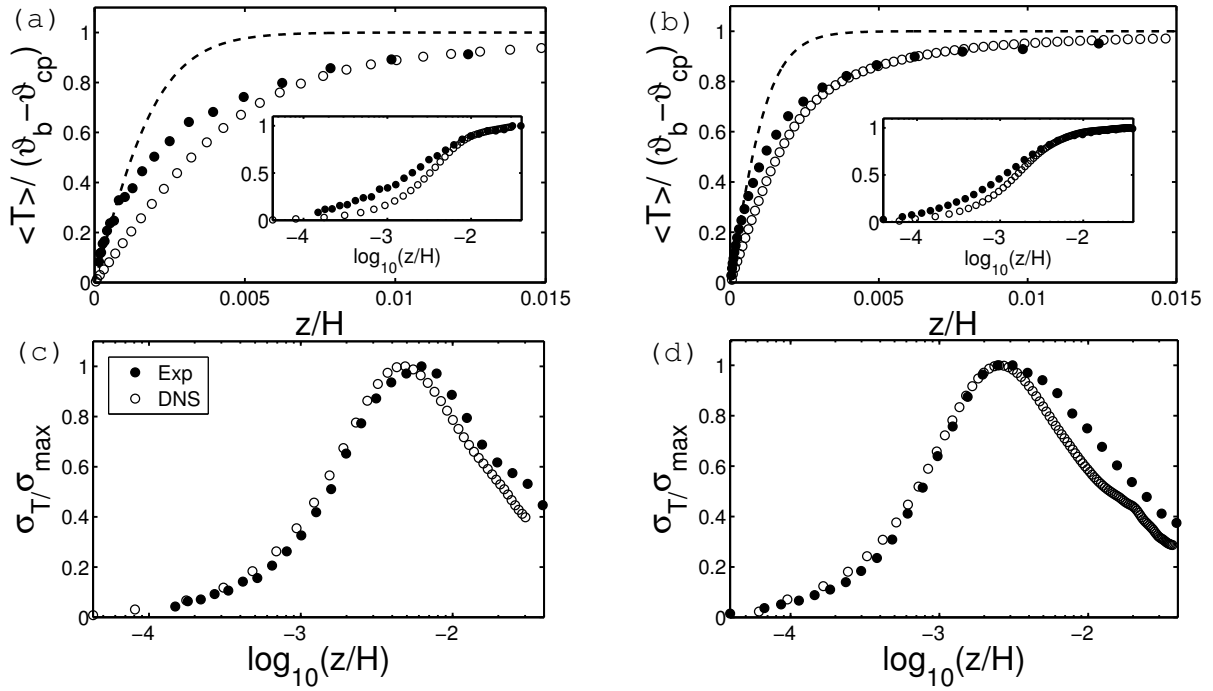
The standard deviation (or root-mean-square) of the horizontal velocity $\sigma_U(z)$ is shown in Fig. 5.1 (c) and (d). The profiles are normalized by their maximum values (0.032 m/s, 0.083 m/s, respectively). Both of the measured profiles are linear increasing near the wall until they reach a maximum, then beyond the maximum σ_{max} decrease. The comparison of the data at $Ra = 3 \times 10^9$ and $Ra = 3 \times 10^{10}$ indicates a very good agreement except for a sudden drop (see [18] for a detailed discussion) in the measured profile at $Ra = 3 \times 10^{10}$. The local maximum of the profile for both cases is at about the same distance from the wall, although the BL gets thinner with higher Ra. Again the agreement seems to improve slightly for the larger Rayleigh numbers.

The measured mean profiles of the wall-normal velocity component $\langle w(z) \rangle$ at $Ra = 3 \times 10^9$ and $Ra = 3 \times 10^{10}$ are plotted in Fig. 5.2 (a) and (b). For both Rayleigh numbers the mean wall-normal velocities tend to zero, in other words, there is no mean vertical velocity. The good agreement between the measured data and the DNS data proves this conclusion. Our result is in agreement with the PIV measurements by Sun et al. [43]. However, this is in contrast to the classical Blasius solutions for an incompressible fluid which obeys a vertical velocity profile due to the displacement effect of the BL. The “jump” of the data is caused by switching from the short to the long focal length lens of the LDA. Due to the specific arrangement of the LDA probes the wall-normal velocity component is extremely sensitive to small misalignments. The change in the lenses requires a complete readjustment of the probes and the result shown in the plot is actually the best one that we can achieve with the given set-up. Nevertheless, the profiles show a clear trend of a zero mean wall-normal velocity which is consistent with a three-dimensional flow structure in an incompressible flow setting. As we can also see, the wall-normal standard deviations $\sigma_w(z)$ are not zero right above the wall. This can be seen from the data compared in Fig. 5.2 (c) and (d). The velocity fluctuations keep increasing to magnitudes that are comparable to the horizontal component. The “bump” of the experimental data at $z/h < 10^{-3}$ is the error caused by the scattering light reflected from the glass window surface. This problem is inevitable for all LDA measurements very close to an interface. The profiles of the standard deviation

of the vertical component in experiment and DNS fit well to being zero at both Rayleigh numbers in the region $0 < z/H < 10^{-3}$, i.e. well within BL. For $z/H > 10^{-3}$ the rms value $\sigma_w(z)$ is strongly increasing. For completeness, the measured viscous BL thicknesses are $\delta_{v,d}/H = 3.8 \times 10^{-3}$ for $Ra = 3 \times 10^9$ and $\delta_{v,d}/H = 1.7 \times 10^{-3}$ for $Ra = 3 \times 10^{10}$. This implies that the fluctuations of the vertical velocity component start to increase rapidly at the edge of the BL. The viscous BL thickness $\delta_{v,d}$ is here calculated by the displacement method, which will be discussed later in the text.

5.1.2 Temperature profiles at the center line

Having discussed the mean profiles of the velocity components so far, we now turn to the mean temperature profiles $\langle T(z) \rangle$ which are displayed in Figs. 5.3 (a) and (b). The mean temperature profiles, measured at $Ra = 3 \times 10^9$ and $Ra = 3 \times 10^{10}$ at the center line, are normalized by the temperature difference as measured between the bulk and the cooling plate. The agreement between the measurement and the numerical data is not as perfect as for the velocity data but is still satisfactory. However, a



[h]

Figure 5.3: Profiles of the mean temperature (a,b) and the standard deviation (c,d) measured in the experiment (closed circles) [14] and obtained from the DNS (open circles) [1] at $Ra = 3 \times 10^9$ (a,c) and $Ra = 3 \times 10^{10}$ (b,d). The Pohlhausen solution is plotted on top of the mean temperature profile. The insets show the near-wall region of the BL. Here, ϑ_b and ϑ_{cp} denote the mean bulk temperature and the surface temperature of the cooling plate.

very detailed view close to the plate surface shows that the measured mean temperature gradients at the wall $d\langle T(z) \rangle / dz|_{z=0}$ strongly differ from the DNS data. It exceeds the value from the DNS by a factor of 2.5 at $Ra = 3 \times 10^9$ and by a factor of 1.5 at $Ra = 3 \times 10^{10}$. In other words, the local heat flux in the experiment is 2.5 (1.5) times larger than numerical result. Currently, we do not have a conclusive explanation for this difference. One reason might be as follows: we found in the early temperature measurement that the fluid properties can be varying, *e.g.* the heat conductivity λ_{th} varying by about 15% across the cell at temperature difference $\Delta T = 45$ K [14]. In the current work, the temperature difference amounts to $\Delta T = 20$ K at $Ra = 3 \times 10^{10}$, which means that the heat conductivity λ_{th} varies by about 7.5%. According to Fourier's law of heat conduction, the temperature gradient is equal to $dT/dz|_{z=0} = -q_w/\lambda_{th}$ and the variation of λ_{th} causes a change of the temperature gradients at the surface of the cooling plates or heating plate by 7.5% as well. Thermal diffusivity κ and kinematic viscosity ν vary even by 15%, but the numerical simulation based on Boussinesq approximation does not take this into account. Finally, we want to state here, that measurements and DNS have been performed with the highest possible diligence and the results are verified in multiple ways. We are also aware about this difference to other RB convection measurements [9, 39] and other very recent DNS results [48, 51]. However, we believe that our measurements are well verified for the following reasons [69]:

- Each sensor has passed a complex calibration process resulting in an accuracy of better than ± 10 mK.
- In addition to the profile measurement with the micro-thermistor the cooling plate temperature at the cell center and the temperature in the bulk have been measured with two independent temperature probes. The measured values coincide very well.
- The size of the sensor is very small compared to the typical BL thickness and amounts only to about 1/100 of the one.
- The plate surface within a radius of 0.5 m around the measurement position is smooth. The roughness amounts to less than $5 \mu\text{m}$ corresponding 0.05 % of the minimal BL thickness.

We have also investigated if the Pohlhausen prediction [73] for the temperature profile fits with our results. The Pohlhausen solution builds on the Blasius solution for the laminar BL and assumes that the temperature is passively advected in the flow. We found that both, the experimental and numerical mean profiles, deviate from this prediction. In Ref. [1] it is demonstrated that one reason for these deviations are the permanent detachments of fragments of the thermal BL into the bulk, the so-called thermal plumes. The standard deviation of the temperature $\sigma_T(z)$ is plotted Figs. 5.3 (c) and (d). They

are normalized by the maximum amplitude. It can be seen that they have the same trend in both panels. At $Ra = 3 \times 10^9$, the temperature fluctuations from experiment and DNS have 10 – 20 % difference from each other before approaching their maximum. For larger distances away from the wall the difference gets smaller to about 5 %. At $Ra = 3 \times 10^{10}$, the fluctuations agree quite well, especially up to the maximum fluctuation. For larger z , we find a difference by about 10 % in comparison to the DNS.

In summary, at two Rayleigh numbers, $Ra = 3 \times 10^9$ and $Ra = 3 \times 10^{10}$, highly resolved measurements of all three velocity components and the temperature inside and outside the BL have been carried out. The measured velocity data agree very well with the DNS results while the temperature data slightly differ. The mean horizontal velocity as well as the mean of the wall-normal velocity are in an excellent agreement. Both differ from the Blasius solution of a laminar non-isothermal shear layer.

5.1.3 Boundary layer scaling

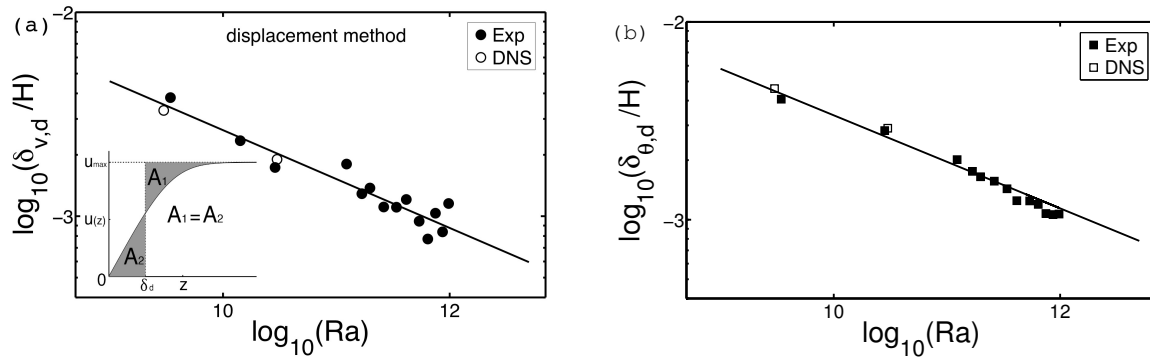


Figure 5.4: Displacement thickness of the viscous (a) and the thermal (b) BLs versus Ra . Experimental results (including earlier measurements data, see in table 5.1 and 5.2) are displayed as closed symbols, DNS data points are open symbols [1]. The solid lines in each of the graphs correspond to power laws $\delta_{v,d}/H = 0.66 Ra^{-0.24}$ and $\delta_{\theta,d}/H = 0.76 Ra^{-0.24}$, respectively. The inset in the left diagram shows the principle of displacement thickness definition.

The boundary layer plays an essential role in studying thermal convection. The thermal plumes in RB convection rise up from the BL of the heating plate, arrive at BL of the cooling plate, then go through the BL and fall down at the other side. The whole self-organized circulation in the RB convection is triggered and maintained by the BL. The scaling theories of thermal convection aim at predicting transport laws for the heat. In this chapter, we turn to the scaling analysis of the local BL thickness with respect to the Ra . Generally, there are two methods to calculate the BL thickness, so called “slope

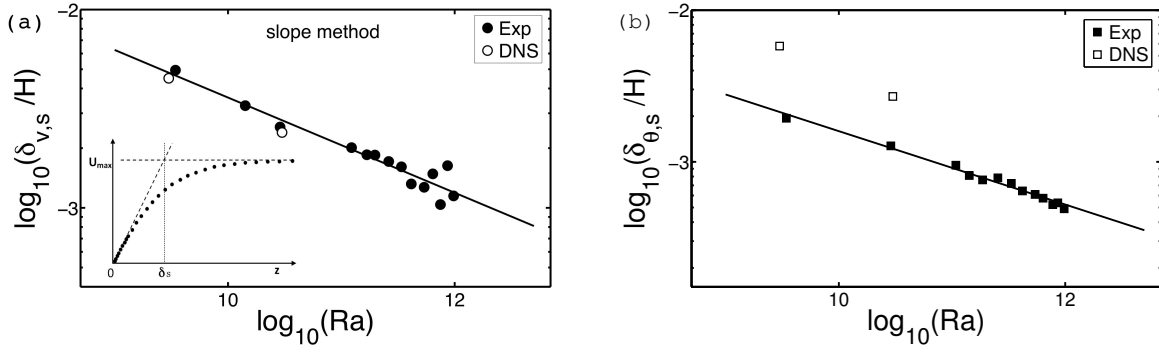


Figure 5.5: Thickness of the viscous (a) and the thermal (b) BLs versus Ra according to the slope method. Experimental results (including earlier measurements data, see in table 5.1 and 5.2) are displayed as closed symbols, DNS data points are open symbols [1]. The solid lines in each of the graphs correspond to power laws $\delta_{v,s}/H = 0.90 \text{ Ra}^{-0.24}$ and $\delta_{\theta,s}/H = 0.42 \text{ Ra}^{-0.24}$, respectively. The inset in the left diagram shows the principle of slope method.

method” and “displacement method”. The principles of both methods are sketched in the insets of Fig. 5.4 (a) and Fig. 5.5 (a). The slope method is more widely used in RB convection and it is useful to complement the analysis of the BL scaling by the slope method (see Tilgner’s paper “Temperature and velocity profiles in turbulent convection in water” in 1993 [38]) for the computation of the BL thickness. The slope method is based on the near-wall gradient of the velocity and the temperature profile. First, we extrapolate the linear part of the velocity profile, then we get the viscous BL thickness from the intersection of the extrapolation and the horizontal line through the first local maximum of the mean velocity. For the thermal BL thickness, we fit the mean temperature profile in the range of $0 < z < 2.07 \text{ mm}$ by the function $y = ax^2 + bx + c$, then compute the thermal BL thickness by the gradient, namely $\delta_{\theta,s} = 1/b$. The displacement thickness is one of the possible measures of the BL thickness. It is defined as the distance by which the surface has to be displaced to compensate the reduction in flow rate due to the effect of the BL. We compute the integrals of the mean horizontal velocity U and the temperature T profiles numerically by a trapezoidal rule, according to the following definitions [74]:

$$\delta_{v,d} = \int_0^\infty \left[1 - \frac{\langle U(z) \rangle}{\langle U_{max} \rangle} \right] dz \quad (5.1)$$

$$\delta_{\theta,d} = \int_0^\infty \left[1 - \frac{\langle T(z) \rangle - \vartheta_{cp}}{\langle \vartheta_b - \vartheta_{cp} \rangle} \right] dz. \quad (5.2)$$

where ϑ_b and ϑ_{cp} are the mean temperature in the bulk and the fixed temperature at the surface of the cooling plate, respectively. Although the slope method is very popular in the RB community, the results are more uncertain than for the displacement thickness. They are very sensitive to the smoothness of the first several data points and depend on the number of data points taken into account. In this chapter,

| Ra | $\langle U_{max} \rangle$ | Re_s | Re_g | $\delta_{v,d}$ | $\delta_{v,d}/H$ |
|-------------------------|---------------------------|--------|--------------------|----------------|------------------|
| | (m/s) | | | (mm) | |
| * 3.44×10^9 | 0.097 | 68 | 1.49×10^4 | 9.532 | 0.00381 |
| * 1.42×10^{10} | 0.168 | 79 | 2.57×10^4 | 5.863 | 0.00235 |
| * 2.88×10^{10} | 0.224 | 99 | 3.41×10^4 | 4.335 | 0.00173 |
| 1.23×10^{11} | 0.179 | 133 | 7.36×10^4 | 11.35 | 0.00180 |
| 1.68×10^{11} | 0.212 | 112 | 8.71×10^4 | 8.12 | 0.00129 |
| 1.98×10^{11} | 0.220 | 124 | 9.00×10^4 | 8.66 | 0.00137 |
| 2.62×10^{11} | 0.262 | 118 | 1.06×10^5 | 6.99 | 0.00111 |
| 3.39×10^{11} | 0.301 | 134 | 1.21×10^5 | 6.97 | 0.00111 |
| 4.14×10^{11} | 0.339 | 162 | 1.34×10^5 | 7.61 | 0.00121 |
| 5.38×10^{11} | 0.404 | 149 | 1.57×10^5 | 5.95 | 0.00094 |
| 6.40×10^{11} | 0.435 | 129 | 1.67×10^5 | 4.87 | 0.00078 |
| 7.48×10^{11} | 0.503 | 195 | 1.89×10^5 | 6.52 | 0.00103 |
| 8.64×10^{11} | 0.545 | 167 | 2.00×10^5 | 5.28 | 0.00084 |
| 9.77×10^{11} | 0.607 | 251 | 2.17×10^5 | 7.27 | 0.00115 |

Table 5.1: Set of parameters and selected results of the velocity measurements at $\Gamma = 1$, $Pr = 0.7$ and Ra between 3.44×10^9 and 9.77×10^{11} . $\langle U_{max} \rangle$ denotes the maximum of the mean horizontal velocity, Re_s denotes the shear Reynolds number, Re_g denotes the global Reynolds number, $\delta_{v,d}$ and dimensionless $\delta_{v,d}/H$ are the displacement thicknesses for the viscous BL. The first three Rayleigh numbers (with star) are from the current measurements, measured in the small convection cell with 2.5 m height and 2.5 m diameter. The others are from earlier measurements [19] in the large convection cell with 6.3 m height and 7.14 m diameter.

we compute the viscous and thermal BL thickness by both methods.

In Fig. 5.4 we summarize the obtained BL thickness values at the corresponding Rayleigh numbers in a range between $Ra = 10^9$ to 10^{12} using the displacement method. The data points at $Ra = 3 \times 10^9$ and $Ra = 3 \times 10^{10}$ are from the present work the data points at the higher Ra numbers are from previous investigations [19, 4]. The plots are given in double logarithmic axes such that a possible algebraic scaling becomes right away visible. The viscous and thermal BL thicknesses are normalized by the constant height of the cylindrical cell $H = 2.55$ m and for the earlier data by the height of $H = 6.3$ m.

| Ra | Re _g | δ _{θ,d} (mm) | δ _{θ,d} /H |
|--------------------------|------------------------|--------------------------|---------------------|
| *3.44 × 10 ⁹ | 1.49 × 10 ⁴ | 10.391 | 0.00416 |
| *2.88 × 10 ¹⁰ | 3.41 × 10 ⁴ | 7.211 | 0.00288 |
| 1.08 × 10 ¹¹ | 6.73 × 10 ⁴ | 12.678 | 0.00201 |
| 1.42 × 10 ¹¹ | 7.77 × 10 ⁴ | 11.063 | 0.00176 |
| 1.86 × 10 ¹¹ | 8.95 × 10 ⁴ | 10.391 | 0.00165 |
| 2.54 × 10 ¹¹ | 1.05 × 10 ⁵ | 9.875 | 0.00157 |
| 3.34 × 10 ¹¹ | 1.22 × 10 ⁵ | 9.034 | 0.00143 |
| 4.19 × 10 ¹¹ | 1.37 × 10 ⁵ | 7.857 | 0.00125 |
| 5.42 × 10 ¹¹ | 1.57 × 10 ⁵ | 7.844 | 0.00125 |
| 6.37 × 10 ¹¹ | 1.71 × 10 ⁵ | 7.532 | 0.00120 |
| 7.76 × 10 ¹¹ | 1.90 × 10 ⁵ | 6.775 | 0.00108 |
| 8.59 × 10 ¹¹ | 2.00 × 10 ⁵ | 6.955 | 0.00110 |
| 9.78 × 10 ¹¹ | 2.14 × 10 ⁵ | 6.734 | 0.00107 |

Table 5.2: Set of parameters and selected results of the temperature measurements at $\Gamma = 1$, $\text{Pr} = 0.7$ and Ra between 3.44×10^9 and 9.78×10^{11} . Re_g is the global Reynolds number, δ_{θ,d} and dimensionless δ_{θ,d}/H are the displacement thicknesses for the thermal BL. The first two Ra numbers (with star) are from the current measurements, measured in the small convection cell with 2.5 m height and 2.5 m diameter. The others are from the earlier measurements [4], measured in the big convection cell with 6.3 m height and 7.14 m diameter.

The measured values of both BL thicknesses, viscous and thermal one, agree perfectly with the data from the DNS. Adding the experimental data from the previous work both quantities scale with Ra as well as with Re_g according to power laws $\delta_{v,d}/H = C_{1,d} \text{Ra}^\beta$, $\delta_{\theta,d}/H = C_{2,d} \text{Ra}^\gamma$, $\delta_{v,d}/H = C_3 \text{Re}_g^\epsilon$ and $\delta_{\theta,d}/H = C_4 \text{Re}_g^\eta$. The pre-factors and the exponents have been computed as $C_{1,d} = 0.66 \pm 0.51$, $C_{2,d} = 0.76 \pm 0.33$, $C_3 = 0.64 \pm 0.66$, $C_4 = 0.54 \pm 0.13$, $\beta = -0.24 \pm 0.03$, $\gamma = -0.24 \pm 0.02$, $\epsilon = -0.54 \pm 0.09$ and $\eta = -0.51 \pm 0.02$. Before we make the comparison, a preview of thermal and viscous BL profiles are collected in the table 5.3.

The obtained exponent β in the current work is quite different from one of previous experiments, for

| Group | Type | Range of Ra | Pr | β | γ |
|-------------------------------------|---------------------------|------------------|----------|------------------|------------------|
| Experiments | | | | | |
| Current work (2012) | δ_v, δ_θ | $10^9 - 10^{12}$ | 0.7 | -0.24 ± 0.03 | -0.24 ± 0.02 |
| | | | | -0.24 ± 0.03 | -0.24 ± 0.01 |
| du Puits <i>et al.</i> (2007, 2009) | δ_θ | $10^9 - 10^{12}$ | 0.7 | \times | -0.2540 |
| Xin <i>et al.</i> (1996) | δ_v, δ_θ | $10^8 - 10^{10}$ | 7 | -0.16 ± 0.02 | -0.29 |
| Numerical simulations | | | | | |
| Scheel <i>et al.</i> (2012) | δ_v, δ_θ | $10^5 - 10^9$ | 0.7, 0.4 | -0.18 ± 0.01 | -0.25 ± 0.01 |

Table 5.3: Preview of boundary layer power law scaling results from both experiments and numerical simulations. β denotes the exponent of viscous BL (δ_v) scaling; γ denotes the exponent of thermal BL (δ_θ) scaling.

example $\beta = -0.16$, made in water [7]. However, the BL thickness in the water experiment is only about 1 mm thick and thus poses much higher requirements on the resolution. However comparing with the numerical simulations calculated at $\text{Pr} = 0.7$, the exponent of δ_θ is similar with each other. We conclude that the discrepancy is mostly due to different aspect ratios and Prandtl numbers. It should also be noted that our scaling laws describe the behavior of the local BL thickness at the central axis of the cylindrical cell and must not necessarily agree with the prediction of the global scaling. Nevertheless, β perfectly fits the prediction of the global exponent (0.25) according to the phenomenological scaling theory of Grossmann and Lohse [31]. The exponent γ is slightly lower than expected from the global scaling $\text{Nu} \sim \text{Ra}^{\gamma'}$ and the exponent ϵ is slightly higher than from $\delta_v = 0.25L \text{Re}^{-0.5}$. Moreover it should be mentioned that both, viscous and the thermal BLs exhibit approximately the same thickness which is consistent with a Pr of about unity.

In figure 5.5, we present the BL thickness calculated by the slope method, which we have introduced at the beginning of this chapter. According to power laws $\delta_{v,s}/H = C_{1,s} \text{Ra}^{\beta'}$, $\delta_{\theta,s}/H = C_{2,s} \text{Ra}^{\gamma'}$, the pre-factors and the exponents are $C_{1,s} = 0.90 \pm 1.22$, $C_{2,d} = 0.42 \pm 0.09$, $\beta' = -0.24 \pm 0.03$, $\gamma' = -0.24 \pm 0.01$. The slope method does not change the BL scaling exponent compared to the displacement method. In the case of the thermal BL, it unravels the differences between the DNS and the experiment, which have been discussed already in section 5.1.2. The conclusion is that we have the same exponents of scaling laws even by the slope method, though the BL thicknesses calculated by this method are thinner than computed by displacement method.

The shear Reynolds number has been defined as a criterion to judge the potential transition of a BL from the laminar toward the turbulent state [75]. It is given by:

$$\text{Re}_s = \frac{\delta_v \langle U_{max} \rangle}{\nu}, \quad (5.3)$$

where δ_v denote the viscous BL thickness, $\langle U_{max} \rangle$ is a typical mean velocity of the outer velocity BLs and ν denotes the kinematic viscosity. For an isothermal, zero-pressure gradient BL according to the model of Prandtl and Blasius the authors in [75] estimated a critical value of $\text{Re}_s \approx 420$. In turbulent RB convection the stability of the BL may not only be disturbed by the shear which increases with rising velocity but also by thermal plumes detaching from the BL or by coherent structures in the flow field. These effects may lower the stability limit of the BL and may induce a transition towards a turbulent regime even at significantly smaller Re_s (e.g. Preston predicted $\text{Re}_s = 320$, based on momentum boundary layer thickness [76]). In Fig. 5.6, the shear Reynolds numbers are plotted in a range between $\text{Ra} = 10^9$ and $\text{Ra} = 10^{12}$ (including earlier measurements data, see in table 5.1). Re_s keeps increasing with Ra and experimental and numerical data fit very well. In order to estimate the Ra numbers at which the trend crosses the critical limits $\text{Re}_s = 320$ or $\text{Re}_s \approx 420$ we extrapolated the data points using a regression $\text{Re}_s \sim \text{Ra}^{0.267 \pm 0.0386}$. According to this fit the lowest possible Ra number for a transition to a turbulent state amounts to $\text{Ra}_c \approx 2.65 \times 10^{12}$ for $\text{Re}_s = 320$, to $\text{Ra}_c \approx 7.3 \times 10^{12}$ for $\text{Re}_s = 420$, which both are in the same order 10^{12} and would be below the prediction of Grossmann and Lohse in [31] and the recent experimental findings ($10^{13} \lesssim \text{Ra} \lesssim 5 \times 10^{14}$ by He *et. al.* [77]). However, it

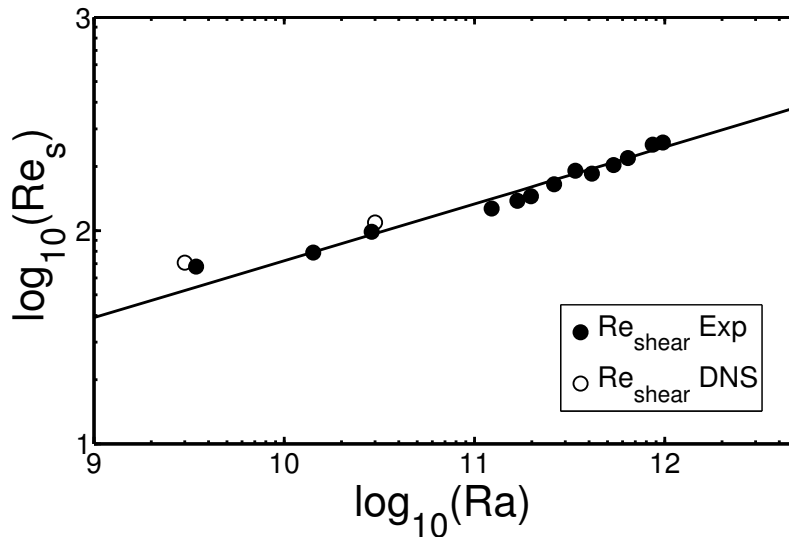


Figure 5.6: Shear Reynolds number Re_s versus Ra from experiment (closed circles) and DNS (open circles) [1]. The solid line is the fit to all data.

cannot be ruled out that due to the plume inside the BLs as well as the strongly three-dimensional flow in turbulent RB convection and the complex dynamics of the LSC this transition may take place at even lower Rayleigh numbers. The exact parameters and the results can be found in table 5.1 and 5.2.

5.1.4 Velocity profiles out of the center line

In RB cells of aspect ratio one and smaller, the sidewall significantly affects the flow inside the cylindrical enclosure. Therefore, it is justifiable to ask whether or not the results obtained at the center of the cooling plate can be generalized to the entire area? We will discuss measurements and numerical results obtained at three other positions 1, 2 and 3 (see Fig. 3.1). In our experiment in the small cell, we tried to lock the wind in a certain direction. We realized this by stretching the plexiglass sidewall along the diameter for about 1 % on each side. Locking the wind in this way, we can assign certain positions at the plate to areas of up-welling and down-welling plumes (position 1 and 2) as well as outside of the large-scale circulation (position 3). This assignment is not possible in the DNS since the mean angle of the LSC plane slowly drifts and these distinct areas are not well defined (see Fig. 4.14). Because of the different behavior of the LSC we will, therefore, not directly compare the data from the experiment with the numerical ones in this section.

First, we present the experimental and DNS mean horizontal velocity profiles [1] at $Ra = 3 \times 10^{10}$ in Fig. 5.7 (a) and (b). In order to show a potential deviation from the profile at the central axis the velocity is normalized by the same value $\langle U_{max} \rangle$ as used in Figs. 5.1 and 5.2. The maximum of the

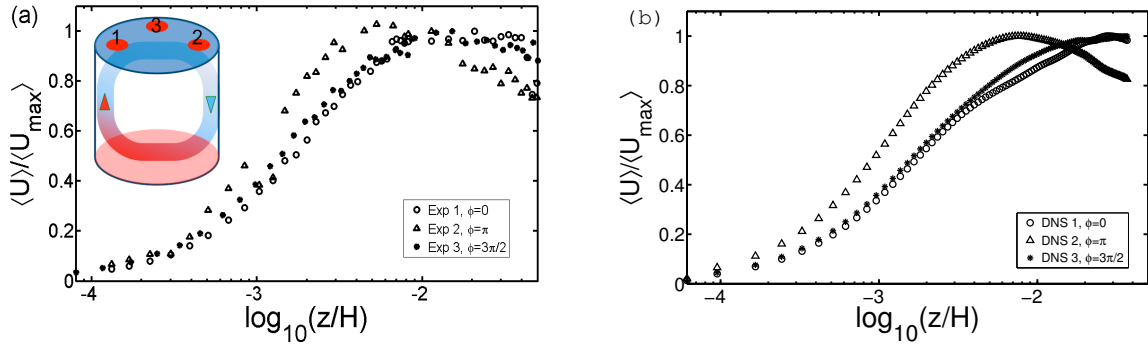


Figure 5.7: Mean horizontal velocity profiles at side window 1, 2 and 3, are located at $r = 0.88 R$ and $\varphi = 0, \pi$ and $3\pi/2$ of the corresponding DNS model [1]. (a) Profiles of the measured data at $Ra = 2.88 \times 10^{10}$, at window 1 (circle), window 2 (triangle) and window 3 (star). (b) Profiles of the DNS data at $Ra = 3 \times 10^{10}$ at array 1 (circle), array 2 (triangle) and array 3 (star). The three locations are shown in the inset with reference to the mean flow.

5 Results: velocity and temperature profiles from the small convection cell

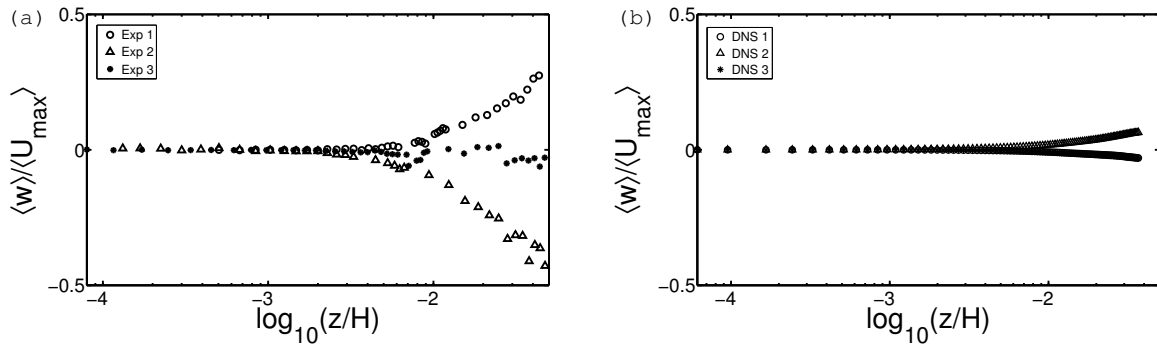


Figure 5.8: Mean wall-normal velocity profiles at side window 1, 2 and 3. (a) Profiles of the measured data at $Ra = 2.88 \times 10^{10}$, at window 1 (circle), window 2 (triangle) and window 3 (star). There is a clear pair of up-welling and down-welling mean velocities. (b) Profiles of the numerical data [1] at $Ra = 3 \times 10^{10}$ at array 1 (circle), array 2 (triangle) and array 3 (star).

velocity at the outer positions is below the value at the center line (non-normalized maximum velocity see table 5.4). This implies a reduction of the local heat transfer coefficient and, hence, a decrease of the local Nu. All three measured profiles rise with a different gradient toward their maximum and the thickness of the viscous BL varies, which means the heat flux are locally different. Unlike at the central axis of the experiment the mean wall-normal velocity at the windows 1 and 2 (begin and end of the path of the LSC along the cooling plate) clearly deviates from zero. Figure 5.8 (a) shows that at the area of up-welling plumes (Exp 1) a positive w component has been measured, while this velocity component is negative at the area of down-welling plumes (Exp 2). At window 3 (Exp 3) which is outside the LSC the mean of w tends to zero. Since in the DNS areas of up- and down-welling plumes are not assigned

| position | $\langle U_{max} \rangle$ | δ_v | δ_θ | δ_v/H | δ_θ/H |
|----------|---------------------------|------------|-----------------|--------------|-------------------|
| | (m/s) | (mm) | (mm) | | |
| Center | 0.224 | 4.335 | 7.211 | 0.00173 | 0.00288 |
| Exp 1 | 0.132 | 5.112 | 7.713 | 0.00204 | 0.00309 |
| Exp 2 | 0.129 | 2.204 | 6.022 | 0.00088 | 0.00241 |
| Exp 3 | 0.162 | 4.723 | 7.738 | 0.00189 | 0.00310 |

Table 5.4: Set of parameters and selected results of the velocity and temperature measurements at $Ra = 2.88 \times 10^{10}$ at various locations. $\langle U_{max} \rangle$ is the maximum of the velocity, δ_v and dimensionless δ_v/H are the displacement thicknesses for the viscous BL, δ_θ and dimensionless δ_θ/H are the displacement thicknesses for the thermal BL.

with distinct positions at the cooling plate the observed effect is weaker, but clearly visible too (see Fig. 5.8(b)). The viscous and thermal BL thicknesses at these three locations have been calculated as well, see table 5.4. Generally the thermal BL thickness is always thicker than viscous BL thickness in our case at $Pr = 0.7$. We found that BL thickness is not uniform and it is strongly dependent on its location. From the thinnest to the thickest BLs at all four locations we have measured a variation by a factor of 2.3 of their thicknesses. The thinnest BL thickness does not occur at the center (maximum mean horizontal velocity) as we expected, instead there is a sudden thickness decrease at side window 2.

In summary, a wall-normal velocity unequally from zero has been detected, particularly at the areas where the plumes hit or leave the cooling plates. Again it was verified that a LSC exists at $\Gamma = 1$.

5.1.5 Turbulent stress invariant analysis

The heat transfer is mainly determined by the complex flow processes in the BL. Previously, we have only studied the magnitude of the horizontal velocity $U = \sqrt{u^2 + v^2}$. How does the turbulent fluctuation of each component, u , v , w , effect the time-averaged flow field, described by the Reynolds stress? The 3-component velocity vectors and their fluctuations give us the opportunity to analyze the Reynolds-stress distribution and its transport in the turbulent flow. In this chapter, we preliminarily calculate the anisotropy tensor of turbulence, which was first introduced by Lumley [78]. The specific calculation [79] is like following:

$$a_{ij} = \frac{\overline{u_i u_j}}{2k} - \frac{\delta_{ij}}{3}, k = \frac{\overline{u_i u_i}}{2}, \quad (5.4)$$

and its first, second and third anisotropy invariants (I, II, III) are:

$$\text{I} = a_{ii}, \text{II} = a_{ij} a_{ji}, \text{III} = a_{ij} a_{in} a_{jn} \quad (5.5)$$

In the equations, a_{ij} is the Reynolds stress anisotropy tensor and i, j are tensor indices. Here we apply the latest anisotropy-invariant map, introduced by Banerjee [80], to present a non-distorted visual representation of anisotropy in turbulent quantities. Figure 5.9 shows a 2-component anisotropy turbulence near the wall, represented by u, w or v, w components. At larger distance from the wall, we find 3-component isotropy turbulence, which means all three u, v, w components have strong fluctuation. According to a study [79], based on the 3D velocity data of BOI, the transition from 2-component turbulence to 3-component turbulence always occurs at the viscous BL region at all investigated locations. At the central window, the transition from 2-component anisotropy turbulence to 3-component one is faster than the other three positions out of center.

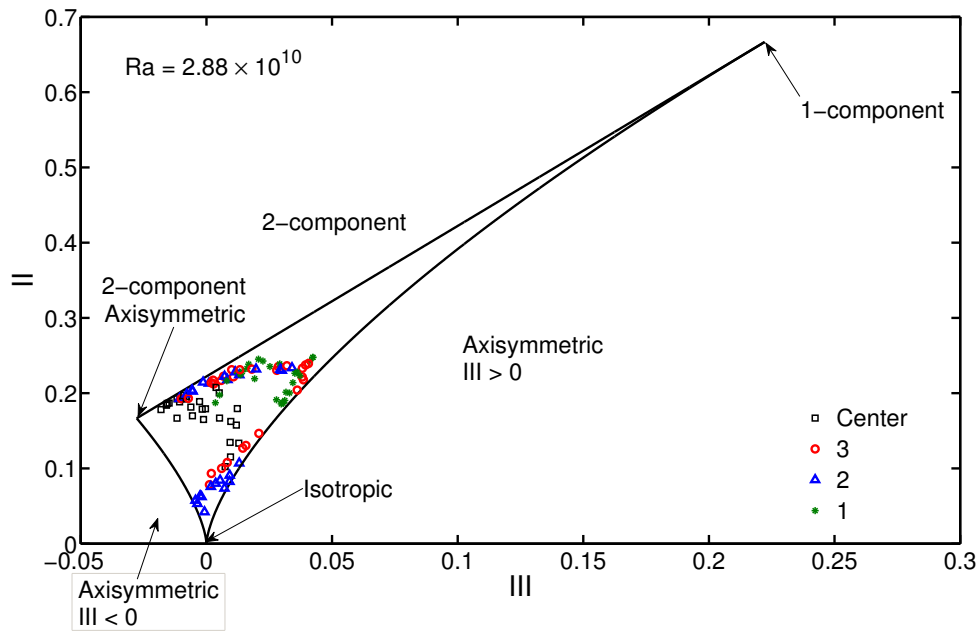


Figure 5.9: Anisotropy invariant map with calculated data based on the 3D velocity data measured from the BOI at different locations, at the center line (empty square), at side window 1 (asterisk), at side window 2 (empty triangle) and at side window 3 (empty circle)

In summary, the turbulence inside and outside the BL with respect to its isotropy or anisotropy is investigated. The result shows that inside the BL, the turbulence is mostly in the region of 2-component anisotropy and outside the BL, the turbulence is mostly between the axisymmetric boundary and the isotropy region.

5.2 Velocity and temperature profiles at aspect ratio $\Gamma = 2.76$

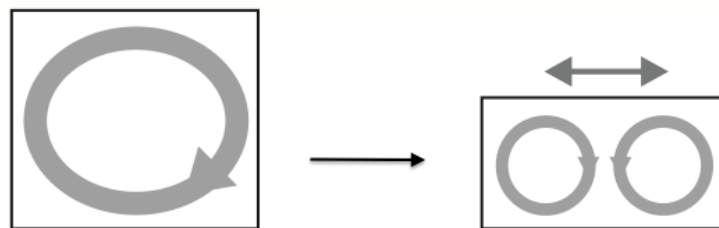


Figure 5.10: Sketches of hypothetical flow pattern transfers from $\Gamma = 1$ (left) to $\Gamma = 1.89$ (right)

For any convection experiment in the laboratory, a lateral sidewall is inevitable. The parameter Γ , which

describes the geometry of the convection cell, has also influence with $Nu(Ra, Pr, \Gamma)$. There are some measurements focusing on aspect ratio dependency [5, 14, 81, 82, 83, 84, 85, 86, 87]. The earlier experiments and numerical simulations in a cylindrical cell [18, 88, 89] have shown that with increasing aspect ratio, the velocity and temperature distributions and the flow structures in the cell change as well. First, in the experimental velocity study (two horizontal components) from the BOI, du Puits [18] found that $\Gamma = 1.89$ was a critical aspect ratio, at which the LSC split from a single roll to two rolls, shown in figure 5.10. Later in a 3D DNS study, Bailon [89] found that $\Gamma = 2.5$ at $Ra = 10^7$ was the critical aspect ratio, at which the LSC split down. A 3D experimental study in air at Γ higher than 1 is still unexplored. In this chapter, we present 3-component mean velocity and temperature profiles at various locations at $\Gamma = 2.76$ and $Ra = 1.27 \times 10^9$. The experimental conditions are still the same with the measurements at $\Gamma = 1$, which have been described in chapter 3. We decreased the height of the small cell to 0.905 m and kept the diameter of 2.5 m. In order to trap the “wind”, the small cell has also been stretched along the central axis of window 1, central window and window 2 for 2 cm on each side.

5.2.1 Velocity and temperature profiles at the center line

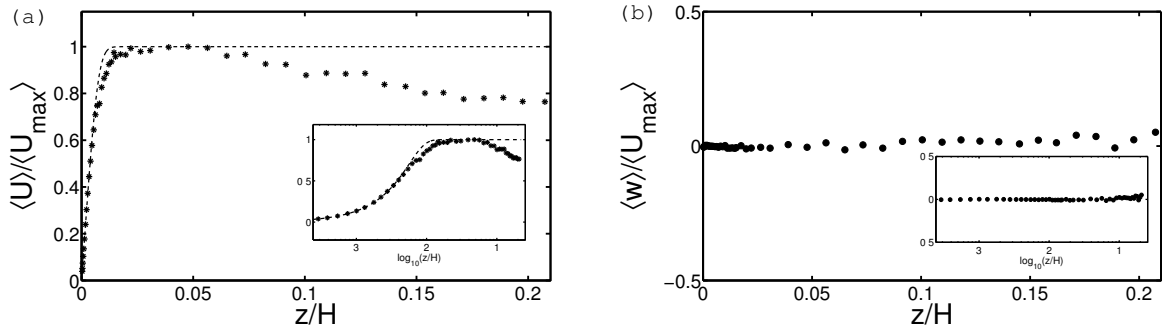


Figure 5.11: Profiles of the mean horizontal velocity (a) and the mean wall-normal velocity (b) measured at the center of the cooling plate at $Ra = 1.27 \times 10^9$, $\Gamma = 2.76$. The dashed line on top of the mean horizontal velocity is the Blasius profile. The insets shows the entire mean velocity profiles in logarithmic scale.

First we present the mean horizontal and wall-normal velocity profiles at the center line, $\langle U(z) \rangle$ and $\langle w(z) \rangle$ at $Ra = 1.27 \times 10^9$, as shown in Fig. 5.11. U is defined by equation (4.12). Both of horizontal and wall-normal velocity are normalized by the maximum mean horizontal velocity, $\langle U_{max} \rangle = 0.176$ m/s. The x axis is normalized by the height of the cell with 0.905 m. The mean horizontal velocity profile has a clear decreasing trend after the BL region compared to the mean profile at $\Gamma = 1$, in figure 5.1, which means the “wind” is getting weaker. With the mean velocity going down, the LSC has

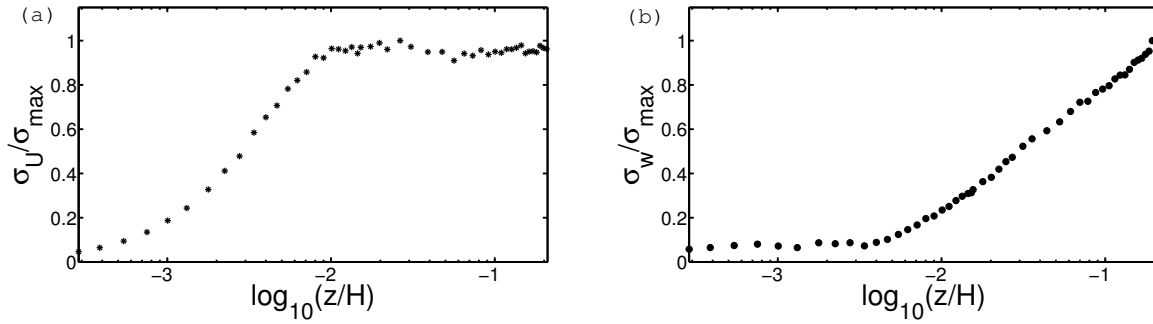


Figure 5.12: Profiles of the mean horizontal (a) and the mean wall-normal velocity fluctuations (b) measured at the center of the cooling plate at $Ra = 1.27 \times 10^9$, $\Gamma = 2.76$, plotted in linear scale. The insets are the entire profile plotted in logarithmic scale.

the trend to transit from a single-roll to a double-roll structure. The wall-normal component still keeps the trend going to zero, which means that the single-roll has not yet split until 200 mm distance from the cooling plate. Otherwise, we should see a non-zero mean wall-normal velocity.

Second, as the previously presented mean horizontal profiles at $Ra = 3 \times 10^9$ and $\Gamma = 1$ in figure 5.1 (a), both of the experimental and numerical results deviate from the Blasius profile. At $Ra = 10^9$, but at $\Gamma = 2.76$, we can see the mean horizontal velocity gets closer to Blasius-type flow.

The directly measured horizontal and wall-normal velocity fluctuations are shown in figure 5.12 (a) and (b) respectively. They are normalized by their respective maximum fluctuations. compared to the horizontal velocity fluctuation at $\Gamma = 1$ in figure 5.1 (b), at $\Gamma = 2.76$ the horizontal velocity fluctuations increase in the BL and are constant out of the BL region until 200 mm depth. The wall-normal fluctuations keep constant within the BL ($\delta_v \approx 4.5$ mm), but they increase moving outside BL.

In figure 5.13 (a) and (b), the mean temperature profile (asterisk) and its fluctuation measured at $Ra = 1.27 \times 10^9$ ($\Delta T = 20$ K) and $\Gamma = 2.76$ at the center line are shown (temperature data refer [4]). The mean temperature profile is normalized by the temperature difference as measured between bulk and cooling plate. The Pohlhausen solution is plotted on top of it. Recall the situation at $\Gamma = 1$, in figure 5.3, the mean temperature profile at $\Gamma = 2.76$ is still different from the Pohlhausen solution. The thermal BL thickness is calculated by the displacement method $\delta_\theta/H = 2.5 \times 10^{-3}$ and it is thinner compared to the thermal BL thickness at $Ra = 3 \times 10^9$, $\delta_\theta/H = 4.1 \times 10^{-3}$ in table 5.2, as Γ increased. The heat flux depends crucially on the shape of the mean temperature profile. The local wall heat flux is defined as $\dot{q}_w = -\lambda_{th} \frac{dT}{dz}$. The inset of figure 5.13 (a) shows that the local heat flux measured at $Ra = 3 \times 10^9$

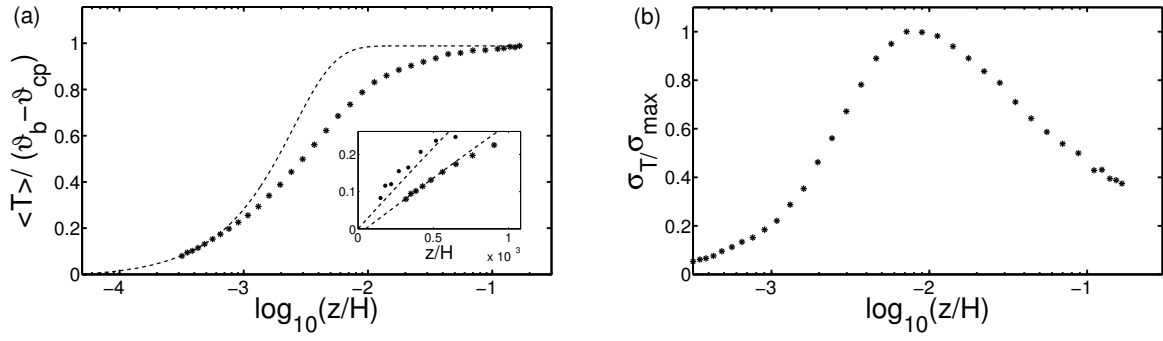


Figure 5.13: Profiles of the mean temperature (a) and its fluctuations (b) measured at the center line of the cooling plate at $Ra = 1.27 \times 10^9$ ($\Delta T = 20$ K), $\Gamma = 2.76$ [14], plotted in logarithmic scale. Here, ϑ_b and ϑ_{cp} denote the mean bulk temperature and the surface temperature of the cooling plate. Pohlhausen solution is plotted on top of the mean temperature profile at $\Gamma = 2.76$. The inset is the linear plot of the vicinity data of the cooling plate, which shows the gradients of mean temperature profiles, at $Ra = 3 \times 10^9$ $\Delta T = 2.4$ K, $\Gamma = 1$ (full circle), at $Ra = 1.27 \times 10^9$ ($\Delta T = 20$ K), $\Gamma = 2.76$ (asterisk).

and $\Gamma = 1$ (gradient of the mean temperature profile (full circle) counted by the first 6 data points), is 1.4 times larger than that measured at $Ra = 1.27 \times 10^9$ and $\Gamma = 2.76$ at the center line. As Γ is increasing, the local wall heat flux is decreasing.

5.2.2 Velocity and temperature profiles out of the center line

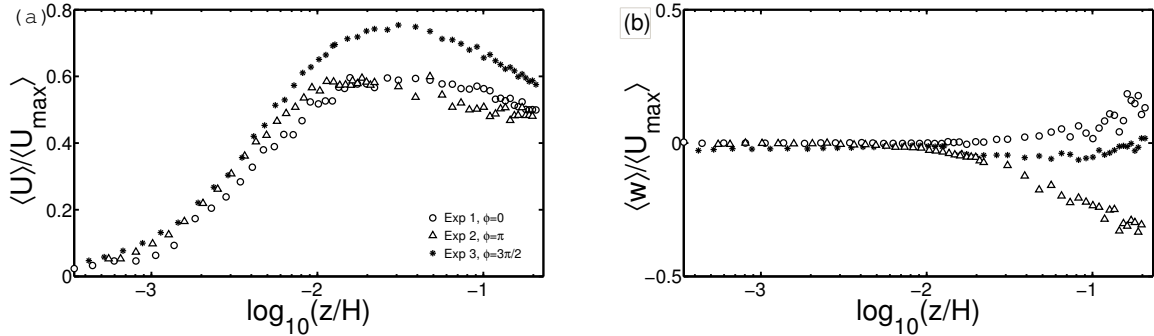


Figure 5.14: Mean horizontal (a) and wall-normal (b) velocity profiles measured at side window 1, 2 and 3, which are located at $r = 0.88 R$ and $\varphi = 0, \pi$ and $3\pi/2$, see in Fig. 3.1. All profiles measured at $Ra = 1.27 \times 10^9$, $\Gamma = 2.76$, at window 1 (circle), window 2 (triangle) and window 3 (star), plotted in logarithmic scale.

In this section, all the mean velocity and temperature profiles are measured at $Ra = 1.27 \times 10^9$ and $\Gamma = 2.76$ (temperature data refer [14]), at three different positions out of the center line of the convec-

5 Results: velocity and temperature profiles from the small convection cell

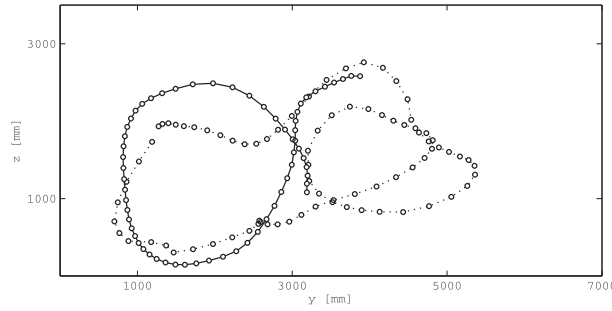


Figure 5.15: 2D plot of reconstructed long-term (over 60 min) 3D trajectory representing the transition between large single-roll and small single-roll in the whole cross section of the convective cell (dotted) and a small single-roll in the half cross section of the cell (solid line) at aspect ratio $\Gamma = 2$ and $Ra = 1.3 \times 10^{11}$ [90].

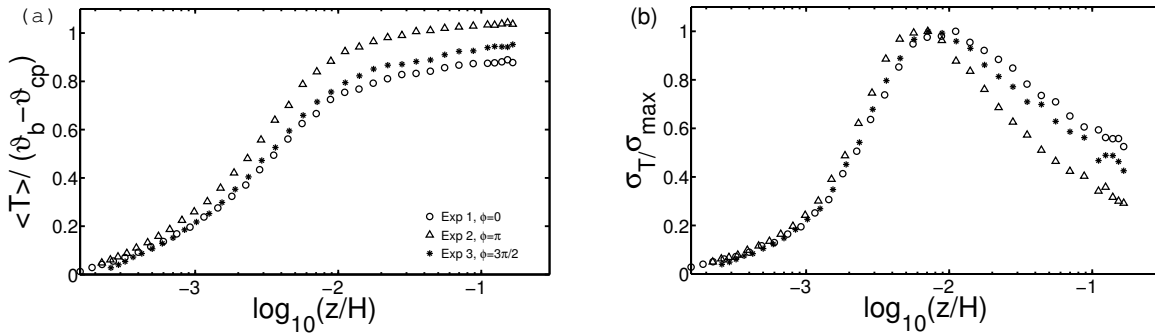


Figure 5.16: Profiles of the mean temperature (a) and its fluctuations (b) measured at side window 1, 2 and 3, at $Ra = 1.27 \times 10^9$, $\Gamma = 2.76$ [14], plotted in logarithmic scale. Here, ϑ_b and ϑ_{cp} denote the mean bulk temperature and the surface temperature of the cooling plate.

tion cell. In order to show a potential deviation from the profile at the central line, both the velocities are normalized by the same value $\langle U_{max} \rangle$ as used in figure 5.11, $\langle U_{max} \rangle = 0.176$ m/s. The non-normalized maximum velocity can be found in table 5.5. The horizontal velocity at different locations, shown in figure 5.14 (a) increases following the distance with different gradients, which shows again, that the viscous BL thickness varies from different positions. A clear pair of up-welling and down-welling mean that a wall-normal velocity has been observed, see figure 5.14 (b). We conclude, that at $\Gamma = 2.76$ the LSC is in the transition mode between a large single-roll and two small single-rolls. This pattern is as Lobutova found from the three-dimensional particle tracking velocimetry (PTV) measurement [90], see figure 5.15. The PTV measurement was conducted in the BOI at aspect ratio $\Gamma = 2$ and $Ra = 1.3 \times 10^{11}$ ($\Delta T = 40^\circ\text{C}$) by recording long-term balloons' trajectories for more than 60 minutes. Figure 5.15, shows that the single-roll does not have a regular elliptical trajectory and does not fill out the whole cross section of the convection cell. It tends from one single-roll (dotted) to another more

| position | $\langle U_{max} \rangle$ | δ_v | δ_θ | δ_v/H | δ_θ/H |
|----------|---------------------------|------------|-----------------|--------------|-------------------|
| | (m/s) | (mm) | (mm) | | |
| Center | 0.176 | 4.418 | 6.922 | 0.00488 | 0.00765 |
| Exp 1 | 0.103 | 4.118 | 6.809 | 0.00455 | 0.00752 |
| Exp 2 | 0.101 | 2.863 | 5.431 | 0.00316 | 0.00600 |
| Exp 3 | 0.126 | 4.101 | 6.392 | 0.00453 | 0.00706 |

Table 5.5: Set of parameters and selected results of the velocity and temperature measurements at $Ra = 1.27 \times 10^9$, $\Gamma = 2.76$ at various locations. $\langle U_{max} \rangle$ is the maximum of the velocity. δ_v and dimensionless δ_v/H are the displacement thicknesses for the viscous BL. δ_θ and dimensionless δ_θ/H are the displacement thicknesses for the thermal BL.

complicated flow pattern (solid line) at $\Gamma = 2$.

Figure 5.16 (a) and (b) show the mean temperature profiles and their fluctuations measured at $Ra = 1.27 \times 10^9$ ($\Delta T = 20$ K) and $\Gamma = 2.76$ at side window 1, 2 and 3. The viscous and thermal BL thickness are calculated from the mean velocity and temperature profiles by the displacement method, which has been introduced in the ‘‘Boundary layer scaling’’ section, see table 5.5. The different temperature gradients of the mean profiles show that the wall heat flux varies locally. Both of the viscous and thermal BL thicknesses at center line are thicker than at the side windows, which indicates that the LSC does not have a regular elliptical pattern and has the tendency to break down to another structure, such as a small single-roll or a double-roll structure.

In summary, at $Ra = 1.27 \times 10^9$ and $\Gamma = 2.76$ we observed that the flow does not have a regular BL thickness distribution. It might be caused by the irregular elliptical flow pattern, which does not fill out the whole cross section of the convection cell. A clear double-roll structure has not been observed, because the upwards and downwards directed wall-normal velocities measured at the side windows do not fit with the double-roll moving mechanism.

6.1 Simultaneous velocity and temperature profiles and their fluctuations at the center line

The heat transport in turbulent convection is determined primarily by thermal plumes, but its transport mechanism has not yet been clearly understood. Basically, the phenomenological theories predicting the global heat transport in turbulent RB convection consider diffusive and convective heat transport throughout the BLs. With the assumptions of a thin BL, it can be written as [91]:

$$\dot{q} = \dot{q}_d + \dot{q}_c = -\lambda_{th} \frac{dT}{dz} + c_p \rho \langle w' \cdot T' \rangle_t, \quad (6.1)$$

\dot{q} is the total heat flux. \dot{q}_d and \dot{q}_c represent diffusive heat flux and convective heat flux respectively. In order to quantify the diffusive term, the temperature gradient has to be measured, which has been done as a local and step-by-step measurement using a thermistor. From these measurements [4, 14] they concluded that the heat is transported convectively inside and outside the BL even at Rayleigh numbers below the transition to the ultimate regime. In these comprehensive temperature studies, the wall-normal velocity fluctuation has not been considered. Simultaneous measurements of the temperature and the wall-normal component velocity will help to understand the heat transport better. The first simultaneous measurements in RB convection were conducted in a cylindrical cell filled with water by Xia and Tong in 2003 [53] and 2004 [52]. The measurement was performed up to $Ra = 7.6 \times 10^9$ and $\Gamma = 1$ and only outside the BL. In this work, we have the chance to study the wall-normal velocity and temperature fluctuations inside and outside the BL with much better spatial resolution at $Ra = 8.96 \times 10^{11}$ and $\Gamma = 1.13$. The measurements have been undertaken at the center line of the convection cell at the

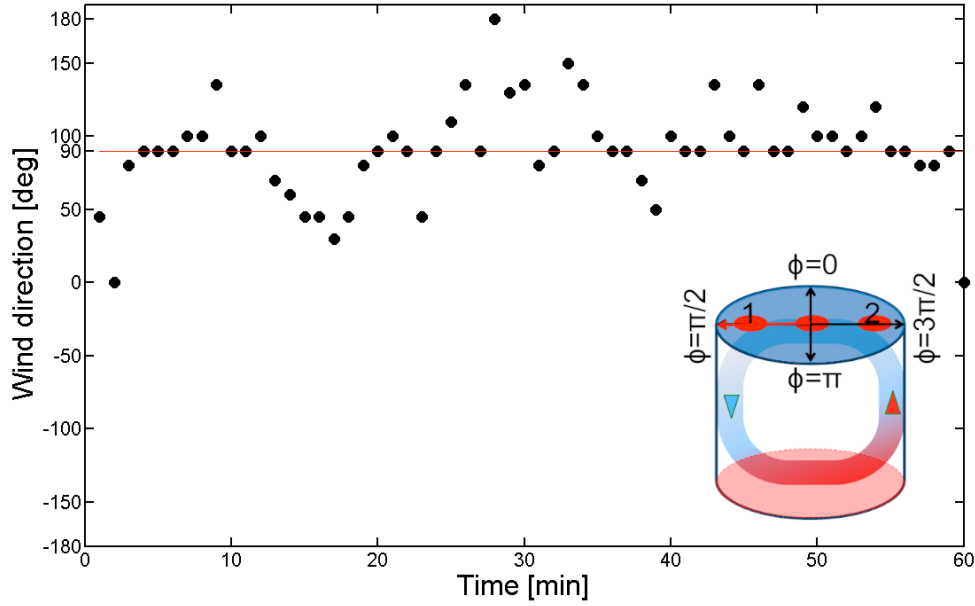


Figure 6.1: Time series of the main wind direction in the BOI. The inset shows the LSC in RB cell. The red line denotes the 90 degree direction of the locked orientation of the LSC.

cooling plate. Moreover, we have studied the local heat transport also at the side windows 1 and 2, shown in figure 4.12, where warm plumes from the lower cell section hit the surface and cold plumes detach from the cooling plate surface.

In this chapter we first study the local wall-normal velocity $\langle w(z) \rangle$ and the temperature T and their fluctuations in the large convection cell ($H = 6.3$ m, $D = 7.14$ m) at $Ra = 8.96 \times 10^{11}$ and $\Gamma = 1.13$ at the center line. The temperature difference is $\Delta T = T_h - T_c = 65 - 15 = 50$ K. The bulk temperature amounts to $T_b = 40^\circ\text{C}$. At this temperature, the air properties are: $\nu = 1.73 \times 10^{-5}$ m²/s, $\kappa = 2.42 \times 10^{-5}$ m²/s, $\lambda_{th} = 0.027$ W/m · K (heat conductivity) and $c_p = 1.007$ kJ/kg · K (heat capacity). Later for the heat flux calculation, the temperature dependency of the fluid properties are considered. The typical sampling rates of the velocity and temperature measurements are 50 Hz and 200 Hz, respectively. Both were measured for one hour at each measuring point. The measuring distance covers from 2.4 mm to 160 mm away from the cooling plate. The first measuring point at 2.4 mm is limited by the construction of the measurement set-up.

Before all the measurements can be run, we need to pin down the azimuthal rotation of the LSC. Actually, a “locked LSC” has been found by a earlier viscous BLs structure study in the BOI [19]. In this

paper, the mean angle of the horizontal velocity vector for a 48h profile measured at $Ra = 5.38 \times 10^{11}$ and $\Gamma = 1.13$ shows that the flow direction undergoes variations of about $\pi/4$. We have also been watching the wind orientation in this work for one hour, see the time series in figure 6.1. The 1h watching time is based on the conclusion of the earlier study, that the wind has already been pinned down and confirms the actual wind orientation during the simultaneous velocity and temperature measurement. The wind direction measurement was performed with degree markers, drawn on the glass surface of the central window and a light nylon thread was glued under the window. The angular of the mean flow was recorded every minute. The LSC plane is found vertically located along the line of the three windows in the cooling plate with ± 45 degree fluctuating around, see figure 6.1 and its inset. The temperature measurement set-up is mounted in adverse wind direction of the main wind.

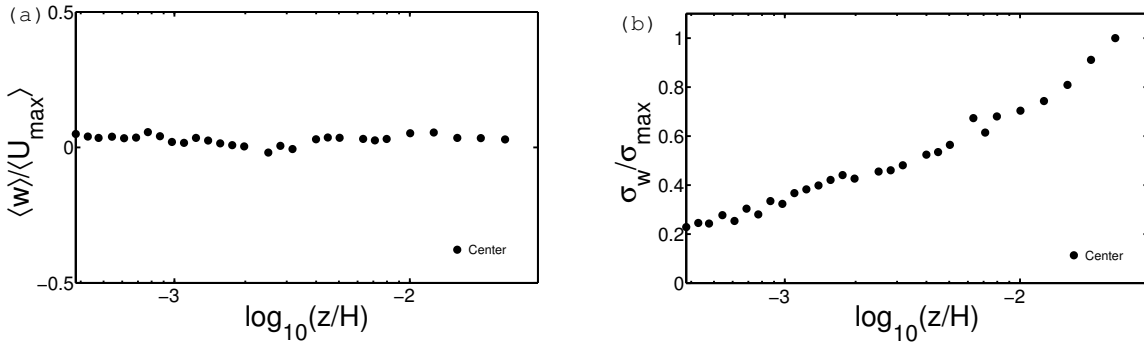


Figure 6.2: Measured wall-normal velocity profiles at $Ra = 8.96 \times 10^{11}$, $\Gamma = 1.13$ at the center line plotted in logarithmic scale. (a) Profile of the mean wall-normal velocity normalized by the maximum mean horizontal velocity. (b) Profile of the mean wall-normal velocity standard deviation normalized by its maximum.

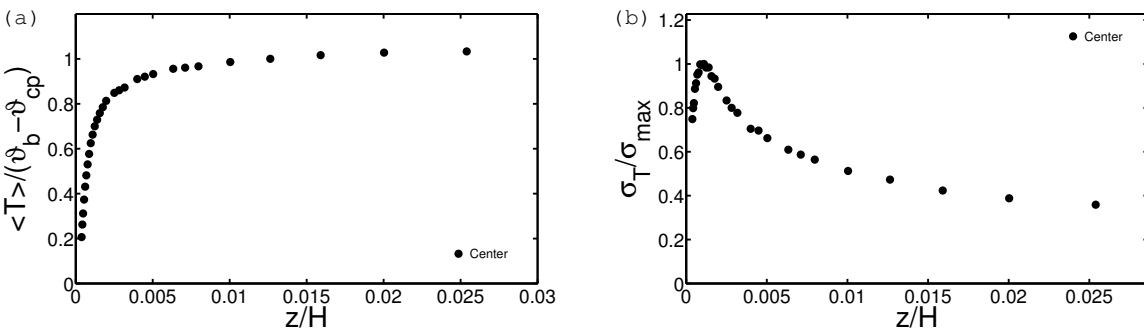


Figure 6.3: Measured temperature profiles at $Ra = 8.96 \times 10^{11}$ and $\Gamma = 1.13$ at the center line. (a) Profile of the mean temperature normalized by the temperature difference of $\vartheta_b - \vartheta_{cp}$. (b) Profile of the temperature standard deviation normalized by its maximum. Here ϑ_b and ϑ_{cp} denote the mean bulk temperature and the surface temperature of the cooling plate.

First, we discuss the mean velocity and temperature profiles measured at the center line, see the inset of figure 6.1. We present the profiles of mean wall-normal velocity and its standard deviation at $Ra = 8.96 \times 10^{11}$ and $\Gamma = 1.13$ in figure 6.2 (a). The mean wall-normal velocity is normalized by the maximum mean horizontal velocity $\langle U_{max} \rangle = 0.545$ m/s, measured earlier at $Ra = 8.64 \times 10^{11}$ and $\Gamma = 1.13$. The mean wall-normal profile still trends to zero, similar to the results we found in the earlier 3D velocity measurements, at lower Rayleigh numbers 10^9 and 10^{10} . Due to the 3D velocity measurement, the mean wall-normal velocity was calculated by the weighted difference of the two measured components u_2 and u_3 by a transformation matrix (4.11), the result is very sensitive to LDA probes alignment angle variations. Another deviation was the “jump” in the mean wall-normal velocity profile, caused by switching between different focal length lenses of the LDA. Therefore, we want to prove the earlier result by this direct measurement using a 1D probe. The wall-normal standard deviation, $\sigma_w(z)$, shown in figure 6.2 (b), is normalized by the maximum wall-normal fluctuation. It keeps increasing until reaching a distance of 160 mm from the cooling plate. The mean temperature profile, shown in figure 6.3 (a), is a rescaled profile according to the early temperature profile measurements [14] at $Ra = 8.59 \times 10^{11}$ and $\Gamma = 1.13$, which was measured for an even longer time of 1.5 h. The reason for this temperature data post-processing is because the original mean temperature profiles have some “jumps”. These especially occurred when the time for measurements occurred at the same time that the window or mirror needed cleaning as well as during the pauses overnight. These fake “jump” data points will have an effect on the calculation of diffusive heat flux, which is strongly dependent on the gradient of mean temperature profile. The mean temperature profile shown in figure 6.3 (a) is normalized by the temperature difference of $(\vartheta_b - \vartheta_{cp})$. The thermal BL thickness is calculated by the displacement method which we introduced earlier in chapter 5 and amounts to $\delta_\theta = 6.55$ mm. The temperature standard deviation σ_T shown in figure 6.3 (b), is the original simultaneous data measured at $Ra = 8.96 \times 10^{11}$ and $\Gamma = 1.13$ and normalized by its maximum. Though part of the data within 2.4 mm is missing, we can still measure the velocity and temperature inside and outside the BL, which can be seen from the maximum (at the BL region) of the temperature standard deviation.

The key feature of velocity and temperature simultaneous measurement is that the plume-generated temperature fluctuations are correlated with the wall-normal velocity fluctuations. The reason is because a group of cold plumes fall down or a group of warm plumes rise up, they always entrain the surrounding air in the downward or upward direction. However, the correlation also depends on spatial separation of LDA measurement volume and temperature sensor tip. From the test measurement, it is clearly shown that the velocity and temperature cross-correlation function $f_c(\tau)$ decreases with the increasing spatial

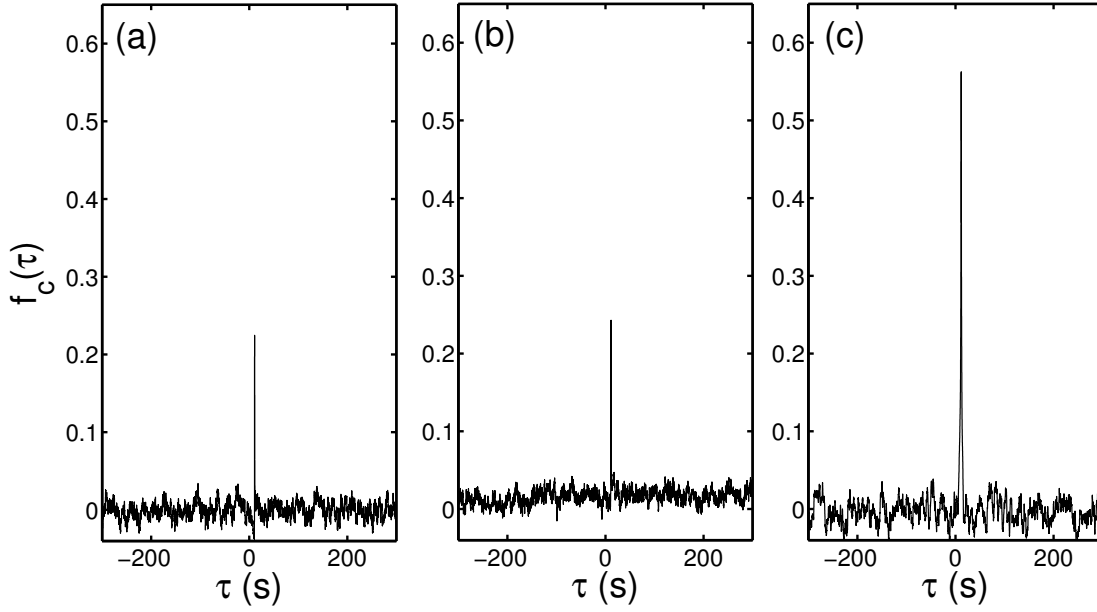


Figure 6.4: Normalized velocity and temperature cross-correlation $f_c(\tau)$ as a function of the delay time τ , at measuring positions $z = 2.4$ mm (a), $z = 6.15$ mm (b) and $z = 160$ mm (c) at the center line. τ is the time delay caused by the measurement starting time and the spatial separation between the LDA measurement volume and thermistor, which is $300 \mu\text{m}$.

separation. We measured the cross-correlation with a minimal spatial separation between LDA measurement volume and thermistor tip of $300 \mu\text{m}$, the calibration is introduced in chapter 4. In figure 6.4 (a), (b) and (c) shows the normalized velocity and temperature cross-correlation as a function of the delay time τ , measured at $z = 2.4$ mm (first measuring point), $z = 6.15$ mm (measuring point around BL region) and $z = 160$ mm (measuring point out of BL) at the center line. The cross-correlation is normalized by a ‘coeff’, function of Matlab, so that the correlations at zero lag are identically 1.0. We see that strength of correlation has a tendency to increase with distance away from the cooling plate. And even at the first measuring point, the correlation amounts to $f_c(\tau) = 0.23$, which is much larger than the background noise at the level of 0.037.

We define the velocity and temperature fluctuations as $w' = w - \langle w \rangle_t$ and $T' = T - \langle T \rangle_t$ respectively. Figure 6.5 (a), (b) and (c) shows the time series of the wall-normal velocity fluctuation w' (blue) and temperature fluctuation T' (red), measured at $z = 2.4$ mm, $z = 6.15$ mm and $z = 160$ mm at the center line. At $z = 2.4$ mm inside the BL, in figure 6.5 (a), the wall-normal velocity fluctuations are skewed towards the positive direction, while at $z = 6.15$ mm (BL region) shown in figure 6.5 (b) and $z = 160$ mm (bulk) shown in figure 6.5 (c), the wall-normal velocities fluctuate symmetrically relative

to the zero mean value. The magnitude of the fluctuations increases with distance away from the cooling plate. In contrast to the situation of velocity fluctuation, the temperature fluctuation inside the BL, shown in figure 6.5 (a), fluctuates symmetrically relative to the zero mean value. It starts to be skewed towards the negative direction at the end of BL, see figure 6.5 (b), which proves again that the plumes are rising up and falling down here. In the bulk, the temperature fluctuations are clearly skewed towards the negative direction.

Figure 6.6 shows the diffusive (green dots) and convective (convective dots) heat flux calculated at the center line. The temperature dependency of the fluid properties has been considered in the calculation of the convective heat flux. Because of the “dead corner” of our measurement, the first measuring point starts from $z = 2.4$ mm, which leads to a large error while calculating the diffusive heat flux right at the cooling plate. There is only diffusive heat flux, then it keeps decreasing to infinity close to zero, see figure 6.6. In contrast to the diffusive heat flux, the convective heat flux (red dots) is almost zero right at the cooling plate, then it keeps increasing until it reaches a maximum value (100.4 W/m^2), which is similar to the diffusive one at the cooling plate (113.3 W/m^2). The ratio between convective and diffusive heat flux is calculated, when the ratio reaches ≈ 1 from 0.11 at the very beginning, the data point is at $z = 6.9$ mm, where also has the maximum temperature fluctuation among all the measuring positions. The thermal BL thickness is calculated by the displacement method with $\delta_\theta = 6.55$ mm. In figure 6.6, from the other point of view, the crossing point of the diffusive and convective heat flux curves is at $z = 6.9$ mm (ratio between convective and diffusive heat flux ≈ 1), where is very close to the thermal BL thickness of $\delta_\theta = 6.55$ mm (refer table 5.2). The conclusion is that the diffusive heat flux dominates inside the BL, while the convective heat flux dominates in the bulk. Figure 6.7 shows the measured total heat flux. Because of the energy conservation, we expected to have a constant volume of total heat flux over z . But the total heat flux is only almost balance at the cooling plate (125.2 W/m^2) and in the bulk (100.5 W/m^2). It drops down in the thermal BL, where the temperature fluctuates stronger than in any other regions. The strong temperature fluctuation requires a fast thermistor, the one used in the current measurement has a maximum capability of 100 ms. It is apparently not fast or small enough to capture all the fluctuations. That might be the reason as to why we do not have a constant total heat flux profile respect to the energy conservation over the whole profile.

In order to characterize the heat transfer through the BL, the wall-normal convective heat flux fluctuations have been studied. Figure 6.8, shows the normalized histograms of the wall-normal convective flux fluctuation $\sigma_{(w'.T')}$ measured at $z = 2.4$ mm (circles), $z = 6.15$ mm (square) and $z = 160$ mm

6.1 Simultaneous velocity and temperature profiles and their fluctuations at the center line

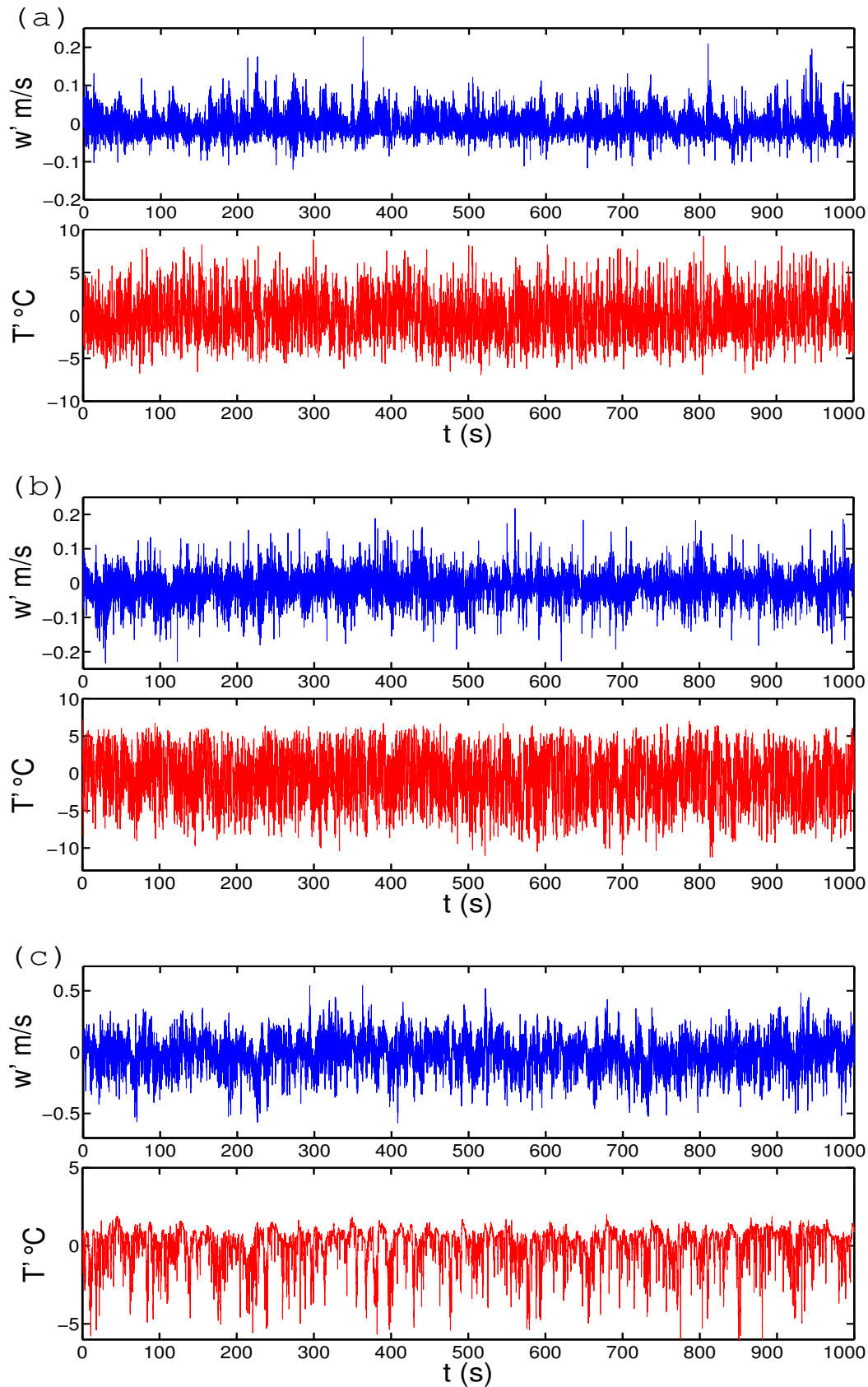


Figure 6.5: Snapshots of measured time series of the wall-normal velocity (blue) and the temperature (red) fluctuations w' and T' . (a) at $z = 2.4$ mm; (b) at $z = 6.15$ mm; (c) at $z = 160$ mm all at the center line.

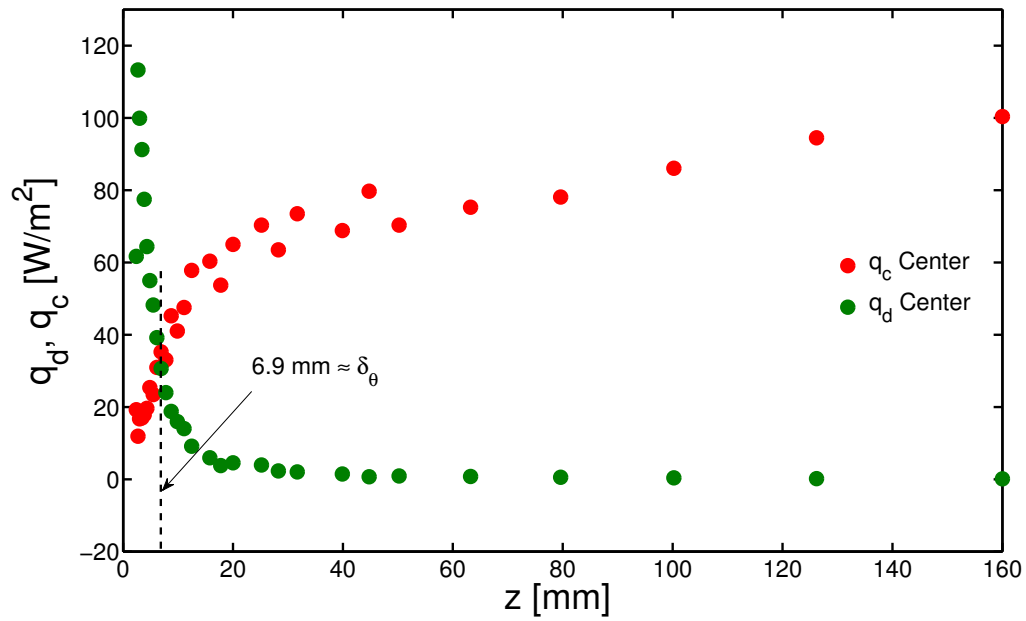


Figure 6.6: Profiles of diffusive heat flux \dot{q}_d (green full circles) and convective heat flux \dot{q}_c (red full circles) calculated from wall-normal velocity and temperature fluctuations at $\text{Ra} = 8.96 \times 10^{11}$ and $\Gamma = 1.13$ at the center line.

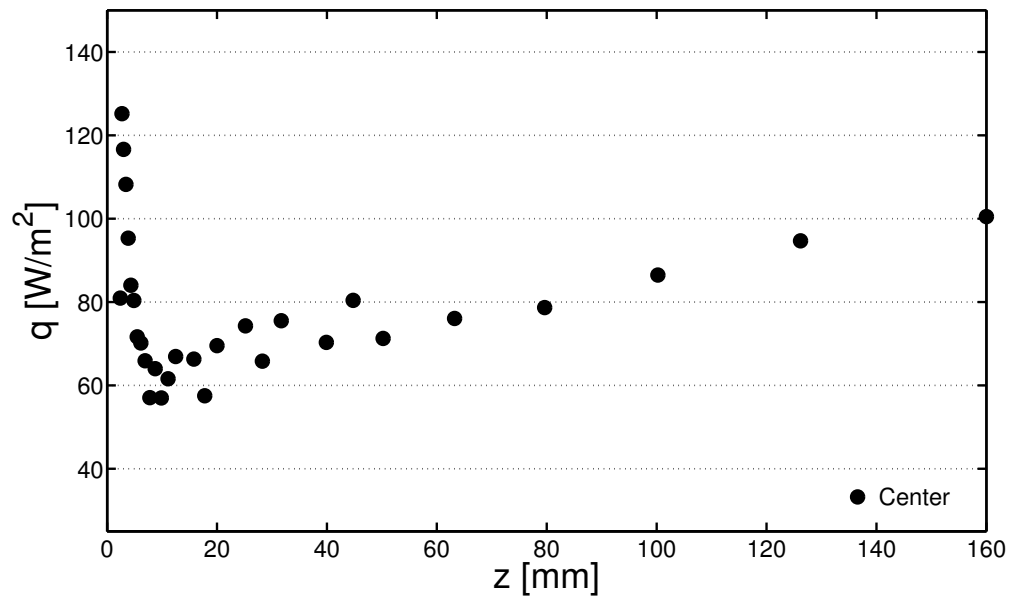


Figure 6.7: Profiles of total heat flux \dot{q} calculated from the velocity and temperature fluctuations at $\text{Ra} = 8.96 \times 10^{11}$ and $\Gamma = 1.13$ at the center line.

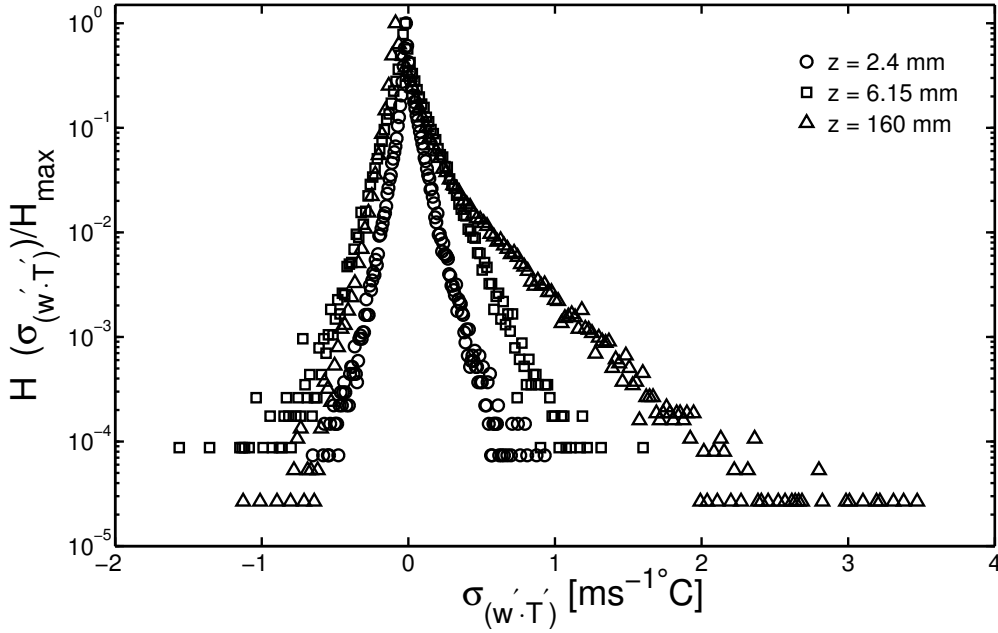


Figure 6.8: Measured histograms of the wall-normal convective flux fluctuation $\sigma_{(w \cdot T')}$, at $z = 2.4$ mm (circles), $z = 6.15$ mm (square) and $z = 160$ mm (triangle) at the center line.

(triangle) at the center line. The fluctuation is $\sigma_{(w \cdot T')} = (w' \cdot T') - \langle w' \cdot T' \rangle_t$. The histogram function, $H(\sigma_{(w \cdot T')})$, is normalized by the maximum of itself. At $z = 2.4$ mm inside the BL, the convective heat flux is almost symmetrically fluctuating around zero and do not contribute to the local heat transport. At $z = 6.15$ mm, BL region, the convective heat flux is slightly skewed towards the positive direction, but at $z = 160$ mm, bulk, the convective heat flux is strongly skewed towards the positive direction. The net gain of the positive fluctuations keep increasing from the BL region until the bulk, in the meanwhile they give rise to a small mean value for the wall-normal fluctuations at the central window.

6.2 Simultaneous velocity and temperature profiles and their fluctuations out of the center line

In this chapter, we discuss the results measured at the side windows 1 and 2, see the inset of figure 6.9, where warm plumes are rising up (window 2) and cold plumes are falling down (window 1) from the cooling plate surface. Can the result at center line be representative for the entire inner region of the plate? To answer this question, it is necessary to know whether the heat transport mechanism is still the same with the situation at the center line or not, since the mean velocities normal to the wall are no longer zero. In figure 6.9, we present the mean wall-normal velocity and its standard deviation profiles at the same $Ra = 8.96 \times 10^{11}$ and $\Gamma = 1.13$. The mean wall-normal velocity is normalized

6 Results: simultaneous velocity and temperature profiles from the large convection cell

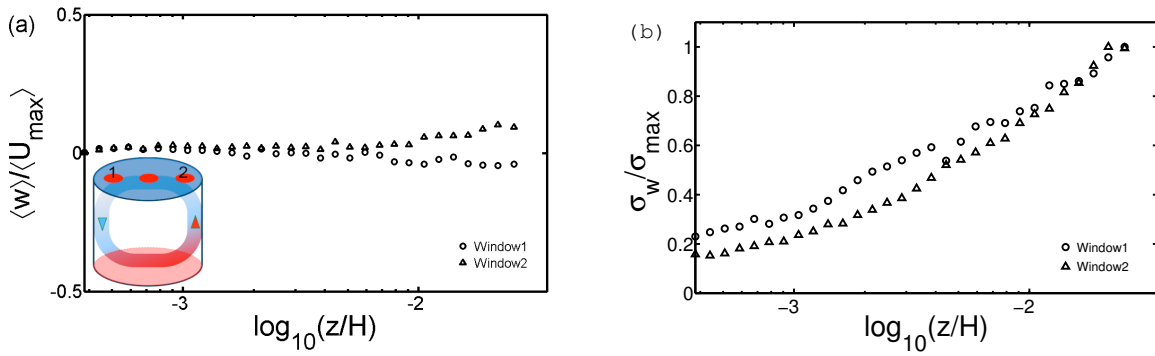


Figure 6.9: Measured wall-normal velocity profiles at $Ra = 8.96 \times 10^{11}$ and $\Gamma = 1.13$ at side window 1 (open circles) and 2 (open triangles), plotted in logarithmic scale. (a) Profiles of the mean wall-normal velocity normalized by the maximum mean horizontal velocity, (b) profiles of the wall-normal standard deviation normalized by their own maximum.

by the maximum mean horizontal velocity, $\langle U_{max} \rangle = 0.545$ m/s, which is the same as the one we used at the center line. From the observed orientation of the wind, there is an upwards velocity at window 2 and a downwards velocity at window 1. Compare with the earlier 3D velocity measurements in the small convection cell (side windows 1 and 2 are 0.15 m from the side-wall), the current result of mean wall-normal velocities have less tendency to go up and down, which is because the side windows 1 and 2 are 1.37 m away from side-wall (19% of the diameter of the cooling plate from the side-wall). Figure 6.9 (b) shows the wall-normal standard deviations, which are normalized by their own maximum. They both keep increasing along the distance. The wall-normal velocity measured at window 1 has stronger fluctuation than the one measured at window 2 according to the higher magnitude of the σ_w .

The mean temperature profiles measured at the side windows are shown in figure 6.10 (a), which are normalized by the temperature difference of $(\vartheta_b - \vartheta_{cp})$. By the same way, the mean temperature profiles have been interpolated as introduced in last section. The local thermal BL thickness is calculated individually at window 1 with $\delta_\theta = 6.32$ mm, at window 2 with $\delta_\theta = 6.55$ mm. It is again verified that the local BL thickness has a variable distribution. Figure 6.10 (b) shows the temperature standard deviation measured at side windows, which are normalized by their own maximum. This demonstrates that we have 8 to 9 measuring points inside the BL. The temperature fluctuation measured at window 1 is stronger than measured at window 2. Since the velocity and temperature standard deviations show us that the down-welling cold plumes have stronger fluctuations than the up-welling warm plumes.

Figure 6.11 and figure 6.12 show the time series of wall-normal velocity fluctuation w' (blue) and tem-

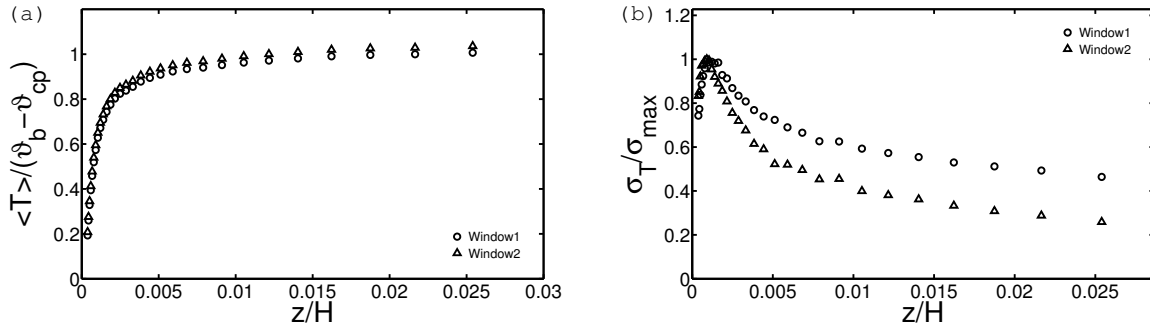


Figure 6.10: Measured temperature profiles at $Ra = 8.96 \times 10^{11}$ and $\Gamma = 1.13$ at side window 1 (open circles) and 2 (open triangles). (a) Profiles of the mean temperature normalized by the temperature difference of $\vartheta_b - \vartheta_{cp}$, (b) profiles of the temperature standard deviation normalized by their own maximum.

perature fluctuation T' (red) measured at $z = 2.4$ mm, $z = 6.15$ mm and $z = 160$ mm at side window 1 and 2 respectively. Except for the similar phenomenon we found at the corresponding positions at the center line, the wall-normal velocity fluctuation has a relatively regular fluctuating pattern, shown in figure 6.11 (a). It seems that the thermal plumes do not arrive randomly, but arriving in groups with a certain frequency. The measured temperature fluctuation in the bulk is always skewed towards negative direction at all three windows, shown in figure 6.11 (c).

Figure 6.13 shows the diffusive heat flux, plotted in green and convective heat flux, plotted in red, calculated at the side windows. There is no difference between the profiles of diffusive heat flux measured at side window 1 and 2, but the convective heat flux measured at side window 1 is higher than the one measured at side window 2. As similar to the heat flux measured at the center line, the diffusive heat flux profile and the convective heat flux profiles cross at $z = 6.59$ mm (thermal BL thickness is $\delta_\theta = 6.32$ mm and $\delta_\theta = 6.55$ mm at window 1 and 2, respectively), which is also at the thermal BL region.

The total heat flux calculated by the measured velocity and temperature fluctuations at side windows is illustrated in figure 6.14. On average, the total heat flux measured at side window 1 is more than measured at side window 2, which means the heat flux is locally different from position to position. Recent DNS by Wagner et al. show that the BL thickness of both, the velocity and temperature field and thus the local heat flux vary significantly across the plate [92].

In summary, we found that at three various locations, the heat transportation inside the BL is dominated

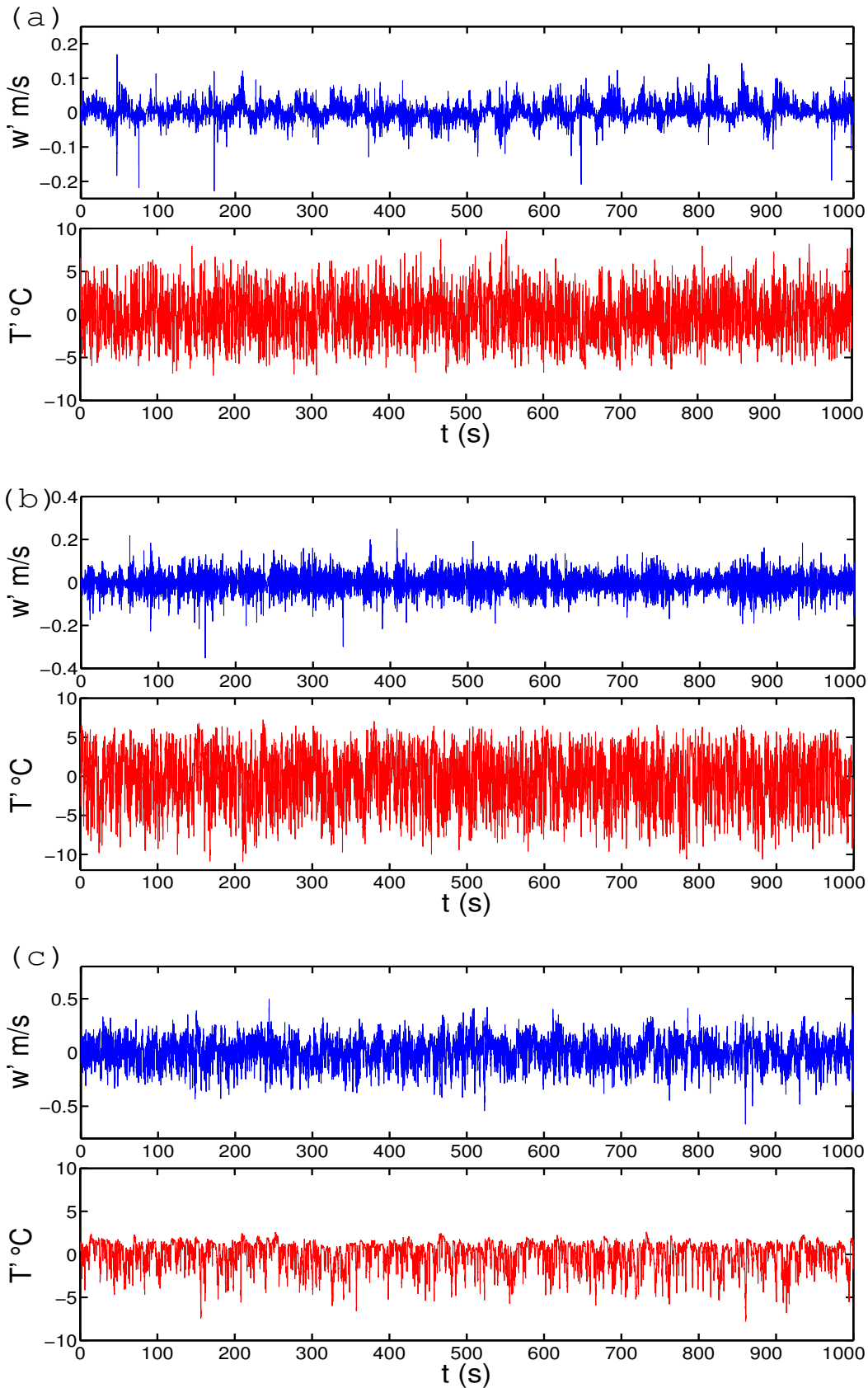


Figure 6.11: Snapshot of measured time series of the wall-normal velocity (blue) and the temperature (red) fluctuations, w' and T' . (a) at $z = 2.4$ mm; (b) at $z = 6.59$ mm; (c) at $z = 160$ mm at side window 1.

6.2 Simultaneous velocity and temperature profiles and their fluctuations out of the center line

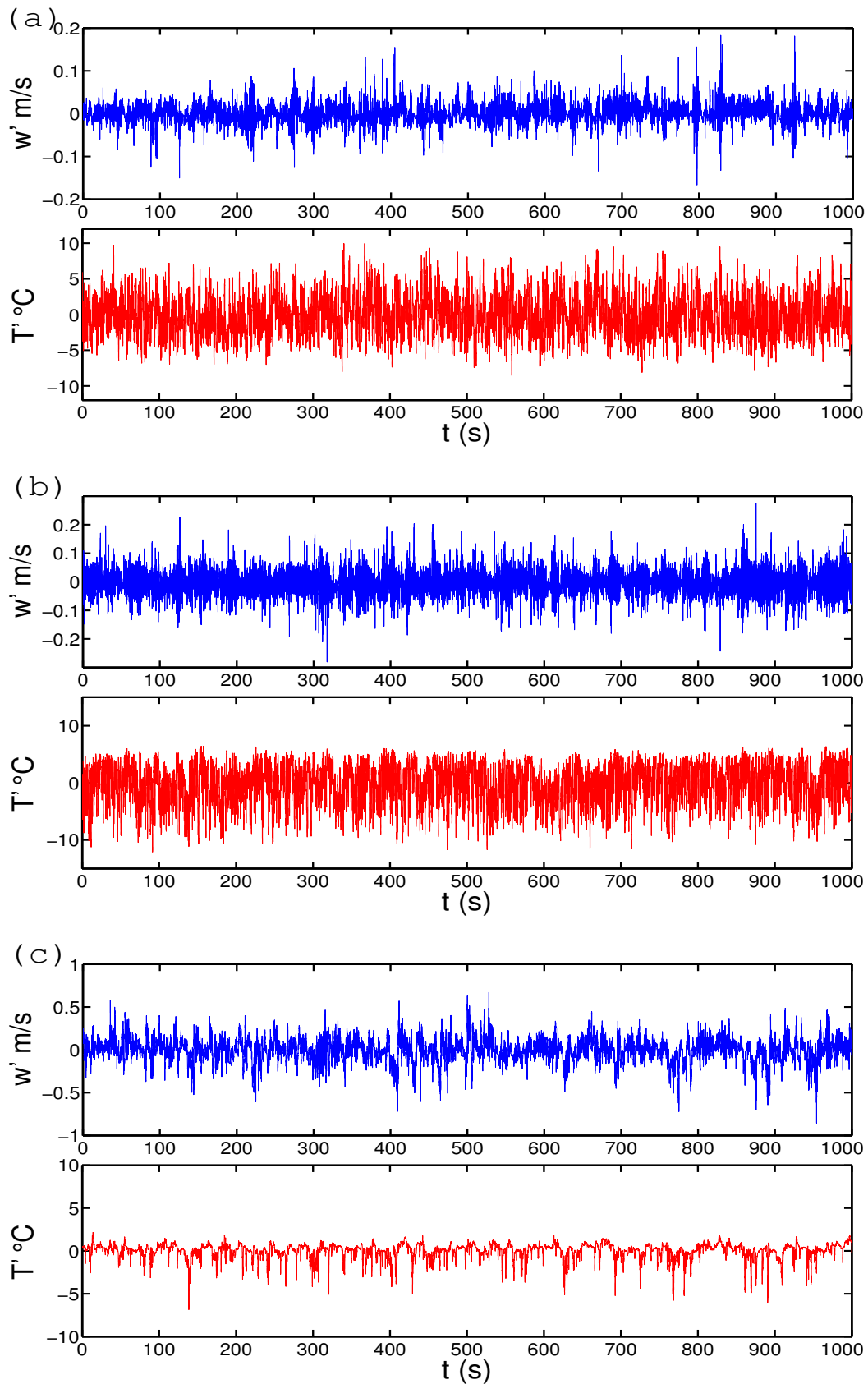


Figure 6.12: Snapshot of measured time series of the wall-normal velocity (blue) and the temperature (red) fluctuations, w' and T' . (a) at $z = 2.4$ mm; (b) at $z = 6.59$ mm; (c) at $z = 160$ mm at side window 2.

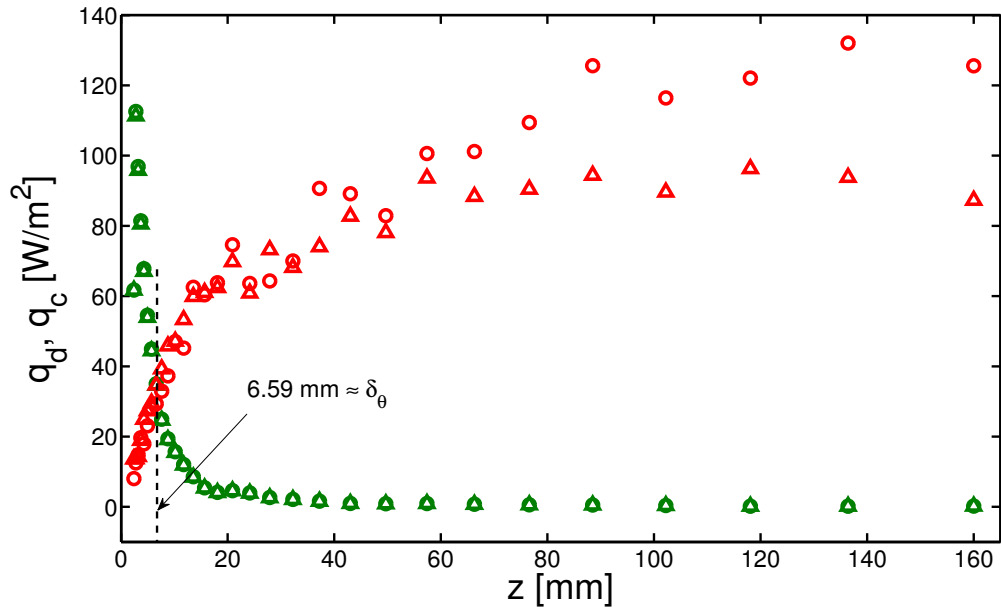


Figure 6.13: Profiles of diffusive heat flux \dot{q}_d (green) and convective heat flux \dot{q}_c (red) calculated from wall-normal velocity and temperature fluctuations at $Ra = 8.96 \times 10^{11}$, $\Gamma = 1.13$ and at side window 1 (open circles) and 2 (open triangles).

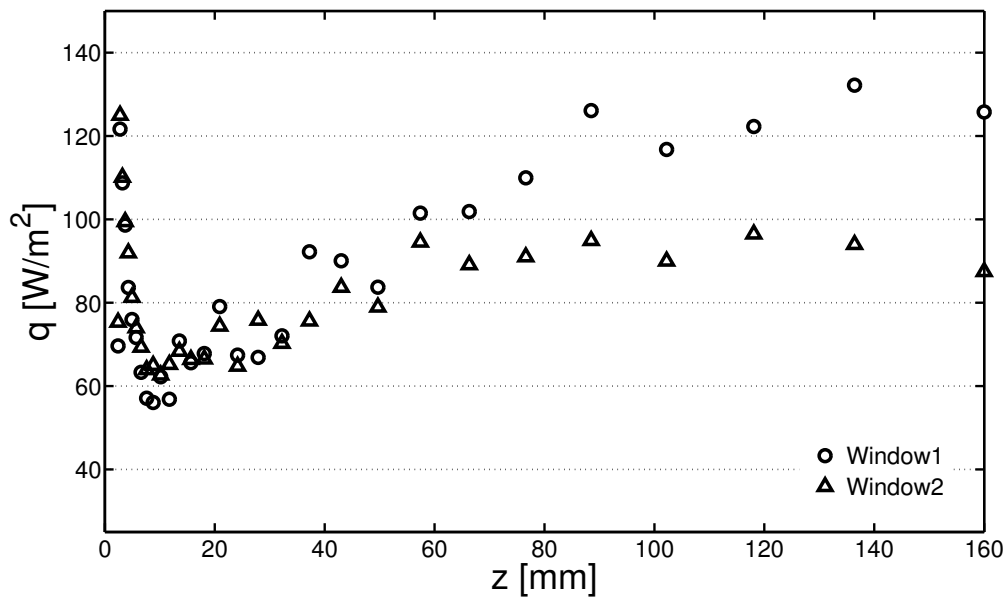


Figure 6.14: Profiles of total heat flux \dot{q} calculated from the velocity and temperature fluctuations at $Ra = 8.96 \times 10^{11}$ and $\Gamma = 1.13$ at side window 1 (open circles) and 2 (open triangles).

6.2 *Simultaneous velocity and temperature profiles and their fluctuations out of the center line*

by the diffusive heat flux and in the bulk it is dominated by the convective heat flux. The total heat flux is locally different.

7.1 Uncertainty analysis for the velocity data

The uncertainty in the velocity measurements is due to two fundamental types of errors: random or precision errors and fixed or bias errors. Figure 7.1 (a) shows up in a measurement scattering about the average value. These are usually caused by the characteristics of the measuring system in combination with changes in the quantity being measured [94]. Precision errors can be determined using standard statistical methods. Figure 7.1 (b) shows up in a measurement as a displacement between the average measured value and the average true value. Bias errors are considered to be constant for a given experiment and must be estimated [94]. In this chapter, our main intention is on bias error since no sample statistical methods exist to define them.

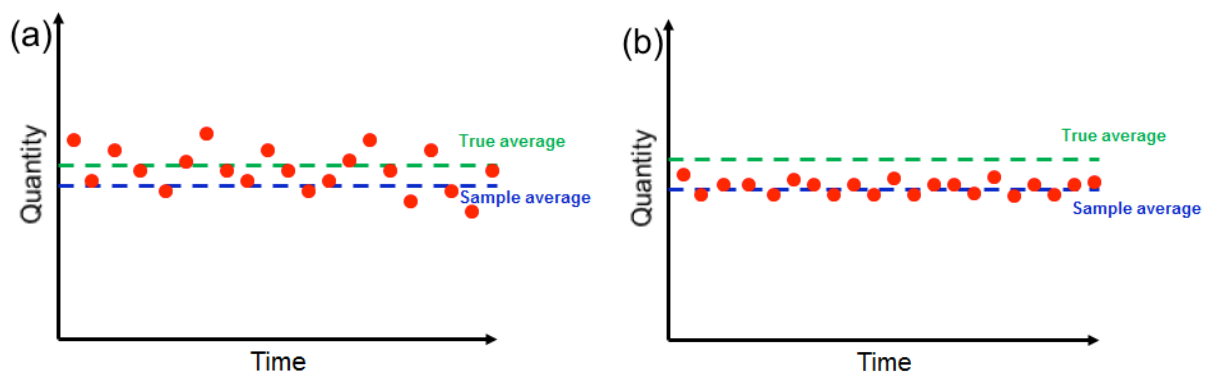


Figure 7.1: Two fundamental types of errors: (a) Random or precision errors, (b) Fixed or bias errors [93].

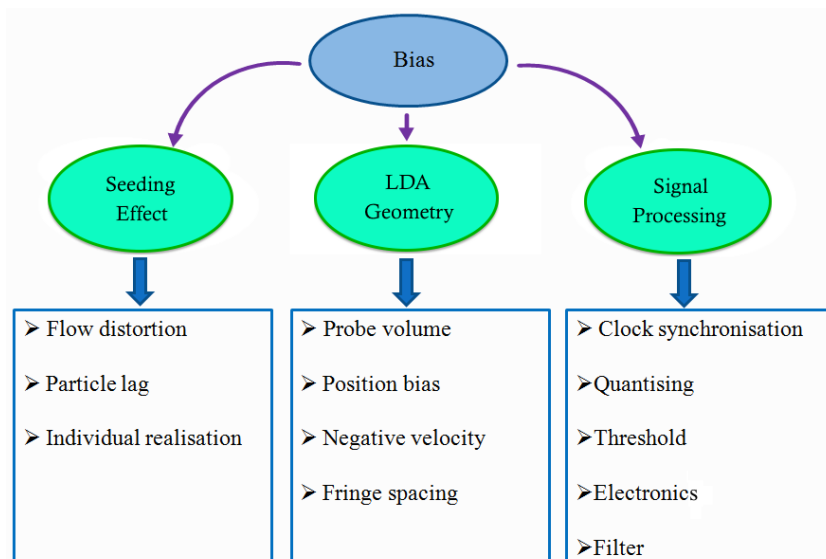


Figure 7.2: Bias sources [93]

Compared to other flow velocity measurement techniques, such as pitot probes, hot wire anemometry and ultrasonic velocimetry, the LDA technique is the most accurate method with a measurement error of the detected Doppler frequency in the range of $< 1\%$. In spite of the high accuracy given by the laser, seeding particle properties and statistics are the main source of measurement errors, such as the bias problem. The bias problem exists in all the turbulent flow measurements and is mainly the result of the seeding effect on the flow, specific geometry of the LDA probe alignment and LDA fringe pattern and the electronic effects associated with the configuration of the burst signal processors, [94]. An overview of the sources of bias is shown in figure 7.2 and described as follows:

1. Bias due to seeding effects:

Seeding effects can result in bias being introduced into the LDA velocity measurements through flow distortion, seed particle lag, and individual realization biases [94]. Flow distortion bias is typically caused by artificial seeding of a flow field which is negligible in BOI due to the small Stokes number (see chapter 4.1.2). Seed particle lag bias is the result of the inability of a seed particle to accurately follow the flow field which is minimal in BOI due to the low turbulent flow. In BOI, the individual realization bias can be assumed to be negligible since there is an equal probability of detecting a fast moving seed particle as there is of detecting a slow moving particle.

2. Bias due to the LDA geometry:

Bias arising from the specific geometry of the intersecting laser beams for the flow pattern can be cate-

gorized as follows [94]: Finite probe volume bias arises since the velocities are measured over a finite control volume diameter. In BOI, finite probe volume bias is negligible due to small velocity gradient. The position or orientation bias is considered negligible since the control volume was carefully aligned with the mean flow direction. The negative velocities introduced into the average velocity can be eliminated by the frequency shift. Fringe spacing uncertainty will be discussed in the next section.

3. Bias due to the burst signal processors:

Heyst [94] studied that clock synchronization bias is the result of the mismatch between the randomly occurring Doppler bursts and the start of the clock cycle. Quantizing bias arises from the determination of the frequency of the analog Doppler signal by the use of a digital reference clock. The quantizing bias resulting from the current configuration and the Fast Fourier Transform (FFT) algorithm is extremely small and thus are considered negligible. Electronic noise-induced bias occurs at low signal-to-noise ratios (SNR) and filter bias is caused by the improper setting of the cutoff frequency of pedestal filters, however, with the help of proper filter and threshold settings, the bias can be minimized.

Figure 7.3 presents several techniques to eliminate the velocity bias, but most of them fall into two general categories [95]: post-facto techniques and sampling methods. Find more details and calculations in the conference contribution [93].

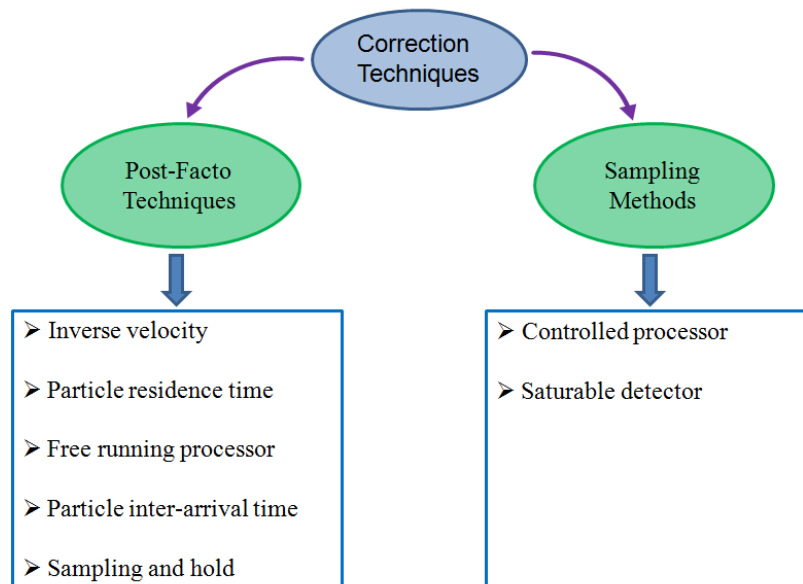


Figure 7.3: Bias error correction techniques [93]

In summary, the velocity bias errors due to fringe spacing and threshold limit are of $< 0.1\%$. The bias errors due to turbulent flow are of $< 0.2\%$, so we conclude that the LDA data including the digital post-processing is bias free.

7.2 Accuracy of the temperature data

Temperature measurement uncertainties, which are the variance from true temperature, could come from three sources. First, there is the self-heating effect of the thermistor probe. It has been demonstrated in section 4.3, the thermistor self-heating error can be avoid by using a lower measurement current than usual. Second, there is another uncertainty from the thermistor calibration and from the thermistor geometry.

The Steinhart-Hart equation is the most popular model used for thermistor resistance-temperature modeling, $T = (C_1 + C_2 \ln(R) + C_3 \ln(R)^3)^{-1} - 273.16$ K. Where T denotes the absolute temperature in Kelvin and R denotes the thermistor resistance in Ohms. The terms C_1 , C_2 , and C_3 are the Steinhart-Hart constants for the thermistor. We have calibrated the thermistor in an accurate closed temperature measurement chamber by more than three points with the RTD reference probe. The measurement uncertainty of the thermistor is specified with ± 0.02 K in the range between 0°C and 100°C . This uncertainty can be omitted, for the simultaneous velocity and temperature measurements, since we are only interested in the temperature fluctuations.

Regarding the geometry of the thermistor, if the connecting wires of the thermistor are not parallel to the measuring isothermal surface, they will induce an additional heat flux in the sensor body. The additional heat flux is driven by the strong thermal gradient of the surrounding fluid. This effect has been systematically studied by Kaiser [69]. All the temperature measurements in this work were applied with the improved alignment of connecting wires, namely the connecting wires were aligned parallel to the horizontal cooling plate. Under this circumstance according the error analysis, if the temperature gradient is about 9.85 K/mm, the thermistor has a 0.1% negligible small error. The maximum temperature gradient in all the temperature measurements of this work is about 4 K/mm, which means the error caused by the geometry of the thermistor is less than 0.1% . Even if the connecting wires were misaligned to 10° to the horizontal plate, the measurement error will not be larger than 0.83% .

8.1 Conclusion

For a better understanding of the heat transfer in thermal convection, the local field variables, particular within the BLs have been studied in detail. At two Rayleigh numbers, $Ra = 3 \times 10^9$ and $Ra = 3 \times 10^{10}$, the first highly resolved measurements of all three velocity components and the temperature have been carried out inside and outside of the BLs close to the cooling plate and compared with equivalent DNS data [1]. Furthermore, the first simultaneous velocity and temperature measurements inside and outside of the BLs at various positions at $Ra = 8.96 \times 10^{11}$ and $\Gamma = 1.13$ have been carried out. All velocity and temperature measurements have been done in the large-scale RB cell, “Barrel of Ilmenau” using both LDA and micro-thermistor technique, respectively.

In fact, the theoretical interpretation of experimental results and the quantitative prediction of thermal convection are still possible to a limited extent. The direct comparison of the local velocity and temperature data between experiment and numerical simulation would definitely help to compensate some knowledge deficit. In summary, the measured velocity data agrees very well with the DNS results while the temperature data slightly differs. The mean horizontal velocity as well as the mean of the wall-normal component are in excellent agreement. Both experimental and numerical mean profiles differ from the Blasius solution of a laminar non-isothermal shear layer. At the center line of the cylindrical convection cell, the mean of the wall-normal velocity component holds at zero over a long range of the wall distance z . However, this component strongly fluctuates, as strong as 80% of the horizontal velocity fluctuations. Out of the center, particularly at the areas where the plumes hit or leave the horizontal plates a non-zero mean wall-normal velocity has been detected. We also found that the viscous

8 Conclusion

BL thickness scales with Ra as $\delta_v \sim \text{Ra}^{-0.24}$, i.e., with the same exponent as predicted by Grossmann and Lohse [31]. In order to have a sufficiently long range in Ra we complemented our data with velocity data from previous experiments covering eventually Rayleigh numbers between $\text{Ra} = 10^9$ and $\text{Ra} = 10^{12}$. We also discussed the shear Reynolds number and its trend with growing Ra since this quantity is one of the potential indicators of a transition towards a turbulent BL. Up to the highest Ra, $\text{Ra} = 10^{12}$, it remains below the predicted transition limits $\text{Re}_{s,c} = 320$ [76] or $\text{Re}_{s,c} = 420$ [75].

The measured mean temperature profiles slightly differ from the numerical results. Particularly, the measured temperature gradients at the wall are significantly higher than those computed from the DNS. Furthermore, both measured profiles do not show the clear linear trend close to the wall as seen in the DNS data. These discrepancies exist, even though the measurements have been carried out very carefully and the used micro-thermistor probes have been calibrated precisely. One of the potential explanations might be the temperature dependence of the fluid properties, *e.g.* at $\Delta T = 20$ K, $\text{Ra} = 3 \times 10^{10}$, the heat conductivity λ varies by about 7.5% across the cell. According to Fourier's law of heat conduction, the temperature gradient $dT/dz|_{z=0} = -q_w/\lambda$, this variation causes the temperature gradients at the surface of the cooling plate or heating plate to differ by 7.5% as well. The temperature gradient $dT/dz|_{z=0}$ is linked to the local wall heat flux with $1/\lambda$ being the constant of proportionality. Assuming symmetry with respect to the local wall heat flux at the heating and the cooling plates, this results in a difference in the gradients by exactly this value. Thermal diffusivity κ and kinematic viscosity ν vary by even 15%, but the numerical simulation based on Boussinesq approximation does not take this into account and there is no summary about how this affects the local temperature profiles. The local thickness of the thermal BL at the center line is found to be scaled with respect to the Ra as $\delta_\theta \sim \text{Ra}^{-0.24}$, as well as being slightly different from the global prediction (0.25 for the exponent) in this range of Ra. The BL thickness is not a constant and depends on the different location at the plate and the specific moment in time.

We measured the velocity and temperature profiles at $\text{Ra} = 1.27 \times 10^9$, $\Gamma = 2.76$ at various locations as well. We observed that the convective flow does not have a uniform BL thickness distribution. It might be caused by the irregular elliptical flow pattern which does not fill out the whole cross section of the convection cell. The indications do not show a clear double-roll structure.

The simultaneous measurement of velocity and temperature fluctuations in a single point inside and outside the BL allows us to calculate the local convective heat flux. For the results of the simultaneous

velocity and temperature measurements at $Ra = 8.96 \times 10^{11}$ and $\Gamma = 1.13$, the directly measured mean wall-normal velocity at the center line still trends to zero, which agrees with the earlier 3D velocity measurement. The diffusive and convective heat flux and their sum have been calculated by the measured mean velocity and temperature and their fluctuations at various locations. We observed that the thermal plumes, rising up and falling down at the BL region, resulted in a skewed time series of the temperature fluctuation. We found that at all investigated locations the heat transport inside the BL is dominated by diffusion while in the bulk it is dominated by convection. The total heat flux differs with respect to the measurement position at the plate, the total heat flux measured at window 1 (down-welling plumes) is about 40% higher than measured at window 2 (up-welling plumes).

8.2 Outlook

The simultaneous velocity and temperature measurements are valuable for understanding the heat transport and for verifying the numerical simulation results and other predictions. In the future, we need to improve our measurement set-up to start measuring right from the vicinity of the cooling plate, since the possibility of the current measurement starts at $z = 2.4$ mm and thus some data points are missing inside the BL. The most ideal way would be to remove the mirror inside the convection cell, but to optimize the windows to guide LDA laser beams for measuring the wall-normal velocity directly at the intimate vicinity of the horizontal plate. For example, the glass window could include a special optical prism to reflect the LDA beams in horizontal direction. Another thought is that a faster (< 100 ms) and smaller (< 125 μm diameter) thermistor would be necessary for improving the resolution of the temperature data. Furthermore, we are interested in the directly measured heat flux at different Ra numbers and at various Γ , when the large single roll drops down into two or more small rolls. Moreover, another interest to be explored in the future, would be the PIV measurements of the dynamics of vortex structures in the near wall. The PIV measurements will give us an even deeper insight into the momentum and heat transport processes close to the plate surface.

- [1] SHI, N.; EMRAN, M. S. ; SCHUMACHER, J.: Boundary layer structure in turbulent Rayleigh-Bénard convection. *J. Fluid Mech.* 705 (2012), 5–33
- [2] KADANOFF, L. P.: Turbulent heat flow: Structures and scaling. *Phys. Today* 54 (2001), 34
- [3] AHLERS, G.; GROSSMAN, S. ; LOHSE, D.: Heat transfer and large-scale dynamics in turbulent Rayleigh-Bénard convection. *Rev. Mod. Phys.* 81 (2009), 503–537
- [4] DU PUIITS, R.; RESAGK, C.; TILGNER, A.; BUSSE, F. H. ; THESS, A.: Structure of thermal boundary layers in turbulent Rayleigh-Bénard convection. *J. Fluid Mech.* 572 (2007), 231–254
- [5] SUN, C.; XIA, K.-Q. ; TONG, P.: Three-dimensional flow structures and dynamics of turbulent thermal convection in a cylindrical cell. *Phys. Rev. E* 72 (2005), 026302
- [6] SHEN, Y.; XIA, K. Q. ; TONG, P.: Measured local-velocity fluctuations in turbulent convection. *Phys. Rev. Lett.* 75 (1995), 437–440
- [7] XIN, Y. B.; XIA, K. Q. ; TONG, P.: Measured velocity boundary layers in turbulent convection. *Phys. Rev. Lett.* 77 (1996), 1266
- [8] XIN, Y. B.; XIA, K. Q.: Boundary layer length scales in convective turbulence. *Phys. Rev. E* 56 (1997), 3010–3015
- [9] LUI, S. L.; XIA, K. Q.: Spatial structure of the thermal boundary layer in turbulent convection. *Phys. Rev. E.* 57 (1998), 5494
- [10] CASTAING, B.; GUNARATNE, G.; HESLOT, F.; KADANOFF, L.; LIBCHABER, A.; THOMAE, S.; WU, X. Z.; ZALESKI, S. ; ZANETTI, G. M.: Scaling of hard thermal turbulence in Rayleigh-Bénard convection. *J. Fluid Mech.* 204 (1989), 1–30

Bibliography

- [11] CHAVANNE, X.; CHILLÀ, F.; CASTAING, B.; HEBRAL, B.; CHABAUD, B. ; CHAUSSY, J.: Observation of the ultimate regime in Rayleigh-Bénard convection. *Phys. Rev. Lett.* 19 (1997), 3648
- [12] NIEMELA, J. J.; SKRBEK, L.; SREENIVASAN, K. R. ; DONNELLY, R. J.: Turbulent convection at very high Rayleigh numbers. *Nature* 404 (2000), 837–840
- [13] FUNFSCHILLING, D.; BODENSCHATZ, E. ; AHLERS, G.: Search for the “ultimate state” in turbulent Rayleigh-Bénard convection. *Phys. Rev. Lett.* 103 (2009), 014503
- [14] DU PUIITS, R.; RESAGK, C. ; THESS, A.: Thermal boundary layers in turbulent Rayleigh-Bénard convection at aspect ratios between 1 and 9. *New J. Phys.* 15 (2013), 013040
- [15] RESAGK, C.; DU PUIITS, R.; THESS, A.; DOLZHANSKY, F. V.; GROSSMANN, S.; ARAUJO, F. F. ; LOHSE, D.: Oscillations of the large scale wind in turbulent thermal convection. *Phys. Fluids* 18 (2006), 095105
- [16] DU PUIITS, R.; RILK, J.; RESAGK, C. ; THESS, A.: Boundary layers in turbulent Rayleigh-Bénard convection in air. *arxiv.org* (2012), arXiv:1209.6201
- [17] DU PUIITS, R.; RESAGK, C. ; THESS, A.: Mean velocity profile in confined turbulent convection. *Phys. Rev. Lett.* 99 (2007), 234504
- [18] DU PUIITS, R.; RESAGK, C. ; THESS, A.: Breakdown of wind in turbulent thermal convection. *Phys. Rev. E* 75 (2007), 016302
- [19] DU PUIITS, R.; RESAGK, C. ; THESS, A.: Structure of viscous boundary layers in turbulent Rayleigh-Bénard convection. *Phys. Rev. E* 80 (2009), 036318
- [20] LI, L.; SHI, N.; DU PUIITS, R.; RESAGK, C.; SCHUMACHER, J. ; THESS, A.: Boundary layer analysis in turbulent Rayleigh-Bénard convection in air: Experiment versus simulation. *Phys. Rev. E* 86 (2012), 026315
- [21] GRIFFITHS, E.; DAVIS, A. H.: The transmission of heat by radiation and convection. *DSIR Food Investigation Board Special Report Bd.* 9, (1922)
- [22] MALKUS, W. V. R.: The heat transfer and spectrum of thermal turbulence. *Proc. R. Soc. London A* 225 (1954), 196–212
- [23] DEARDORFF, J. W.; WILLIS, G. E.: Investigation of turbulent thermal convection between horizontal plates. *J. Fluid Mech.* 28 (1976), 675–704

- [24] KRISHNAMURTI, R.: One the transition to turbulent convection. Part I. The transition from two- to three-dimensional flow. *J. Fluid Mech.* 42 (1970), 295–307
- [25] BROWN, W. S.: Heat-flux transitions at low Rayleigh number. *J. Fluid Mech.* 60 (1973), 539–559
- [26] BUSSE, F. H.: On the stability of two-dimensional convection in a layer heated from below. *J. Math. Phys.* 46 (1967), 140–179
- [27] FITZJARRALD, D. E.: An experimental study of turbulent convection in air. *J. Fluid Mech.* 73 (1976), 693
- [28] SANO, M.; WU, X. Z. ; LIBCHABER, A.: Turbulence in helium-gas free convection. *Phys. Rev. A* 40 (1989), 6421
- [29] CHAVANNE, X.; CHILLÀ, F.; CHABAUD, B.; CASTAING, B. ; HÉBRAL, B.: Turbulent Rayleigh-Bénard convection in gaseous and liquid He. *Phys. Fluids* 13 (2001), 1300–1320
- [30] NIEMELA, J. J.; SREENIVASAN, K. R.: Confined turbulent convection. *J. Fluid Mech.* 481 (2003), 355–384
- [31] GROSSMANN, S.; LOHSE, D.: Scaling in thermal convection: a unifying theory. *J. Fluid Mech.* 407 (2000), 27–56
- [32] GROSSMANN, S.; LOHSE, D.: Prandtl and Rayleigh number dependence of the Reynolds number in turbulent thermal convection. *Phys. Rev. E* 66 (2002), 016305
- [33] GROSSMAN, S.; LOHSE, D.: On geometry effects in Rayleigh-Bénard convection. *J. Fluid Mech.* 486 (2003), 105–114
- [34] KRAICHNAN, R. H.: Turbulent thermal convection at arbitrary Prandtl number. *Phys. Fluids* 5 (1962), 1374–1389
- [35] CHILLÀ, F.; RASTELLO, M.; CHAUMAT, S. ; CASTAING, B.: Ultimate regime in Rayleigh-Bénard convection: The role of plates. *Phys. Fluids* 16 (2004), 2452–2456
- [36] GARON, A. M.; GOLDSTEIN, R. J.: Velocity and heat transfer measurements in thermal convection. *Phys. Fluids* 16 (1973), 1818–1825
- [37] TANAKA, H.; MIYATA, H.: Turbulent natural convection in a horizontal water layer heated from below. *Int. J. Heat Mass Transfer.* 23 (1980), 1273

Bibliography

- [38] TILGNER, A.; BELMONTE, A. ; LIBCHABER, A.: Temperature and velocity profiles in turbulent convection in water. *Phys. Rev. E* 47 (1993), R2253
- [39] BELMONTE, A.; TILGNER, A. ; LIBCHABER, A.: Temperature and velocity boundary layer in turbulent convection. *Phys. Rev. E* 50 (1994), 269–279
- [40] CHILLÀ, F.; CILIBERTO, S.; INNOCENTI, C. ; PAMPALONI, E.: Boundary layer and scaling properties in turbulent thermal convection. *Nuovo Cimento* 15 (1993), 1229–1249
- [41] QIU, X. L.; XIA, K. Q.: Viscous boundary layers at the sidewall of a convection cell. *Phys. Rev. E* 58 (1998), 486–491
- [42] QIU, X. L.; TONG, P.: Large scale velocity structures in turbulent thermal convection. *Phys. Rev. E* 64 (2001), 036304
- [43] SUN, C.; CHEUNG, Y. H. ; XIA, K. Q.: Experimental studies of the viscous boundary layer properties in turbulent Rayleigh-Bénard convection. *J. Fluid Mech.* 605 (2008), 79
- [44] SHRAIMAN, B. I.; SIGGIA, E. D.: Heat transport in high-Rayleigh-number convection. *Phys. Rev. A* 42 (1990), 3650–3653
- [45] SIGGIA, E.D.: High Rayleigh number convection. *Annu. Rev. Fluid Mech.* 26 (1994), 137–168
- [46] GROSSMANN, S.; LOHSE, D.: Fluctuations in turbulent Rayleigh-Bénard convection: The role of plumes. *Phys. Fluids* 16 (2004), 4462–4472
- [47] SCHLICHTING, H.; GERSTEN, K.: *Boundary Layer Theory*. Springer, (2004)
- [48] ZHOU, Q.; XIA, K. Q.: Measured instantaneous viscous boundary layer in turbulent Rayleigh-Bénard convection. *Phys. Rev. Lett.* 104 (2010), 104301
- [49] ZHOU, Q.; STEVENS, R. J. A. M.; SUGIYAMA, K.; GROSSMANN, S.; LOHSE, D. ; XIA, K. Q.: Prandtl-Blasius temperature and velocity boundary layer profiles in turbulent Rayleigh-Bénard convection. *J. Fluid Mech.* 664 (2010), 297–312
- [50] STEVENS, R. J. A. M.; ZHOU, Q.; GROSSMANN, S.; VERZICCO, R.; XIA, K. Q. ; LOHSE, D.: Thermal boundary layer profiles in turbulent Rayleigh-Bénard convection in a cylindrical sample. *Phys. Rev. E* 85 (2012), 027301
- [51] SCHEEL, J. D.; KIM, E. ; WHITE, K. R.: Thermal and viscous boundary layers in turbulent Rayleigh-Bénard convection. *J. Fluid Mech.* 711 (2012), 281–305

- [52] SHANG, X. D.; QIU, X. L.; TONG, P. ; XIA, K. Q.: Measured local heat transport in turbulent Rayleigh-Bénard convection. *Phys. Rev. Lett.* 90 (2003), Nr. 7, 074501
- [53] SHANG, X. D.; QIU, X. L.; TONG, P. ; XIA, K. Q.: Measurements of the local convective heat flux in turbulent Rayleigh-Bénard convection. *Phys. Rev. E* 70 (2004), 026308
- [54] QIU, X. L.; SHANG, X. D.; TONG, P. ; XIA, K. Q.: Velocity oscillations in turbulent Rayleigh-Bénard convection. *Phys. Fluids* 16 (2004), 412–423
- [55] VERZICCO, R.; CAMUSSI, R.: Prandtl number effects in convective turbulence. *J. Fluid Mech.* 383 (1999), 55–73
- [56] VILLERMAUX, E.: Memory-induced low frequency oscillations in closed convection boxes. *Phys. Rev. Lett.* 75 (1995), Nr. 25, 4618–4621
- [57] SREENIVASAN, K. R.; BERSHADSKII, A. ; NIEMELA, J. J.: Mean wind and its reversal in thermal convection. *Phys. Rev. E* 65 (2002), 056306
- [58] NIEMELA, J. J.; SKRBEK, L.; SREENIVASAN, K. R. ; DONNELLY, R. J.: The wind in confined thermal convection. *J. Fluid Mech.* 449 (2001), 169–178
- [59] BROWN, E.; AHLERS, G.: Rotations and cessations of the large-scale circulations in turbulent Rayleigh-Bénard convection. *J. Fluid Mech.* 568 (2006), 351–386
- [60] BROWN, E.; NIKOLENKO, A. ; AHLERS, G.: Reorientation of the large-scale circulation in turbulent Rayleigh-Bénard convection. *Phys. Rev. Lett.* 95 (2005), 084503
- [61] BLASIUS, H.: Grenzsichten in Flüssigkeiten mit kleiner Reibung. *Z. Math. Phys.* 56 (1908), 1–37
- [62] DU PUIITS, R.: *Wärmetransport in turbulenter Konvektionsströmung*, TU Ilmenau, Habilitationsschrift, (2008)
- [63] YEH, Y.; CUMMINS, H. Z.: Localized fluid flow measurements with a He-Ne laser spectrometer. *Appl. Phys. Lett.* (1964), 176–179
- [64] LEHMANN, B.: Geschwindigkeitsmessung mit Laser-Doppler-Anemometer Verfahren. *Wiss. Berichte AEG-Telefunken* (1968), 141–145
- [65] VON STEIN, H. D.; PFEIFER, H. J.: A Doppler difference method for velocity measurements. *Metrologia* (1969), 59–61

Bibliography

- [66] *Dantec dynamics education presentation*. Dantec Dynamics, (2004)
- [67] *Bedienungsanleitung Flüssigkeitszerstäuber AGF 10.0*. Palas Partikel- und Lasermeßtechnik, (1996)
- [68] BAKER, B.: Temperature sensing technologies. (1998)
- [69] KAISER, R.; DU PUIITS, R.: Error estimation of temperature measurements in non-isothermal shear layers. *Exp. Fluids* 53 (2012), 137–143
- [70] KAISER, R.: *Geschwindigkeitsmessung in turbulenter Rayleigh-Bénard Konvektion*, TU Ilmenau, Diplomarbeit, (2010)
- [71] *Dantec User's Guide*. Dantec Dynamics, (2006)
- [72] INCEROPERA, P. F.; DEWITT, P. D.: *Fundamentals of heat and mass transfer*. John Wiley and Sons, (1996)
- [73] POHLHAUSEN, E.; ANGEW, Z.: Der Wärmeaustausch zwischen festen Körpern und Flüssigkeiten mit kleiner Reibung und kleiner Wärmeleitung. *Math. Mech.* 1 (1921), 115–121
- [74] POPE, S. B.: *Turbulent flows*. Cambridge University Press, (2010)
- [75] LANDAU, L. D.; LIFSCHITZ, E. M.: *Fluid Mechanics*. Pergamon Press, (1987)
- [76] PRESTON, J. H.: The minimum reynolds number for a turbulent boundary layer and the selection of a transition device. *J. Fluid Mech.* 3 (1958), 373–384
- [77] HE, X. Z.; FUNFSCHILLING, D.; NOBACH, H.; BODENSCHATZ, E. ; AHLERS, G.: Transition to the ultimate state of turbulent Rayleigh-Bénard convection. *Phys. Rev. Lett.* 108 (2012), 024502
- [78] LUMLEY, J. L.: Computational modeling of turbulent flows. *Advances in Applied Mechanics* 18 (1978), 123–176
- [79] HIRSCH, H.: *Isotropie/Anisotropie in turbulenter Rayleigh-Bénard Konvektion*, TU Ilmenau, Master Projektseminar, (2013)
- [80] BANERJEE, S.; KRAHL, R.; DURST, F. ; ZENGER, CH.: Presentation of anisotropy properties of turbulence, invariants versus eigenvalue approaches. *J. Turbulence* 8 (2007), 32
- [81] XU, X. C.; BAJAJ, K. M. S. ; AHLERS, G.: Heat transport in turbulent Rayleigh-Bénard convection. *Phys. Rev. Lett.* 84 (2000), 4357–4360

- [82] FLEISCHER, A. S.; GOLDSTEIN, R. J.: High-Rayleigh-number convection of pressurized gases in a horizontal enclosure. *J. Fluid Mech.* 469 (2002), 1–12
- [83] CHEUNG, Y. H.: Aspect-ratio dependence of the Nusselt number and boundary layer properties in Rayleigh-Bénard turbulent convection. *MPhil thesis* (2004), The Chinese University of Hong Kong
- [84] NIKOLAENKO, A.; BROWN, E.; FUNFSCHILLING, D. ; AHLERS, G.: Heat transport by turbulent Rayleigh-Bénard convection in cylindrical cells with aspect ratio one and less. *J. Fluid Mech.* 523 (2005), 251–260
- [85] FUNFSCHILLING, D.; BROWN, E.; NIKOLAENKO, A. ; AHLERS, G.: Heat transport by turbulent Rayleigh-Bénard convection in cylindrical samples with aspect ratio one and larger. *J. Fluid Mech.* 536 (2005), 145–154
- [86] NIEMELA, J. J.; SREENIVASAN, K. R.: Turbulent convection at high Rayleigh numbers and aspect ratio 4. *J. Fluid Mech.* 557 (2006), 411–422.
- [87] ROCHE, P. E.; GAUTHIER, F.; KAISER, R. ; SALORT, J.: On the triggering of the ultimate regime of convection. *New J. Phys.* 12 (2010), 085014
- [88] XIA, K. Q.; SUN, C. ; CHEUNG, Y. H.: Large-scale velocity structures in turbulent thermal convection with widely varying aspect ratio. *Proc. 14th Int. Symp. on Applications of Laser Techniques to Fluid Mechanics, Lisbon, Portugal*, (2008)
- [89] BAILON-CUBA, J.; EMRAN, M. S. ; SCHUMACHER, J.: Aspect ratio dependence of heat transfer and large-scale flow in turbulent convection. *J. Fluid Mech.* 655 (2010), 152–173
- [90] LOBUTOVA, E.; RESAGK, C. ; PUTZE, T.: Investigation of large-scale circulations in room air flows using three-dimensional particle tracking velocimetry. *Building and Environment* 45 (2010), 1653–1662
- [91] TENNEKES, H.; LUMLEY, J. L.: *A first course in turbulence*. MIT Press, (1972)
- [92] WAGNER, S.; SHISHKINA, O. ; WAGNER, C.: Boundary layers and wind in cylindrical Rayleigh-Bénard cells. *J. Fluid Mech.* 697 (2012), 336–366
- [93] AGRAWAL, Y. K.; LI, L.; DU PUIITS, R. ; RESAGK, C.: Velocity bias in turbulent boundary layer flows measured with laser Doppler anemometry. *Proceedings of the Thirty Ninth National Conference on Fluid Mechanics and Fluid Power, Gujarat, India*, (2012)

Bibliography

- [94] HEYST, W. J. V.: *The evolution of a turbulent isothermal jet in a uniform turbulent external coflow*, University of Waterloo, PhD thesis, (1997)
- [95] HERRIN, J. L.; DUTTON, J. C.: An investigation of LDV velocity bias correction techniques for high speed separated flows. *Exp. Fluid* 14 (1997), 354–363

LIST OF FIGURES

| | | |
|-----|--|----|
| 2.1 | The large-scale circulation with a typical mean flow, which is maintained by the up- and down-welling plumes detaching permanently from the BLs. | 14 |
| 2.2 | Structure of the boundary layer flow over a flat plate. | 15 |
| 3.1 | Sketch of “Barrel of Ilmenau” with the inset cell of 2.5 m height and 2.5 m diameter. In this work we will take measurements at the central window (the center line) and the side windows 1, 2 and 3. | 17 |
| 3.2 | Construction of cooling plate of the BOI, with 16 separate segments (on the left) and the cross section of an individual segment (on the right) [62]. | 19 |
| 3.3 | Temperature distribution at the surface of the heating plate (a) and the cooling plate (b) at $T_h - T_c = 35.2$ K, $\Gamma = 2.75$ and $Ra = 5.2 \times 10^{10}$. The plots show the relative deviation $\Delta T_h = 100 [T_h(x, y) - T_h] / [T_h - T_c]$ and $\Delta T_c = 100 [T_c - T_c(x, y)] / [T_h - T_c]$ in percent of the total temperature drop between the plates. The crosses indicate the position of internal temperature sensors. The radial temperature distribution at each segment is a projection of the measured distribution along the horizontal line whereas the angular distributed temperature sensors are used as basic values. Figure taken from [14]. | 20 |
| 3.4 | Accessible parameter range in Ra versus Γ for the Barrel of Ilmenau (green), and the inset cell (red). The accessible range of the direct numerical simulation (DNS) is given in blue. The yellow dots mark the parameter sets (Ra, Γ) at which the measurements were compared directly with the results from the DNS [1]. | 21 |
| 4.1 | LDA principle and configuration of transmitter and receiver [66]. | 24 |

| | | |
|------|---|----|
| 4.2 | Three-dimensional LDA measurement volume in the intersection point of two laser beams. | 25 |
| 4.3 | Number distribution of DEHS droplets generated by AGF 2.0 at three different volume flows. [67] | 26 |
| 4.4 | Overview of the AGF systems. * applied for DEHS; ** test rig version; *** average number diameter [67] | 27 |
| 4.5 | Figure (a) shows the theoretical possibilities how one can align the measurement volume. At the BOI, there is no access for guiding the laser through the side-wall. Figure (b) shows the vertical alignment for the BOI with two different front lenses. The optimized measurement volume is guided through the window at the cooling plate with very short focal length of 160 mm. | 28 |
| 4.6 | Set-up of the 3D laser Doppler anemometry measurement using two probes, which are mounted on the traverse system above the cooling plate. u , v and w are the desired velocity components in the Cartesian coordinate system, δ illustrates the thickness of the BL inside the convection cell. | 29 |
| 4.7 | Stability test results by the “rotating wire” laser beam diagnostic method. The three colored curves are the three pairs of beams. The peak of the curves denote the maximum intensity of the Gaussian beam intensity distribution. (a) Principle: rotating wire with given frequency is cutting the LDA measurement volume and scanning the intensity distribution of each beam pair. (b) Well aligned measurement volume with all the maximum intensity in one vertical line. (c) De-adjusted measurement volume shows different peak positions after one hour traversing. | 30 |
| 4.8 | (a) Photograph of the laser beam diagnostic system Coherent LaserCam-HR. (b) Example of the intensity distribution of the LDA laser beam in the center of the measurement volume (focal point), screen shot of the BeamView USB Analyzer Software. | 31 |
| 4.9 | Temperature measurement set-up: Schematic of the thermistor probe performed through the central window (Figure 3.1) and a photograph of the sensor tip with connecting wires. | 34 |
| 4.10 | Simultaneous velocity and temperature measurement set-up: The sketch on the left shows the set-up of the joint measurement of wall-normal velocity and temperature through one access, a small window embedded in the cooling plate. The alignment of the thermistor and LDA measurement volume was fixed in the direction of the wind. The LDA probe and thermistor support are mounted together on a traverse system, which can be moved up and down precisely in 0.01 mm per step. The figure on the right shows a photograph of the dielectric mirror and the thermistor probe. | 35 |

| | | |
|------|--|----|
| 4.11 | Illustration of the flow disturbance from the thermistor | 36 |
| 4.12 | On the left side, the top-view of the set-up shows the horizontal displacement of $300 \mu\text{m}$ between the thermistor probe and the LDA measurement volume, which is necessary to minimize the heating of the thermistor by the LDA laser light. On the right side, the front-view shows the additional vertical displacement in order to prevent the measurement of wall-normal velocity from the influence of the flow around the thermistor and the connecting wires. | 37 |
| 4.13 | LDA block diagram of data acquirement and post-processing procedure. | 38 |
| 4.14 | Orientation of the horizontal velocity vector. (a) Instantaneous angle of the vector from experiment and (b) DNS data [1], taken at the center line. The time axis from the DNS has been recalculated to the experimental ones. Figure is taken from Ref. [20]. | 40 |
| 5.1 | Profiles of the mean horizontal velocity (a,b) and the standard deviation (c,d) measured in the experiment (closed circles) and obtained from the DNS (open circles) [1] at $\text{Ra} = 3 \times 10^9$ (a,c) and $\text{Ra} = 3 \times 10^{10}$ (b,d). The dashed lines in (a) and (b) represent the velocity field of a laminar flat plate BL according to Blasius [47]. The insets of (a) and (b) show the entire mean velocity profile in logarithmic scale and the inset of (c) and (d) show the near-wall region of the BL fluctuations. | 44 |
| 5.2 | Profiles of the mean wall-normal velocity (a,b) and the standard deviation (c,d) measured in the experiment (closed circles) and obtained from the DNS (open circles) [1] at $\text{Ra} = 3 \times 10^9$ (a,c) and $\text{Ra} = 3 \times 10^{10}$ (b,d). The insets show the near-wall region of the BL. | 45 |
| 5.3 | Profiles of the mean temperature (a,b) and the standard deviation (c,d) measured in the experiment (closed circles) [14] and obtained from the DNS (open circles) [1] at $\text{Ra} = 3 \times 10^9$ (a,c) and $\text{Ra} = 3 \times 10^{10}$ (b,d). The Pohlhausen solution is plotted on top of the mean temperature profile. The insets show the near-wall region of the BL. Here, ϑ_b and ϑ_{cp} denote the mean bulk temperature and the surface temperature of the cooling plate. | 47 |
| 5.4 | Displacement thickness of the viscous (a) and the thermal (b) BLs versus Ra . Experimental results (including earlier measurements data, see in table 5.1 and 5.2) are displayed as closed symbols, DNS data points are open symbols [1]. The solid lines in each of the graphs correspond to power laws $\delta_{v,d}/H = 0.66 \text{Ra}^{-0.24}$ and $\delta_{\theta,d}/H = 0.76 \text{Ra}^{-0.24}$, respectively. The inset in the left diagram shows the principle of displacement thickness definition. | 49 |

List of Figures

| | | |
|------|---|----|
| 5.5 | Thickness of the viscous (a) and the thermal (b) BLs versus Ra according to the slope method. Experimental results (including earlier measurements data, see in table 5.1 and 5.2) are displayed as closed symbols, DNS data points are open symbols [1]. The solid lines in each of the graphs correspond to power laws $\delta_{v,s}/H = 0.90 \text{ Ra}^{-0.24}$ and $\delta_{\theta,s}/H = 0.42 \text{ Ra}^{-0.24}$, respectively. The inset in the left diagram shows the principle of slope method. | 50 |
| 5.6 | Shear Reynolds number Re_s versus Ra from experiment (closed circles) and DNS (open circles) [1]. The solid line is the fit to all data. | 54 |
| 5.7 | Mean horizontal velocity profiles at side window 1, 2 and 3, are located at $r = 0.88 R$ and $\varphi = 0, \pi$ and $3\pi/2$ of the corresponding DNS model [1]. (a) Profiles of the measured data at $\text{Ra} = 2.88 \times 10^{10}$, at window 1 (circle), window 2 (triangle) and window 3 (star). (b) Profiles of the DNS data at $\text{Ra} = 3 \times 10^{10}$ at array 1 (circle), array 2 (triangle) and array 3 (star). The three locations are shown in the inset with reference to the mean flow. | 55 |
| 5.8 | Mean wall-normal velocity profiles at side window 1, 2 and 3. (a) Profiles of the measured data at $\text{Ra} = 2.88 \times 10^{10}$, at window 1 (circle), window 2 (triangle) and window 3 (star). There is a clear pair of up-welling and down-welling mean velocities. (b) Profiles of the numerical data [1] at $\text{Ra} = 3 \times 10^{10}$ at array 1 (circle), array 2 (triangle) and array 3 (star). | 56 |
| 5.9 | Anisotropy invariant map with calculated data based on the 3D velocity data measured from the BOI at different locations, at the center line (empty square), at side window 1 (asterisk), at side window 2 (empty triangle) and at side window 3 (empty circle) . . . | 58 |
| 5.10 | Sketches of hypothetic flow pattern transfers from $\Gamma = 1$ (left) to $\Gamma = 1.89$ (right) . . . | 58 |
| 5.11 | Profiles of the mean horizontal velocity (a) and the mean wall-normal velocity (b) measured at the center of the cooling plate at $\text{Ra} = 1.27 \times 10^9$, $\Gamma = 2.76$. The dashed line on top of the mean horizontal velocity is the Blasius profile. The insets shows the entire mean velocity profiles in logarithmic scale. | 59 |
| 5.12 | Profiles of the mean horizontal (a) and the mean wall-normal velocity fluctuations (b) measured at the center of the cooling plate at $\text{Ra} = 1.27 \times 10^9$, $\Gamma = 2.76$, plotted in linear scale. The insets are the entire profile plotted in logarithmic scale. | 60 |

- 5.13 Profiles of the mean temperature (a) and its fluctuations (b) measured at the center line of the cooling plate at $Ra = 1.27 \times 10^9$ ($\Delta T = 20$ K), $\Gamma = 2.76$ [14], plotted in logarithmic scale. Here, ϑ_b and ϑ_{cp} denote the mean bulk temperature and the surface temperature of the cooling plate. Pohlhausen solution is plotted on top of the mean temperature profile at $\Gamma = 2.76$. The inset is the linear plot of the vicinity data of the cooling plate, which shows the gradients of mean temperature profiles, at $Ra = 3 \times 10^9$ ($\Delta T = 2.4$ K), $\Gamma = 1$ (full circle), at $Ra = 1.27 \times 10^9$ ($\Delta T = 20$ K), $\Gamma = 2.76$ (asterisk). 61
- 5.14 Mean horizontal (a) and wall-normal (b) velocity profiles measured at side window 1, 2 and 3, which are located at $r = 0.88 R$ and $\varphi = 0, \pi$ and $3\pi/2$, see in Fig. 3.1. All profiles measured at $Ra = 1.27 \times 10^9$, $\Gamma = 2.76$, at window 1 (circle), window 2 (triangle) and window 3 (star), plotted in logarithmic scale. 61
- 5.15 2D plot of reconstructed long-term (over 60 min) 3D trajectory representing the transition between large single-roll and small single-roll in the whole cross section of the convective cell (dotted) and a small single-roll in the half cross section of the cell (solid line) at aspect ratio $\Gamma = 2$ and $Ra=1.3 \times 10^{11}$ [90]. 62
- 5.16 Profiles of the mean temperature (a) and its fluctuations (b) measured at side window 1, 2 and 3, at $Ra = 1.27 \times 10^9$, $\Gamma = 2.76$ [14], plotted in logarithmic scale. Here, ϑ_b and ϑ_{cp} denote the mean bulk temperature and the surface temperature of the cooling plate. 62
- 6.1 Time series of the main wind direction in the BOI. The inset shows the LSC in RB cell. The red line denotes the 90 degree direction of the locked orientation of the LSC. . . . 66
- 6.2 Measured wall-normal velocity profiles at $Ra = 8.96 \times 10^{11}$, $\Gamma = 1.13$ at the center line plotted in logarithmic scale. (a) Profile of the mean wall-normal velocity normalized by the maximum mean horizontal velocity. (b) Profile of the mean wall-normal velocity standard deviation normalized by its maximum. 67
- 6.3 Measured temperature profiles at $Ra = 8.96 \times 10^{11}$ and $\Gamma = 1.13$ at the center line. (a) Profile of the mean temperature normalized by the temperature difference of $\vartheta_b - \vartheta_{cp}$. (b) Profile of the temperature standard deviation normalized by its maximum. Here ϑ_b and ϑ_{cp} denote the mean bulk temperature and the surface temperature of the cooling plate. 67

List of Figures

| | | |
|------|--|----|
| 6.4 | Normalized velocity and temperature cross-correlation $f_c(\tau)$ as a function of the delay time τ , at measuring positions $z = 2.4$ mm (a), $z = 6.15$ mm (b) and $z = 160$ mm (c) at the center line. τ is the time delay caused by the measurement starting time and the spatial separation between the LDA measurement volume and thermistor, which is $300 \mu\text{m}$ | 69 |
| 6.5 | Snapshots of measured time series of the wall-normal velocity (blue) and the temperature (red) fluctuations w' and T' . (a) at $z = 2.4$ mm; (b) at $z = 6.15$ mm; (c) at $z = 160$ mm all at the center line. | 71 |
| 6.6 | Profiles of diffusive heat flux \dot{q}_d (green full circles) and convective heat flux \dot{q}_c (red full circles) calculated from wall-normal velocity and temperature fluctuations at $\text{Ra} = 8.96 \times 10^{11}$ and $\Gamma = 1.13$ at the center line. | 72 |
| 6.7 | Profiles of total heat flux \dot{q} calculated from the velocity and temperature fluctuations at $\text{Ra} = 8.96 \times 10^{11}$ and $\Gamma = 1.13$ at the center line. | 72 |
| 6.8 | Measured histograms of the wall-normal convective flux fluctuation $\sigma_{(w'.T')}$, at $z = 2.4$ mm (circles), $z = 6.15$ mm (square) and $z = 160$ mm (triangle) at the center line. | 73 |
| 6.9 | Measured wall-normal velocity profiles at $\text{Ra} = 8.96 \times 10^{11}$ and $\Gamma = 1.13$ at side window 1 (open circles) and 2 (open triangles), plotted in logarithmic scale. (a) Profiles of the mean wall-normal velocity normalized by the maximum mean horizontal velocity, (b) profiles of the wall-normal standard deviation normalized by their own maximum. | 74 |
| 6.10 | Measured temperature profiles at $\text{Ra} = 8.96 \times 10^{11}$ and $\Gamma = 1.13$ at side window 1 (open circles) and 2 (open triangles). (a) Profiles of the mean temperature normalized by the temperature difference of $\vartheta_b - \vartheta_{cp}$, (b) profiles of the temperature standard deviation normalized by their own maximum. | 75 |
| 6.11 | Snapshot of measured time series of the wall-normal velocity (blue) and the temperature (red) fluctuations, w' and T' . (a) at $z = 2.4$ mm; (b) at $z = 6.59$ mm; (c) at $z = 160$ mm at side window 1. | 76 |
| 6.12 | Snapshot of measured time series of the wall-normal velocity (blue) and the temperature (red) fluctuations, w' and T' . (a) at $z = 2.4$ mm; (b) at $z = 6.59$ mm; (c) at $z = 160$ mm at side window 2. | 77 |
| 6.13 | Profiles of diffusive heat flux \dot{q}_d (green) and convective heat flux \dot{q}_c (red) calculated from wall-normal velocity and temperature fluctuations at $\text{Ra} = 8.96 \times 10^{11}$, $\Gamma = 1.13$ and at side window 1 (open circles) and 2 (open triangles). | 78 |

| | | |
|------|---|----|
| 6.14 | Profiles of total heat flux \dot{q} calculated from the velocity and temperature fluctuations at $Ra = 8.96 \times 10^{11}$ and $\Gamma = 1.13$ at side window 1 (open circles) and 2 (open triangles). | 78 |
| 7.1 | Two fundamental types of errors: (a) Random or precision errors, (b) Fixed or bias errors [93]. | 81 |
| 7.2 | Bias sources [93] | 82 |
| 7.3 | Bias error correction techniques [93] | 83 |

LIST OF TABLES

4.1 Dimensions of measurement volume with $f = 500$ mm front lens. Two probes combined a 3D LDA set-up, includes a pair of green beam (2D probe), a pair of blue beam (2D probe) and a pair of dark green beam (1D probe) 25

5.1 Set of parameters and selected results of the velocity measurements at $\Gamma = 1$, $\text{Pr} = 0.7$ and Ra between 3.44×10^9 and 9.77×10^{11} . $\langle U_{max} \rangle$ denotes the maximum of the mean horizontal velocity, Re_s denotes the shear Reynolds number, Re_g denotes the global Reynolds number, $\delta_{v,d}$ and dimensionless $\delta_{v,d}/H$ are the displacement thicknesses for the viscous BL. The first three Rayleigh numbers (with star) are from the current measurements, measured in the small convection cell with 2.5 m height and 2.5 m diameter. The others are from earlier measurements [19] in the large convection cell with 6.3 m height and 7.14 m diameter. 51

5.2 Set of parameters and selected results of the temperature measurements at $\Gamma = 1$, $\text{Pr} = 0.7$ and Ra between 3.44×10^9 and 9.78×10^{11} . Re_g is the global Reynolds number, $\delta_{\theta,d}$ and dimensionless $\delta_{\theta,d}/H$ are the displacement thicknesses for the thermal BL. The first two Ra numbers (with star) are from the current measurements, measured in the small convection cell with 2.5 m height and 2.5 m diameter. The others are from the earlier measurements [4], measured in the big convection cell with 6.3 m height and 7.14 m diameter. 52

5.3 Preview of boundary layer power law scaling results from both experiments and numerical simulations. β denotes the exponent of viscous BL (δ_v) scaling; γ denotes the exponent of thermal BL (δ_θ) scaling. 53

List of Tables

| | | |
|-----|--|----|
| 5.4 | Set of parameters and selected results of the velocity and temperature measurements at $Ra = 2.88 \times 10^{10}$ at various locations. $\langle U_{max} \rangle$ is the maximum of the velocity, δ_v and dimensionless δ_v/H are the displacement thicknesses for the viscous BL, δ_θ and dimensionless δ_θ/H are the displacement thicknesses for the thermal BL. | 56 |
| 5.5 | Set of parameters and selected results of the velocity and temperature measurements at $Ra = 1.27 \times 10^9$, $\Gamma = 2.76$ at various locations. $\langle U_{max} \rangle$ is the maximum of the velocity. δ_v and dimensionless δ_v/H are the displacement thicknesses for the viscous BL. δ_θ and dimensionless δ_θ/H are the displacement thicknesses for the thermal BL. . | 63 |